

AD-A162 330

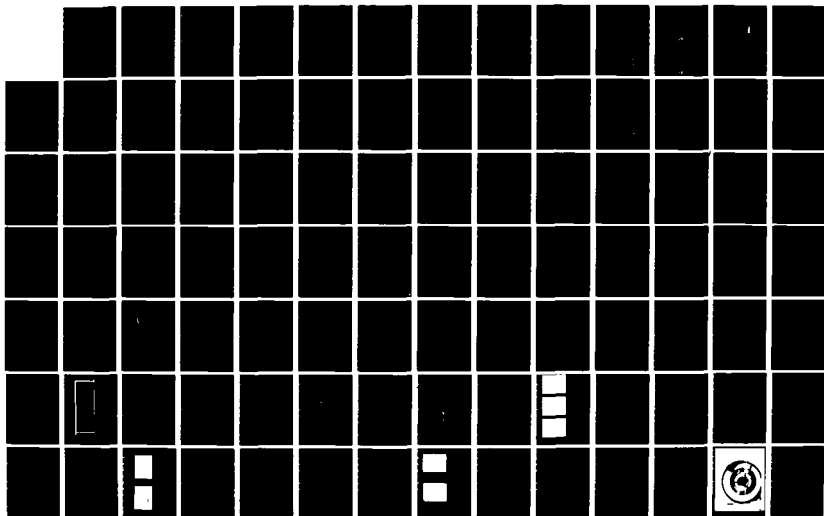
NEUTRAL BEAM INTERACTIONS WITH MATERIALS(U) MICHIGAN
UNIV ANN ARBOR DEPT OF NUCLEAR ENGINEERING
R M GILGENBACH ET AL 22 NOV 85 AFOSR-84-0130

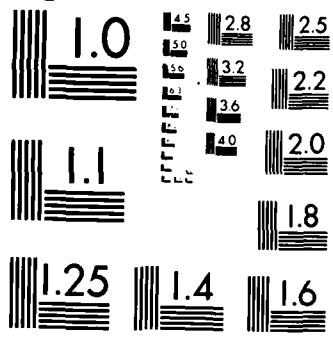
1/2

UNCLASSIFIED

F/G 28/9

NL





MICROCOPY RESOLUTION TEST CHART
NATIONAL BUREAU OF STANDARDS 1963-A

7

AD-A162 330

*Final Progress Report to:
The Air Force Office of Scientific Research
for the Project:*

Neutral Beam Interactions
with Materials
(AFOSR 84-0130)

R. M. Gilgenbach
Nuclear Engineering Department

J. J. Duderstadt
Nuclear Engineering Dept. and
Dean, College of Engineering

R. S. Ong*
Aerospace Engineering

DTIC
S DEC 13 1985
D

November 1985

Intense Energy Beam Interaction Laboratory
The University of Michigan

*deceased

THIS FILE COPY



DISTRIBUTION STATEMENT A
Approved for public release;
Distribution Unlimited

85 12 12 074

D-162 330

REPORT DOCUMENTATION PAGE

1a. REPORT SECURITY CLASSIFICATION Unclassified			1b. RESTRICTIVE MARKINGS			
2a. SECURITY CLASSIFICATION AUTHORITY			3. DISTRIBUTION/AVAILABILITY OF REPORT Unclassified, approved for public release, distribution unlimited			
2b. DECLASSIFICATION/DOWNGRADING SCHEDULE			5. MONITORING ORGANIZATION REPORT NUMBER(S)			
PERFORMING ORGANIZATION REPORT NUMBER(S) AFOSR84-0130			7a. NAME OF MONITORING ORGANIZATION Air Force Office of Scientific Research			
3a. NAME OF PERFORMING ORGANIZATION University of Michigan		3b. OFFICE SYMBOL (If applicable)	7b. ADDRESS (City, State and ZIP Code) Physical and Geophysical Sciences Bolling Air Force Base, Washington, DC			
6c. ADDRESS (City, State and ZIP Code) Nuclear Engineering Department Ann Arbor, MI 48109			9. PROCUREMENT INSTRUMENT IDENTIFICATION NUMBER AFOSR84-0130			
4a. NAME OF FUNDING/SPONSORING ORGANIZATION AFOSR		4b. OFFICE SYMBOL (If applicable)	10. SOURCE OF FUNDING NOS.			
5c. ADDRESS (City, State and ZIP Code) Physical and Geophysical Sciences Bolling AFB, Washington, DC			PROGRAM ELEMENT NO.	PROJECT NO.	TASK NO.	WORK UNIT NO.
1. TITLE (Include Security Classification) Final Report Neutral Beam Interactions with Mtrls						
12. PERSONAL AUTHOR(S) R. M. Gilgenbach and J. J. Duderstadt						
3a. TYPE OF REPORT Final		13b. TIME COVERED FROM 6/1/84 TO 10/31/85		14. DATE OF REPORT (Yr., Mo., Day) Nov. 22, 1985		15. PAGE COUNT 99
16. SUPPLEMENTARY NOTATION						
17. COSATI CODES			18. SUBJECT TERMS (Continue on reverse if necessary and identify by block number)			
FIELD	GROUP	SUB. GR.	Neutral beams, radiation signatures, beam-material interactions			
19. ABSTRACT (Continue on reverse if necessary and identify by block number)						
<u>Abstract</u>						
<p>This final report describes experimental and theoretical research which concerns the interaction of electron, neutral or ion beams with surface ablation plasmas. This problem is of interest in the case of particle penetration to outgassing or ablating objects in a high vacuum environment. Preliminary experiments have been performed during a 5 month research option concerning "Electromagnetic Radiation Emission from Electron-Beam Induced Ablation Plasmas." The Michigan Electron Long Beam Accelerator (MELBA) has been used to generate state-of-the-art electron beam parameters:</p>						
20. DISTRIBUTION/AVAILABILITY OF ABSTRACT UNCLASSIFIED/UNLIMITED <input checked="" type="checkbox"/> SAME AS RPT. <input type="checkbox"/> DTIC USERS <input type="checkbox"/>				21. ABSTRACT SECURITY CLASSIFICATION Unclassified		
22a. NAME OF RESPONSIBLE INDIVIDUAL Dr. P. ce Smith			22b. TELEPHONE NUMBER (Include Area Code) (202) 767-4908		22c. OFFICE SYMBOL	

Voltage = -0.7 to -1MV

Current = 1 to 30kA

Pulselength from 0.1 to 4 microseconds

Diode impedance data and temporally resolved spectroscopic measurements both indicate that anode plasma effects play an important role in these experiments.

We have constructed a neutral beam-ablation plasma experiment which employs a Q-switched ruby laser to independently generate a dense ablation plasma. The neutral beam is generated by a (5-20 keV) duopigatron ion source with charge exchange neutralization cell. Experimental results of beam attenuation show excellent agreement with predictions based on available cross-section data. In studying the attenuation of the neutral beams we have considered primarily charge exchange processes although we are estimating the relative contributions of momentum scattering and impact ionization. Line density values from a self-similar expansion model show good agreement with attenuation data. Spectroscopic measurements of the ablation plasma yield singly and doubly ionized lines.

We have developed a one-dimensional computational physics code which simulates the ablation of a carbon target by a proton beam. This is accomplished by coupling a sophisticated collisional-radiative equilibrium (CRE) ionization dynamics model, a one-dimensional, single temperature and fluid hydrodynamics model, and an energy deposition model. The total package is then applied to simulating the beam-target interaction under a variety of beam conditions. Other applications considered include heating due to inner-shell photon absorption and calculation of the amount of K radiation emitted by the direct interaction of a beam proton with a target atom.

The basic approach involves coupling a one-dimensional hydrodynamic code to an ionization dynamics and an energy deposition model. Because the radiation emitted by the plasma is an important diagnostic tool, we have tried to model the ionization dynamics very carefully. This is accomplished by developing an ionization dynamics model which considers a large number of excited states and atomic processes.

The atomic processes which are considered in our model are:

- 1) collisional ionization
- 2) three body recombination
- 3) collisional excitation
- 4) collisional de-excitation
- 5) spontaneous emission
- 6) radiative recombination
- 7) dielectric recombination

A model to calculate the stopping power for energetic, "structured" (those carrying electrons into the target) low Z ions has been developed. Low Z ions are both energetic and structured at typical specific energies of a few hundred keV/amu (e.g. 1 MeV helium). The atomic structure is taken into account by describing the electron cloud of the projectile with elastic form factors in the first Born approximation. However, at these energies the first Born approximation begins to break down. Hence, two corrections are included: (i) the Bloch correction to account for the scattering of wave packets (instead of plane waves) for close collisions, and (ii) the Barkas effect which corrects for deviations from pure Rutherford scattering due to the displacement of an oscillating electron. Structure is introduced more approximately in these two terms. An attempt has been made to allow sufficient generality to describe ionized targets as well as neutral solids.

Final Progress Report to:
The Air Force Office of Scientific Research
for the Project:
"Neutral Beam Interactions with Materials"
AFOSR84-0130

R. M. Gilgenbach, J. J. Duderstadt, R. S. Ong*
Nuclear Engineering Department
The University of Michigan
Ann Arbor, Michigan 48109

November 1985

*Deceased

CONTENTS

Introduction	p. 1
R.O.I. Research Option: Electromagnetic Radiation Emission from Electron Beam Induced Ablation Plasmas	p. 2
I. Theoretical Progress	p. 37
a) Stopping Power of Low-Z "Structured" Projectile Ions	p. 37
b) Computer Simulation of Ion Beam Target Dynamics and Radiation Emission	p. 48
II. Experimental Progress	p. 59
a) Neutral/Ion Interactions with a Laser Ablation Plasma	p. 59
b) Duopigatron Based Experiments Concerning Neutral/Ion Beam Interactions with Laser Ablation Plasmas	p. 61
1) Beamline and Vacuum Systems	p. 64
2) Ruby Laser System	p. 68
3) Beam Diagnostics	p. 70
4) Ion and Neutral Beam Probe Measurements	p. 70
5) Ablation Plasma Production and Diagnostics	p. 79
6) Beam-Plasma Interaction Experiments	p. 81
c) Fabrication of an Applied-B Ion Diode for Febetron	p. 87
III. Graduate Students Supported Under this Contract	p. 99
IV. Publications and Doctoral Dissertations	p. 99
V. Honors and Awards	p. 99

Accession For	
NTIS CRA&I	<input checked="" type="checkbox"/>
DTIC TAB	<input type="checkbox"/>
Unannounced	<input type="checkbox"/>
Justification	
By	
Distribution/	
Availability Codes	
Dist	Avail and/or Special
A-1	



Introduction

This final report is divided into several sections. The first section covers the (5 month) Research Option: "Electromagnetic Radiation Emission from Electron Beam Induced Ablation Plasmas." The remainder of the report covers the progress made during a 12 month period in research concerning the interaction of neutral and ion beams with solids and laser induced ablation plasmas. Both theoretical and experimental results are presented.

R.O.-I Research Option: Electromagnetic Radiation Emission from
Electron Beam Induced Ablation Plasmas

During the past year the UM Intense Energy Beam Interaction Laboratory has developed a state-of-the-art accelerator for the generation of intense microsecond pulselength electron beams. This generator, the Michigan Electron Long Beam Accelerator (MELBA), operates within the following range of parameters:

Pulselength = 0.1 to 4.0 μs , with fully adjustable pulselength over the
first 1.0 μs ,

Voltage = -1MV maximum, flat to within $\pm 10\%$ over the first 1.0 μs ,

Current = 10 kA or greater,

Total delivered energy for a 2.0 μs pulse > 10 kJ.

In order to perform studies of electron beam pumped optical emission, we have performed extensive research into the problems of field-emission cathode designs for μs electron beams [1]. The goal of this study was the generation of uniform, reproduceable electron beams for long pulse lengths without diode shorting from cathode plasma closure. The most important issue was the gap plasma closure velocity which determined the maximum attainable pulselengths. In the course of our investigation we have discovered that anode plasmas can also have a significant effect on diode performance. The following discussion is arranged in a loose chronological order.

Investigation of Anode Plasma Effects in Diode Behavior

Much of the diode data was obtained prior to our spectroscopic investigations and therefore represented a starting point for this work. The basic configuration for the initial diode experiments is depicted in Figure 1. Both carbon fiber and velvet cathodes were studied at gap spacings of 6, 8, 10 cm. Typical experimental data for two shots, M486 and M491, with an AK gap spacing $d_{AK} = 10$ cm, and a carbon fiber brush cathode of radius $r_c = 7$ cm is presented in Figure 2. The data has been divided up into two categories; type B, characterized by very fast rates of impedance collapse and current increase, and type A with slowly varying character. One of the important conclusions of this initial research was that a large area carbon brush cathode allowed significantly longer pulselengths than the velvet cathodes because of lower cathode plasma expansion velocities. Velvet cathodes always gave type B behavior. Brush cathodes gave type A shots (M486) and shots with both type A and type B character (M491) referred to as type B.

The anode design also underwent a series of modifications. These are depicted in Figure 3. Configuration 1 was a large carbon cylinder with a 9 cm radius. The outer aluminum surface was coated with Aerodag (carbon spray) to reduce potential sputtering or else left clean. Pressure jumps after the shot and large currents indicated that the carbon spray formed ions in the gap which enhanced the electron current. The appearance of arc damage on the aluminum on the sharp edge around the carbon led us to a redesign of the carbon block anode as we suspected that outgassing as well as field enhancement under the influence of the intense electron flux

EXPERIMENTAL CONFIGURATION FOR DIODE STUDIES

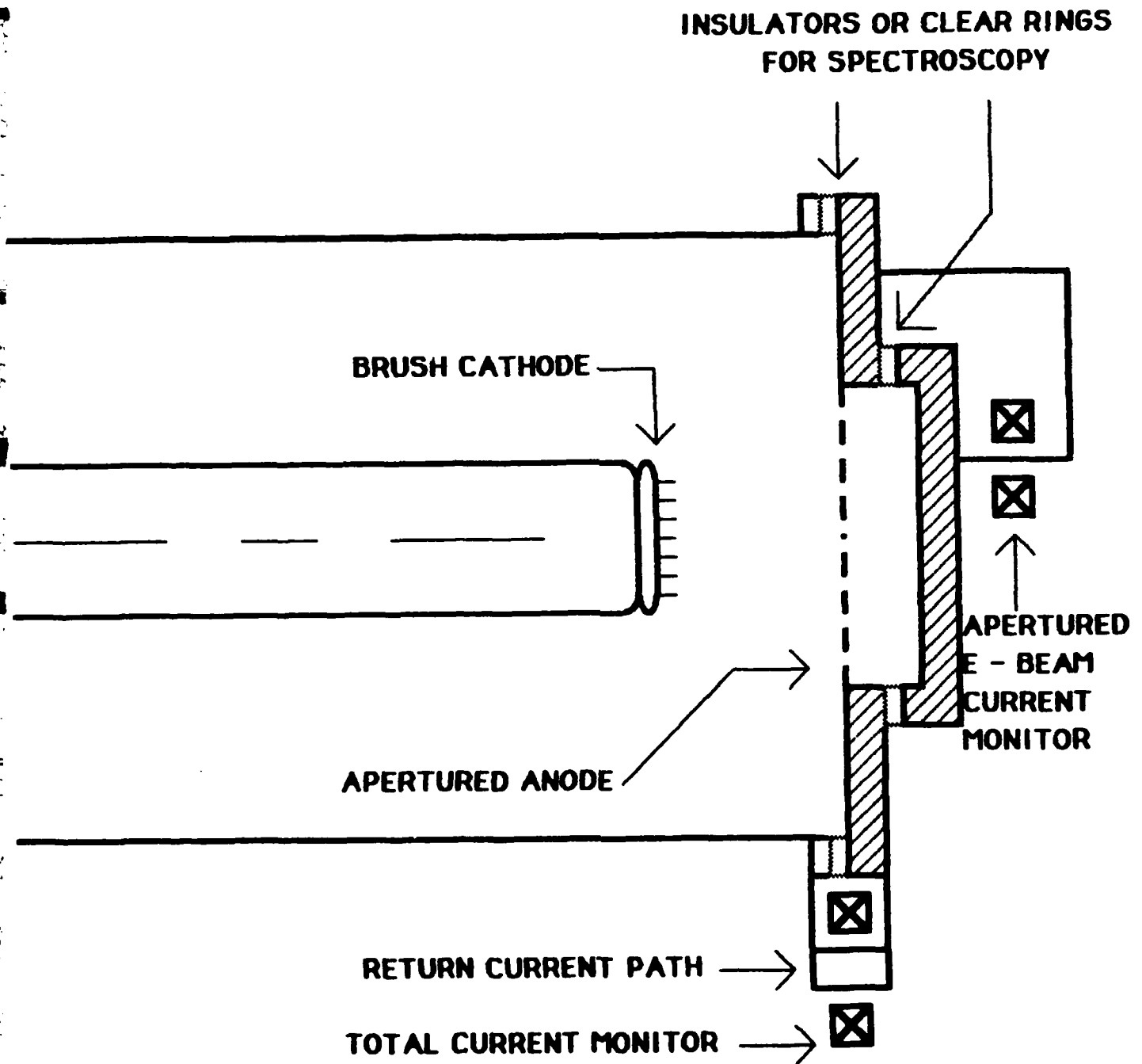


Figure 1

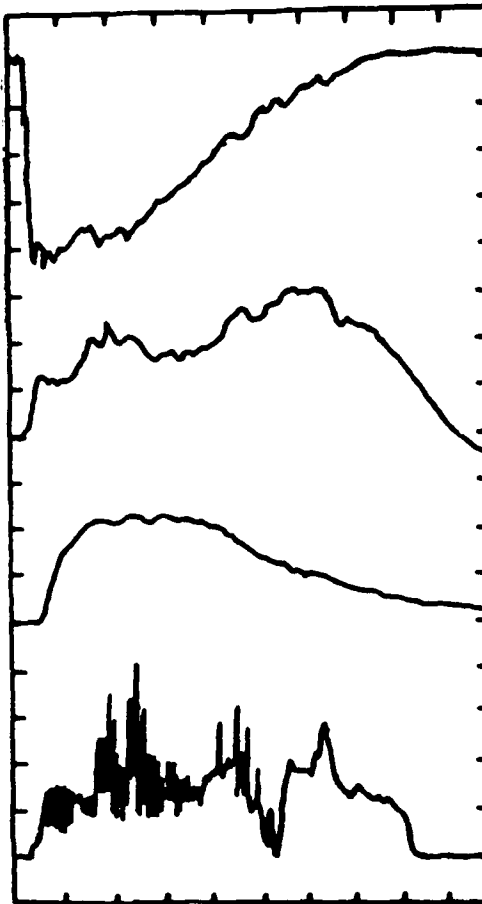
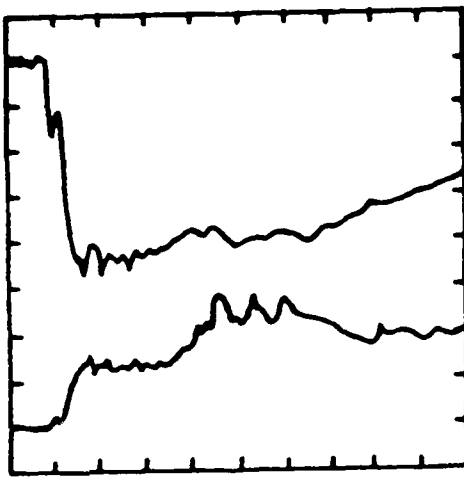
EXPERIMENTAL DATA

BRUSH CATHODE: RADIUS = 7 cm , AK GAP = 10 cm

200 ns/div

500 ns/div

M486



VOLTAGE
(160 kV/div)

CURRENT
(5.3 kA/div)

HARD X-RAYS

APERTURED
E-BEAM CURRENT

M491

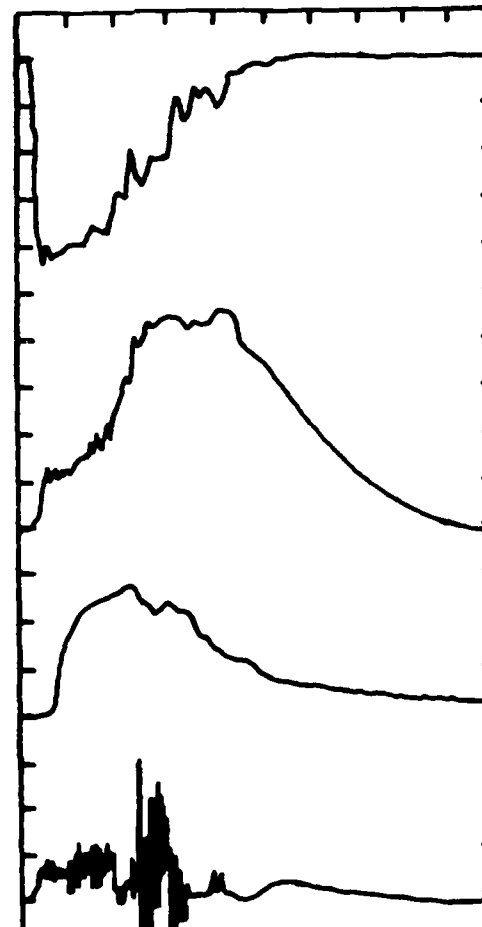
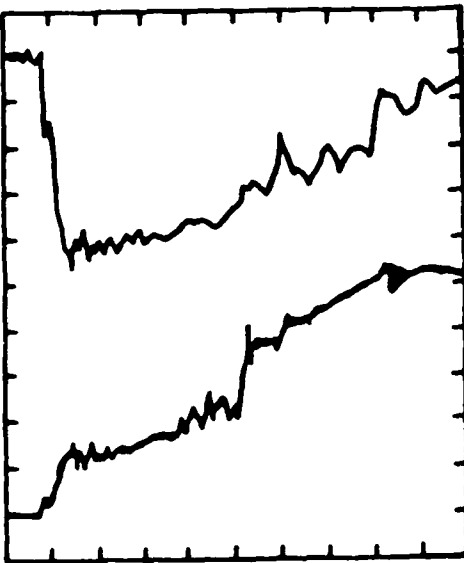


Figure 2

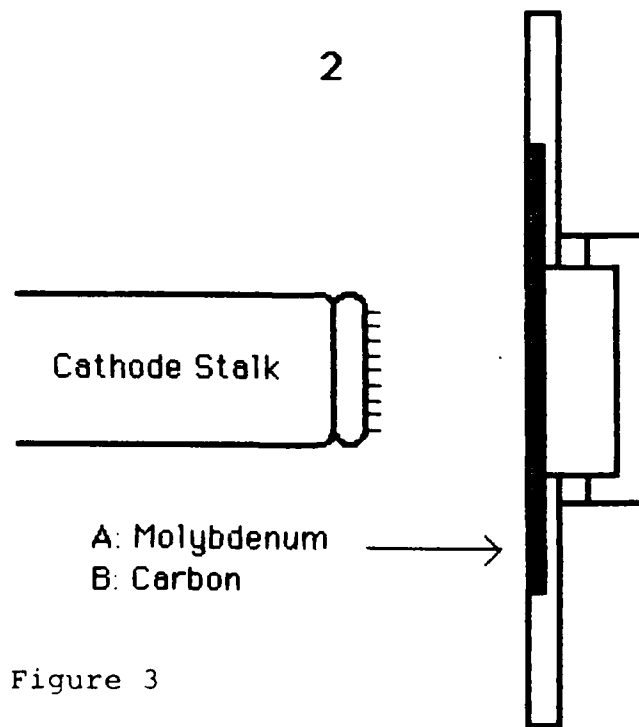
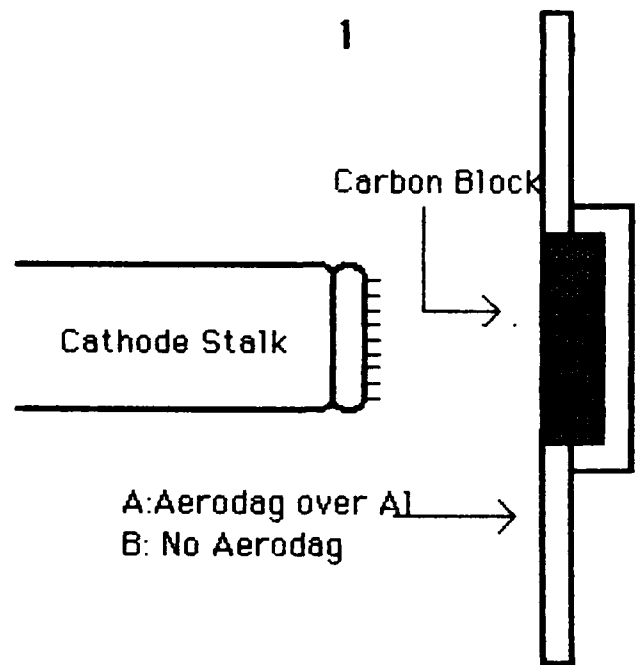


Figure 3

was occurring. In configuration 2 the anodes were 0.3 cm thick and 15 cm in radius, well removed from impinging electron flux. We tried molybdenum and carbon anodes in this configuration. In order to withstand the multi-kilojoule electron beam pulses, reduce the X-ray flux, and to reduce the potential damage to the insulators and cathode in the non-crowbarred mode where arcing and subsequent anode melting and sputtering may occur, a solid poco-graphite anode was employed. It is interesting to note that the diode current at 500 ns with the molybdenum anode was 6.7 ± 0.3 kA compared to the case for the same size carbon anode at 8.8 ± 0.6 kA. From some of the current modeling and energy deposition calculations following, it is apparent that this can be attributed to carbon's greater porosity and ability to absorb gases and impurities readily. Ions, which come from plasma formed at the anode contribute to space charge neutralization at the cathode, allowing greater electron currents. The operating experience with each anode design is summarized in Table 1.

Some observations on the experimental data in Figure 2 can be made. The rapid oscillations in both the apertured electron beam diagnostic and voltage during the time of rapid current increase and voltage droop suggest some of instability with counter-streaming electrons and ions in the diode [2]. An effective gap closure velocity can be defined by the total time there is a signal on the apertured beam diagnostic (for a noncrowbarred pulse). In this case $U_{\text{eff}} = d_{\text{AK}}/t_{\text{short}}$. U_{eff} is proportional to the rate of impedance collapse and is always greater for a type B shot. U_{eff} measures only the contribution to gap closure from the cathode plasma. Table 2 summarizes the closure velocity information by type of shot for each cathode and gap spacing. The apparent closure velocity U_{app} is

<u>shots</u>	<u>gap(cm)</u>	<u>anode</u>	<u>I at 0.5 μs(kA)</u>
384-396	10	1A	10.6 \pm 0.6
397-402	10	1B	9.1 \pm 0.5
403-406	8	1B	14.1 \pm 2.1
407-411	6	1B	17.5 \pm 0.8
412-417	10	2A	6.7 \pm 0.3
418-438	10	2B	8.8 \pm 0.6
439-446	8	2B	12.1 \pm 1.2
447-452	10	2B	7.4 \pm 0.9
453-458	8	2B	10.9 \pm 0.6
459-466	10	2B	11.4 \pm 3.9
		(velvet cathode)	
467-481	8	2B	11.2 \pm 2.2
		(velvet cathode)	

Table 1

summary of diode closure velocities(cm/ μ s)

	<u>brush</u>		<u>velvet</u>	
<u>A-K gap(cm)</u>	<u>10</u>	<u>8</u>	<u>10</u>	<u>8</u>
Apparent				
Type A	3.3 \pm .4	3.3	none	
	(3)	(1)		
Type B	5.3 \pm .42	6.0	6.1	6.2
	(2)	(1)	(1)	(1)
Effective				
Type A	3 \pm .7	2.1 \pm .3	none	
	(3)	(7)		
Type B	3.5 \pm .6	2.6	3 \pm .6	4.1 \pm .3
	(4)	(1)	(4)	(5)

Table 2

discussed below in the section on current modeling. Note that U_{app} measures the total contribution to gap closure from both the cathode and anode plasmas (if any). The increased closure velocity for type B shots seems to indicate that closure of anode plasmas across the AK gap may also be contributing to the impedance collapse, although increases in current due to other mechanisms would also be perceived as an increase in U_{app} . Our further investigations of the diode physics concerned the issues of current modeling, beam dynamics, and the central issue of ion production mechanisms and absorbed dose at the anode.

Current Modeling Including Anode Plasma Ions

The physics of the flow of charged particles in these high voltage diodes is well developed. For the current densities in our diode the Child-Langmuir model is appropriate. However, this model is 1-dimensional in nature and is only strictly applicable to diodes with infinite (large) aspect ratios (r_c/d_{AK}). For real diodes, particularly for those in our study ($r_c/d_{AK} \approx 1$), 2-d effects are important and the amount of current from the diode edges must be ascertained. The current model used was a combination of the edge emission model of Parker et. al. [3] and the technique of Poukey [4] for inclusion of ion flows and relativistic corrections.

The total current is given by the sum of a planar contribution and an edge one:

$$I_{total} = A_{planar}(j_{ep1} + j_{ip1}) + A_{edge}(j_{eed} + j_{ied}) \quad (1)$$

where $A_{planar} = \pi r_c^2$, $j_{ep1} = h^2 j_{c1}$ (2)

$$j_{c1} = \frac{2.334 \times 10^{-6} V^{3/2}}{(d_o - u(t - t_o))^2} \quad (3)$$

Here j_{c1} is the Child-Langmuir expression [5] for current density modified

for gap closure. In that expression j is in amps/cm² for V in volts, d_0 in cm. t_0 is the diode opening time, d_0 is the initial AK gap spacing and U is an empirically determined closure velocity. As discussed above U_{eff} is appropriate, and in practice it is also possible to vary U until a best fit to the data is obtained. We refer to this velocity as the apparent closure velocity U_{app} . These two are not in general equal, although when they are we can have greater confidence in space charge models for the flow. h^2 is the correction factor due to Poukey that modifies j_{c1} for the presence of ions (leading to enhanced electron current density) and relativistic effects (leading to reductions in electron current density $\approx 10\%$ for 700 kV). h is given by

$$h = \frac{3}{4} \int_0^{\pi/2} \frac{\sin 2\theta \, d\theta}{[\sin \theta (1 + \beta \sin^2 \theta)^{1/2} + \alpha(1 + \beta)^{1/2} (\cos \theta - 1)]^{1/2}} \quad (4)$$

In this expression β is a dimensionless electron energy, and α is a model parameter varied to include ion flows of variable magnitude

$$j_{ip} = \alpha j_{ep1} [(Zm_e/m_i)(1 + \beta)]^{1/2}, \quad \beta = eV/2m_e c^2 \quad (5)$$

In general the integral for h must be solved numerically. In the case where

$\beta=0$ (nonrelativistic) and $\alpha=0$ (no ions), we may integrate analytically to find $h=1$ and we recover the original results of Child and Langmuir.

Langmuir [6] treated the nonrelativistic case with $\alpha=1$ numerically, a case he called bipolar flow. Jory and Trivelpiece [7] solved the relativistic case without ions exactly using a series solution. Each of these limits are contained in expression 4 and have been reproduced in testing of the model.

The edge current is modeled as an angular portion of the flow between two concentric torri, with the cathode edge as the portion of the inner torus and the anode and diode chamber as the outer torus. In the limit of large cathode radius compared to edge radius the flow between concentric torri is approximately the same as the flow between infinite concentric cylinders, a case where analytical series solutions have been found by Langmuir and Blodgett [8]. We recover the results of Parker for edge emission

$$A_{\text{edge}} = (\theta/2\pi)4\pi^2 r_c (d_o + r_{e0}), \quad j_{\text{eed}} = h^2 j_{\text{lb}} \quad (6)$$

$$j_{\text{lb}} = \frac{2.334 \times 10^{-6} \gamma^{3/2}}{(d_o + r_{e0})^2 \Delta^2} \quad (7)$$

Where j_{lb} is the Langmuir-Blodgett result for current density for infinite concentric cylinders. In this expression Δ is given by

$$\Delta = \gamma - (2/5)\gamma^2 + (11/120)\gamma^3 - (47/3300)\gamma^4 + 0.00168\gamma^5 \quad (8)$$

where $\mathcal{G} = \ln[(d_0 + r_{e0})/r_e]$, $r_e = r_{e0} + u(t - t_0)$ (9)

In expression 9 note that the model also takes into account radial expansion of the plasma. This must be modified for example in modeling of diodes in a strong external magnetic field. The correction of the edge results for relativistic and ion effects by multiplication of j_{1b} by h^2 in equation 6 is only approximate here, whereas in equation 2 it was exact. We suspect that the corrections should be on the same order as for the planar case, and errors induced by not accounting for ions and relativistic corrections are probably larger than those introduced by this ad-hoc correction. Equation 5 but with j_{eed} and j_{led} complete the description for edge emission.

The importance of edge emission can be seen by comparing this modeled edge current with that from the planar portion to obtain a scaling argument

$$\begin{aligned} I_{\text{planar}}/I_{\text{edge}} &= A_{\text{planar}}j_{ep1}/A_{\text{edge}}j_{eed} \\ &= 2\theta [(d_0 + r_{e0})r_c \Delta^2/d_0^2] \\ &\approx r_c/d_0 \quad \text{for } r_{e0} \ll d_0 \end{aligned}$$

In the limit of large aspect ratio the contribution of edge emission becomes negligible, as we expect. For the Melba diodes $r_c/d_0 \approx 1$ so edge emission and planar emission contribute equally.

A space charge model can be used to define the apparent closure velocity. In principle one could imagine that rather than use the experimentally measured voltage and closure velocity to determine the modeled current, it may be possible, given the experimental voltage and current, to solve for U. This procedure is not possible given the full model above, thus an abbreviated model for the diode current was developed which takes edge emission into account by defining an effective planar diode emitting area. The diode current is given by

$$I = \frac{\pi(Kr_c)^2 h^2 2.334 \times 10^{-6} V^{3/2}}{(d_0 - U_{app}(t - t_0))^2} \quad (10)$$

Here Kr_c is the 'effective radius'. K is a correction factor to take into account non-ideal space charge behavior. $K = 1$ for an infinite planar diode. Solving for $d(t) = d_0 - U_{app}(t - t_0)$

$$d_0 - U_{app}(t - t_0) = 2.708 \times 10^{-3} Kr_c h [V^{3/2}/I]^{1/2} \quad (11)$$

Thus if the diode can be modeled by space charge flow, a best fit of $h[V^{3/2}/I]^{1/2}$ should be a linearly decreasing function of time whose slope yields U_{app} , the apparent closure velocity. At t_0 the following must also be satisfied in order that the theory be consistent

$$d_0 = 2.708 \times 10^{-3} K r_c \{h(V(t_0), \alpha) [V(t_0)^{3/2} / I(t_0)]^{1/2}\}_{fit} \quad (12)$$

which determines K . $K \approx 1.4 - 1.9$ for the 10 cm gap, 7cm radius brush cathode shots considered above. In order to implement this model, t_0 , the diode opening time must be specified. This can take on many values depending on what definition of opening time you subscribe to. A sensitivity analysis shows that t_0 can vary by over 0.2 μs and U changes by at most 10%.

The results of applying the model to shots M486 and M491 is shown in Figures 4 and 5. $U_{eff} = 2.6 \text{ cm}/\mu\text{s}$ for M486 (type A). With this value of U and the experimental voltage, both Child-Langmuir models (solid line) match the experimental current points quite well at both early and late times. Incidentally, $U_{app} = 2.7 \text{ cm}/\mu\text{s}$ for this shot, signifying that we might expect good agreement. The larger currents observed between 0.45 μs and 1.2 μs suggested the presence of ions leading to bipolar current flows and enhancements of electron current. The bipolar current model is also shown and has ions "turned on" (α nonzero) at 0.45 μs and linearly increasing until full bipolar flow ($\alpha = 1$) is reached at 0.70 μs . In fact current increases above Child-Langmuir were noted between 0.4 and 0.6 μs on almost every shot taken. We felt this was caused by exceeding some sort of critical anode dose for plasma formation. Since our operating conditions were often very close, even for different gap spacings, this behavior might be expected. The important and unknown issue was the beam dynamics which would determine the beam current density at the

M486

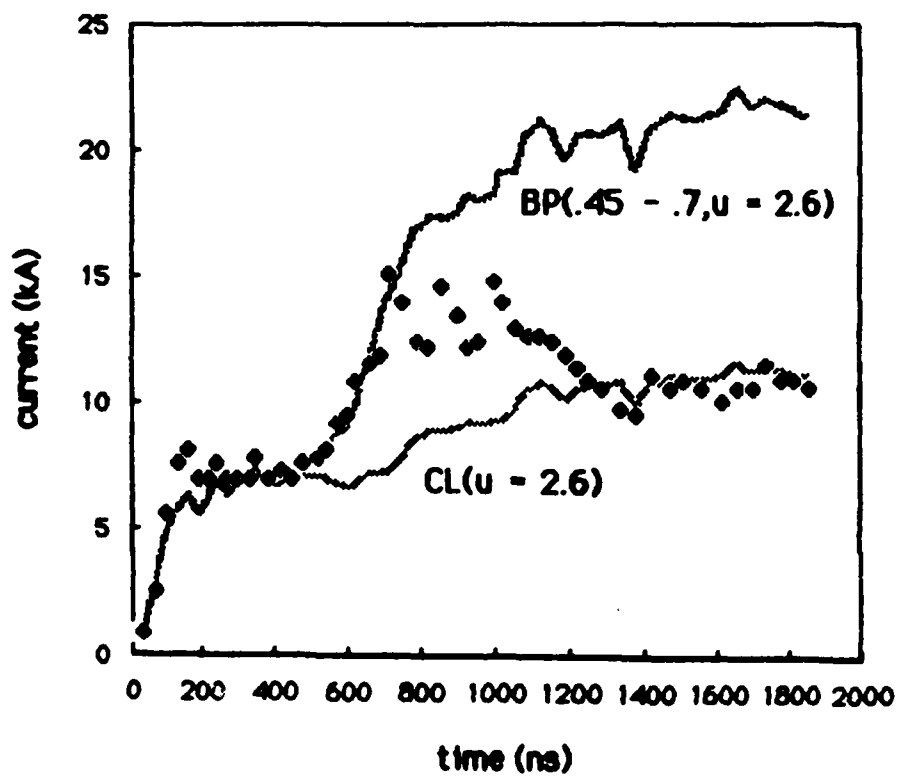


Figure 4

M491

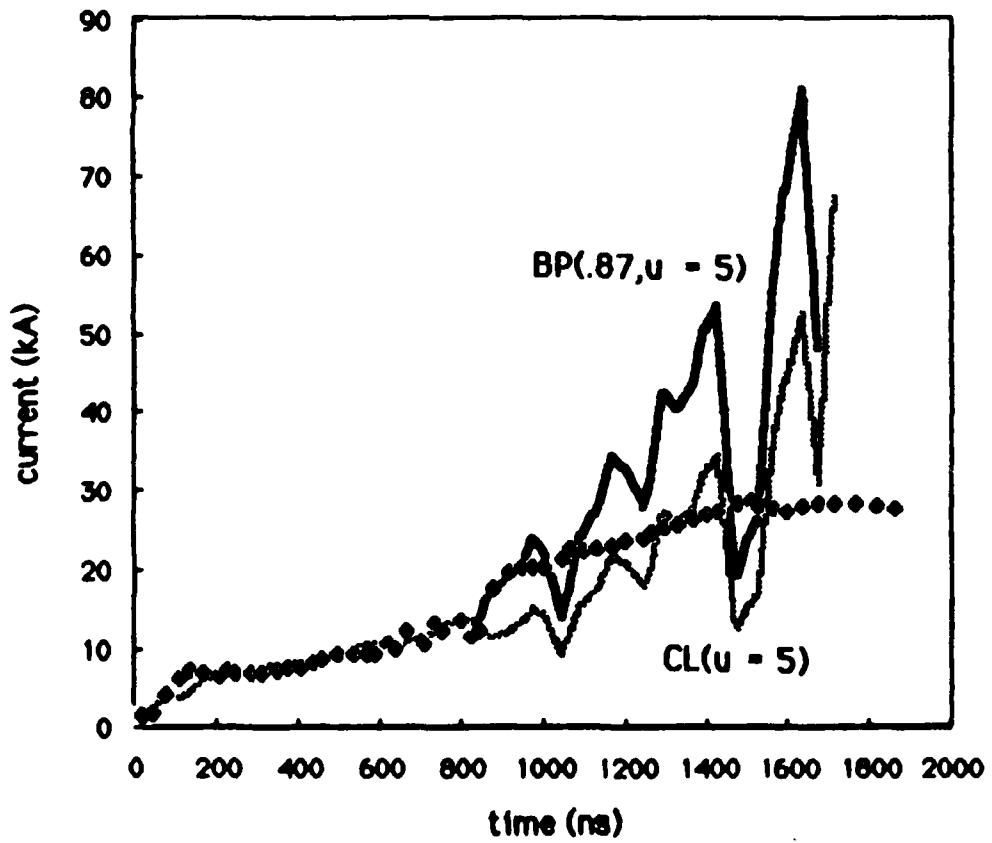
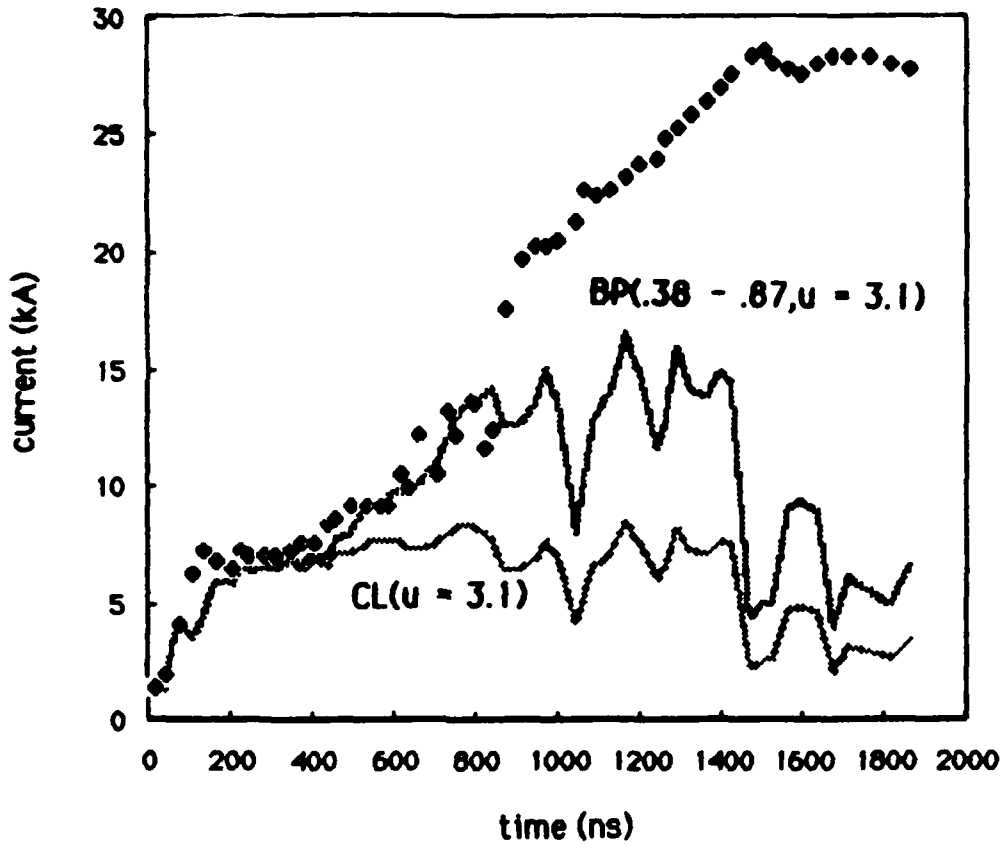


Figure 5

anode. If the beam was pinching, high absorbed doses could be reached and anode plasmas created easily giving significant plasma optical emission. In addition the contribution of the impact ionization of the background must be evaluated. This effect can be significant for long pulselength machines [9].

The same modeling approach is followed for M491 (type B) but failed to produce agreement at late times. Note that the fluctuating behavior of the current model is due to its strong dependence on the voltage which is drooping and very spikey. At early times, using the effective closure velocity $U_{\text{eff}} = 3.1 \text{ cm}/\mu\text{s}$, there is both a Child-Langmuir plateau and increasing currents consistent with the bipolar model between 0.38 and 0.87 μs . The qualitative agreement at late times with the apparent closure velocities $U_{\text{app}} = 5 \text{ cm}/\mu\text{s}$ may suggest the influence of anode plasma closure. However the lack of complete agreement suggests that other phenomena need to be considered. Vacuum arc behavior is ruled out on the basis of the constant impedance behavior expected of arcs. The currents are also not consistent with other models for high current pinching diodes [10]. It is evident from observing the same type of current behavior for molybdenum anodes, that the cathode plasma also plays a role in the formation of these very large currents. There are extensive references in the Russian literature [11,12] to cathode plasma instabilities in long pulse beams leading to enhancements over Child-Langmuir current densities.

The mechanism for these instabilities is the depletion of the cathode plasma by drawing electrons off faster than they are being resupplied by plasma formation. This is critical for long pulselengths where the plasma may not be continually regenerated when the electric field and electric

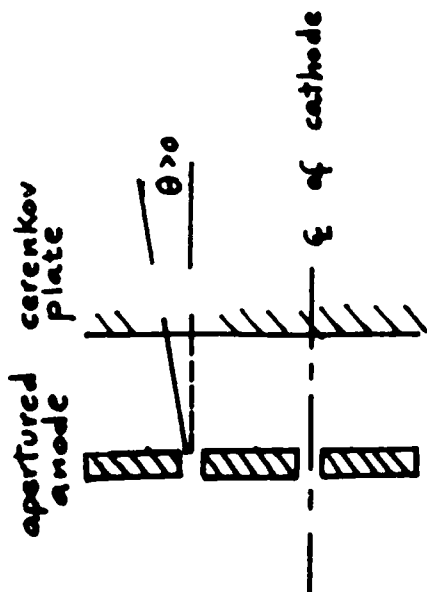
field rates are reduced after the fast initial rise. This occurs when the gap impedance has dropped below some critical value, depending of course on the cathode plasma properties. Dropping impedance can occur, of course, because of gap closure, but also in this case after ions form and enter the gap. The electrons are drawn off at the rate determined by the diode impedance, however, and since the plasma is not being resupplied, it is possible that gap closure may be checked or slowed. A charge imbalance builds up in the plasma and a positive ion sheath forms at the cathode surface to compensate, leading to large electric fields. The electrons are now accelerated and reach the cathode plasma emission surface with a finite velocity. The configuration is now similar to a triode with the cathode flare acting in the role of the grid in a triode. The large electric fields created at the cathode by the ion sheath results in a resupply of material to the bulk of the cathode plasma. The net charge imbalance disappears and the diode returns to its normal operating characteristics. This instability may cycle once or more. These large enhancements over even bipolar currents are interesting. With such rapidly falling voltages and increasing currents, the anode surface dosage increases substantially. Further investigation is necessary.

Beam Dynamics for Anode Plasma Studies

Computer simulations and modeling of the beam dynamics were completed using the Stanford Electron Optics Code (SEOC). From experimental measurements of the anode current density distribution during the first 0.5 μ s we had reason to suspect that the center of the beam was pinching slightly while the outer portions were diverging (see

Figure 6). The code simulations agree with this result. In order to model measured currents during the first 0.5 μ s (before the suspected presence of ions) it was necessary to account for edge emission, just as in the analytical model. In this case planar emission contributed more than edge emission while for the analytical model edge emission was slightly greater than planar emission. The most important information obtained from the simulation was the current density of the beam on the anode, which would allow us to calculate the absorbed dose and to address the mechanism for anode plasma formation. For the 10 cm gap, 7 cm radius cathode shown in Figures 7 and 8 this is 20 A/cm². The simulations with SEOC converge with a great deal of effort and are at their limit of usefulness. The code was not designed for intense electron beams with large self magnetic fields. As we will progress to significantly higher current densities, it is clear that another simulation code will be necessary. We have obtained TIGER, a Monte Carlo energy deposition code. This code coupled with an adequate beam dynamics code will allow us to calculate absorbed doses in solids, gases, and plasmas in many different experimental situations.

Calculations of spatially and time varying absorbed energy dose using the model of Spencer [13] failed to produce the doses required for plasma formation. Many authors have reached the conclusion that 200 - 700 J/gr on carbon or aluminum will cause the release of desorbed gases [3,14,15]. These gases are subsequently impact ionized or avalanche ionized at higher surface densities. These studies were all done for short (\approx 100 ns) high current density (\approx 1 kA/cm²) pulses. The absorbed doses for vaporization of carbon to form neutrals or ions is even higher (50 - 180 kJ/gr) [16-17].



θ - beamlet divergence

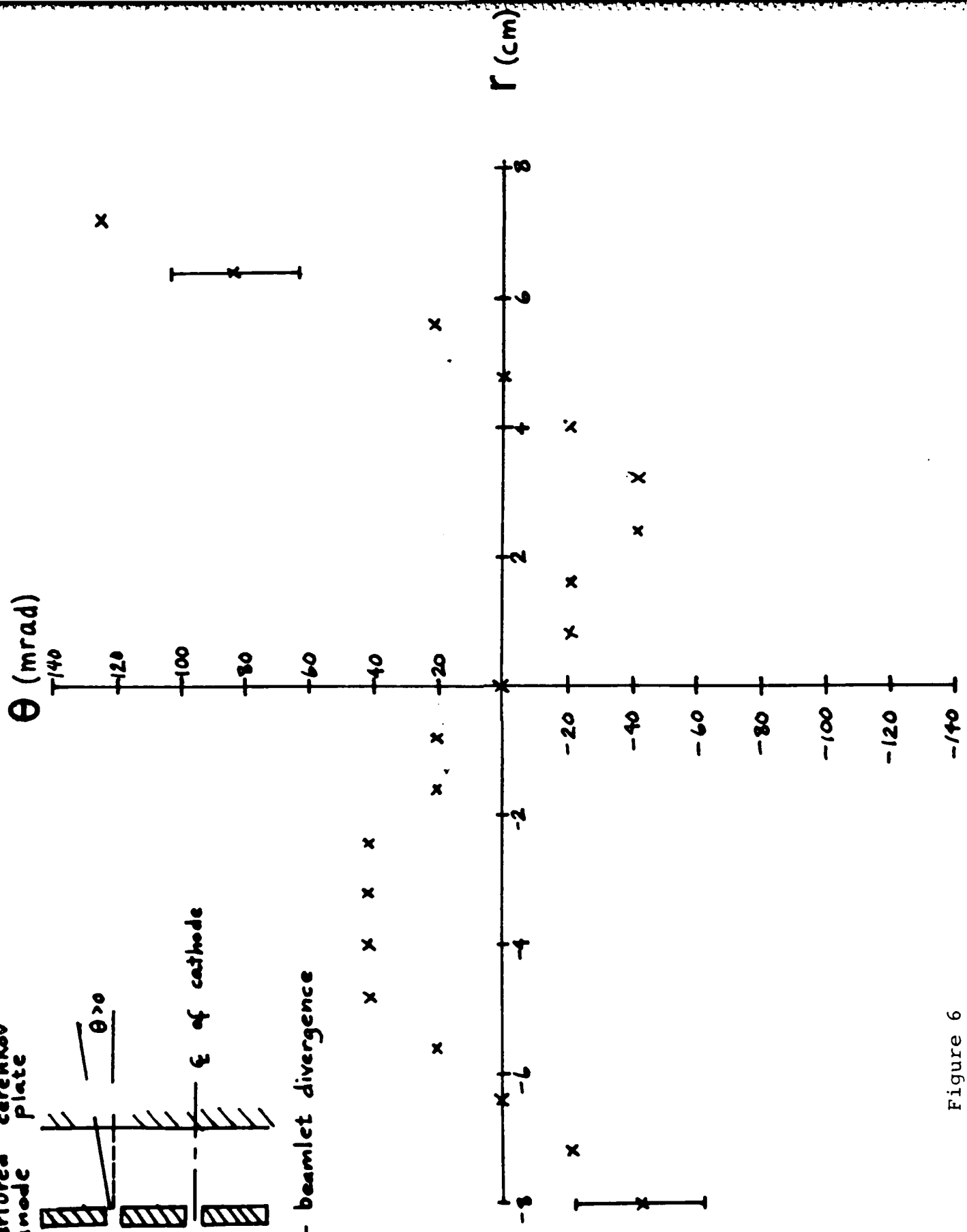


Figure 6

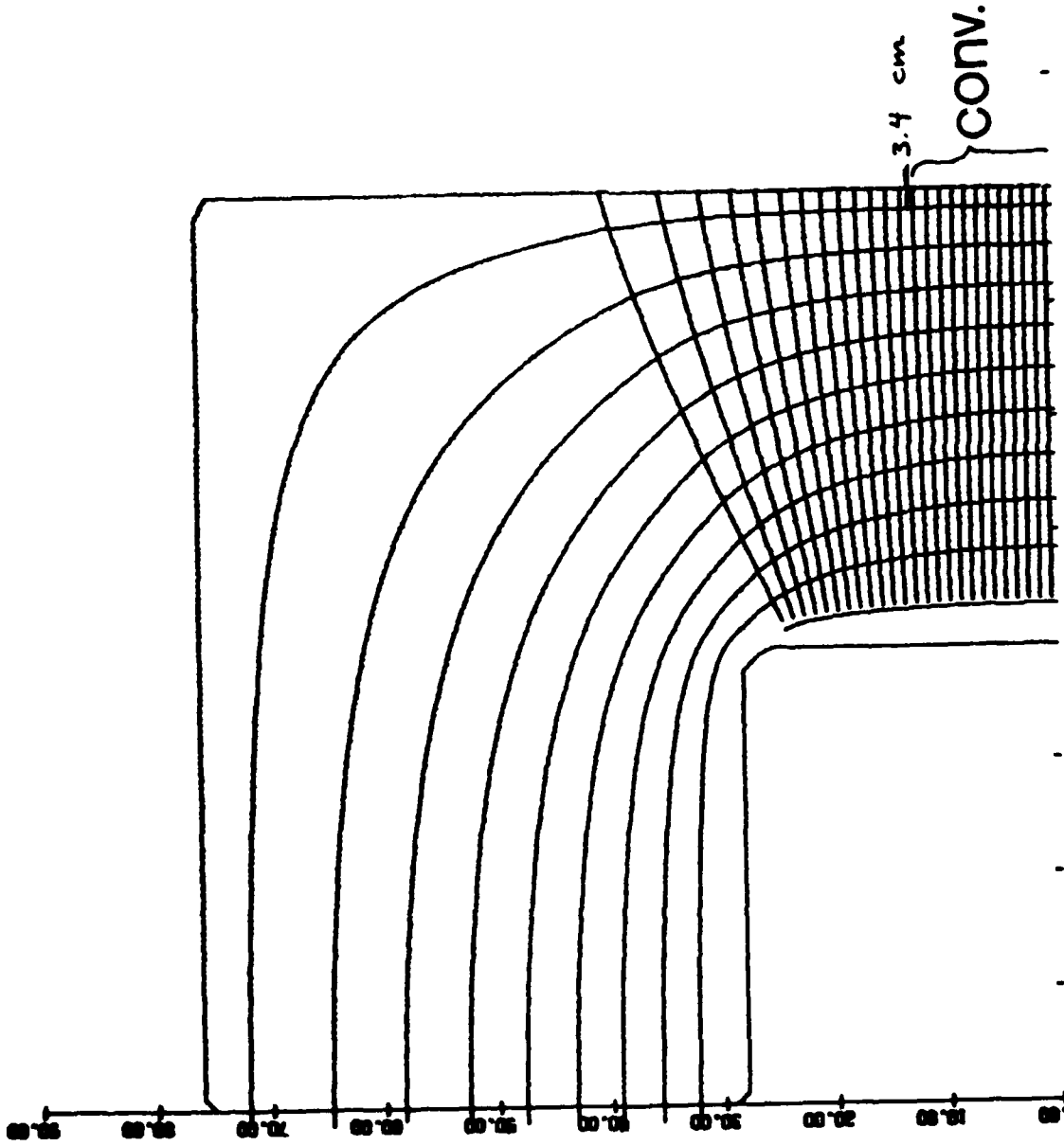
V 720 kV

I = 4.5 kA

P = 7.4 μ P

$P_{CI} = 2.6 \mu$ P

$J_{anode} \approx 20 \frac{A}{cm^2}$

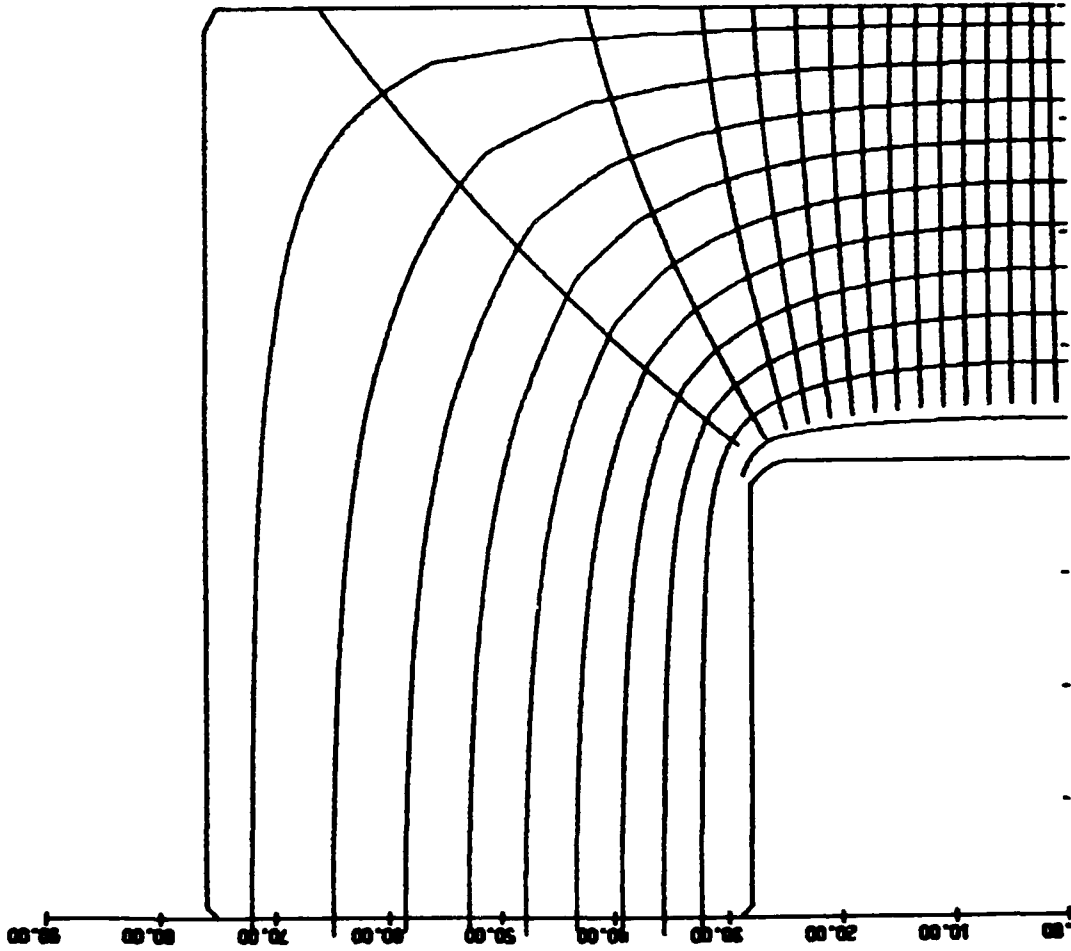


6 cm emission surface
Figure 7

$V = 720 \text{ kV}$

$I = 7.7 \text{ kA}$

$P = 12.6 \text{ } \mu\text{p}$



edge emission

Figure 8

Using the current density incident on the anode given by SEOC, the average energy during the first $0.5 \mu\text{s}$ (700 kV), and $0.311 \text{ gr}/\text{cm}^2$, the electron range for that energy, the approximate anode dose is $45\tau(\mu\text{s}) \text{ J}/\text{gr}$. At $\tau=0.45 \mu\text{s}$ the dose is $20 \text{ J}/\text{gr}$ which is an order of magnitude below the minimum required dose. A simple calculation shows that impact ionization cannot contribute sufficient numbers of ions to allow bipolar flow at the diode pressures we operate at. It thus seems that the presence of ions is not admitted.

The experiments of Swain et. al. [14] were done with in-situ cleaning of aluminum anodes. They note that the doses for anode plasma formation for anodes contaminated by pump oil or vacuum grease are reduced by a factor of 10 or more. Poco-graphite has about a 20% porosity and we suspect that it is even easier to bring gases or impurities out. We suspect that pump oil and water vapor are the largest contributors to the impurities in our system. The presence of pump oil in our system is consistent with our experimental procedure of roughing on the chamber as continuously as possible. In a turbo pumped system, back diffusion of oil from the roughing pumps will occur if the blades are not spinning while in a diffusion pumped system the diffusion oil also contributes. One final point is that the critical doses necessary may be reduced for longer pulselengths.

Optical Spectra from Electron Beam Pumped Ablation Plasmas

The preliminary experimental configuration for measuring spectra is shown in Figure 1. We used polished lucite rings, as shown, which allowed light to pass through the optics and back to the screen room to be focused on the OMA slit (Optical Multichannel Analyzer). This was a configuration which would allow us to take spectra with as little delay and change to the experimental configuration as possible. There were several drawbacks to these rings, however, the first being that the curved surface of the lucite acted like a dispersing lens and the thickness as an attenuator. Secondly there is a cutoff of blue light at about 380 nm below which nothing is transmitted. Arcing to the lucite occurred during a few shots and dendrites under the surface, discovered by inspection afterwards often left one with an unavoidably ambiguous interpretation of the spectra obtained. In addition, the copious edge emission led to a large electron flux near the lucite, although no surface roughness was created. In addition to discoloration of the lucite and possible formation of a lucite surface plasma (although in fact no oxygen lines were observed), this may have led to an intense continuum-like emission or Cerenkov radiation when the OMA was gated during the pulse. It may in fact be continuum emission or possibly bremsstrahlung. This feature did not occur all the time and we were able to obtain some spectra during the pulse. Even under these restrictive conditions it was possible to obtain information which gave a better understanding of the processes that were occurring. The spectra obtained required careful interpretation.

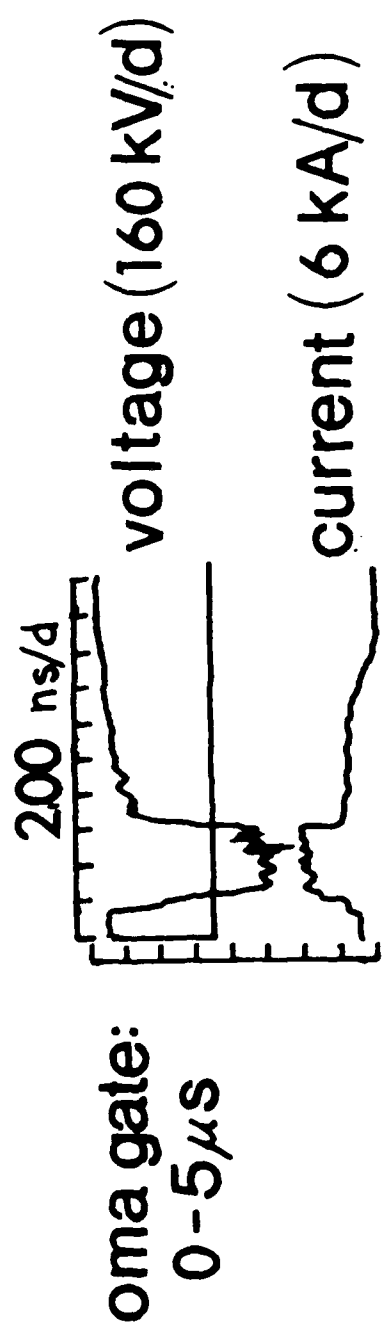
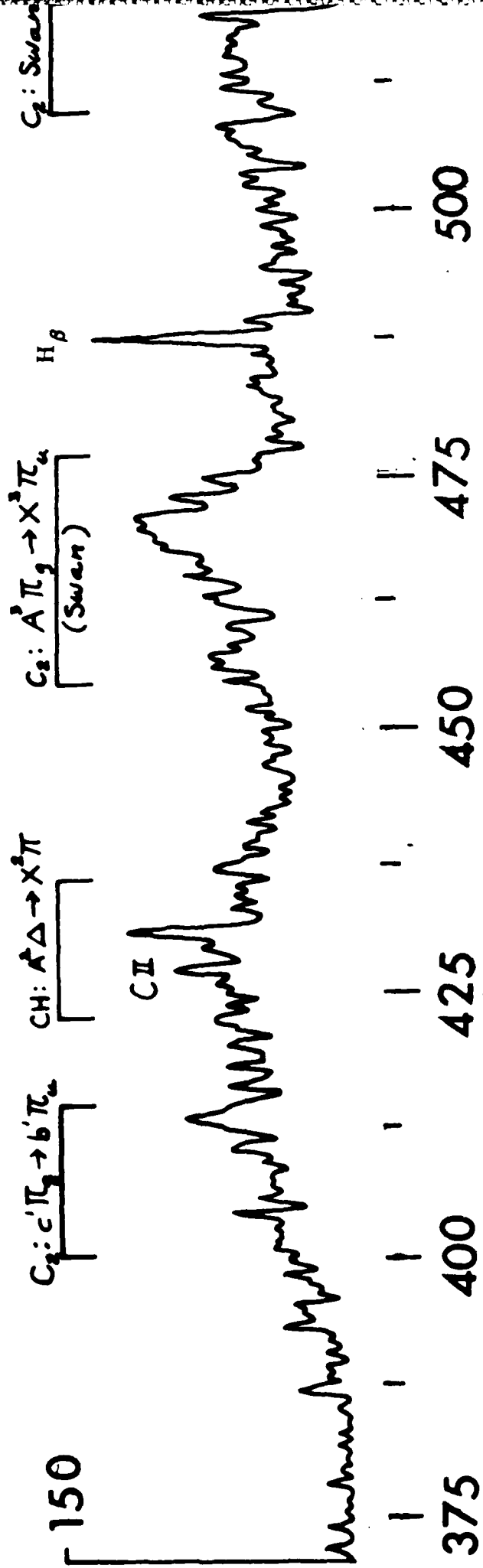
Spectroscopy on the diode chamber was made possible with highly

polished, large diameter lucite rings. Although one set of lucite rings with flat transmitting surfaces was used, the spectra using curved surfaces were not significantly different. Due to the dangers of misinterpretation of spectra in the analysis, we weighted the results, favoring spectra obtained early in the run before significant lucite damage could have occurred.

The first spectra were obtained using OMA gates the full width of noncrowbarred pulses. With these gates, light from a whole range of plasma producing events in the diode would have been observed including cathode and anode plasma light, plasma formed by the late time pulses due to the ringing stage [1] or the plasma formed from any late time arcs which may have occurred. Initially these spectra were hard to interpret and no lines were readily identifiable. This was due to the large Stark shifts caused by the diode electric fields. In fact the shift in the H_{β} line in Figure 9 and 10 is about 17 \AA , which corresponds to a diode electric field of 75 kV/cm. This is in good agreement with the theoretically obtained electric fields of 100 kV/cm required to see this shift. Shifts were also observed in the C_2 spectrum and in the very intense $C^+ - 4265 \text{ \AA}$ line. No neutral carbon lines were observed, apparently because of their lower intensities and since important lines may have been hidden by the intense C_2 structures. Since the spectra are shifted, they must have been obtained during the applied field i.e. during the electron beam pulse.

For the pulses in Figures 9 and 10, the time of the applied field is shorter than is needed for the cathode plasma to cross the gap, thus we are observing anode plasma components. There are some other interesting

M551



oma gate:
0-5 μs

Figure 9

M552

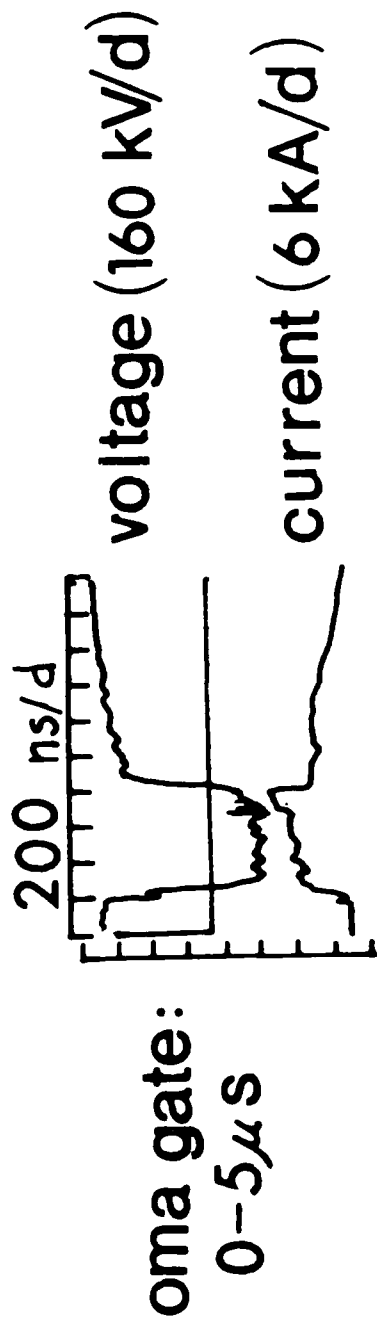
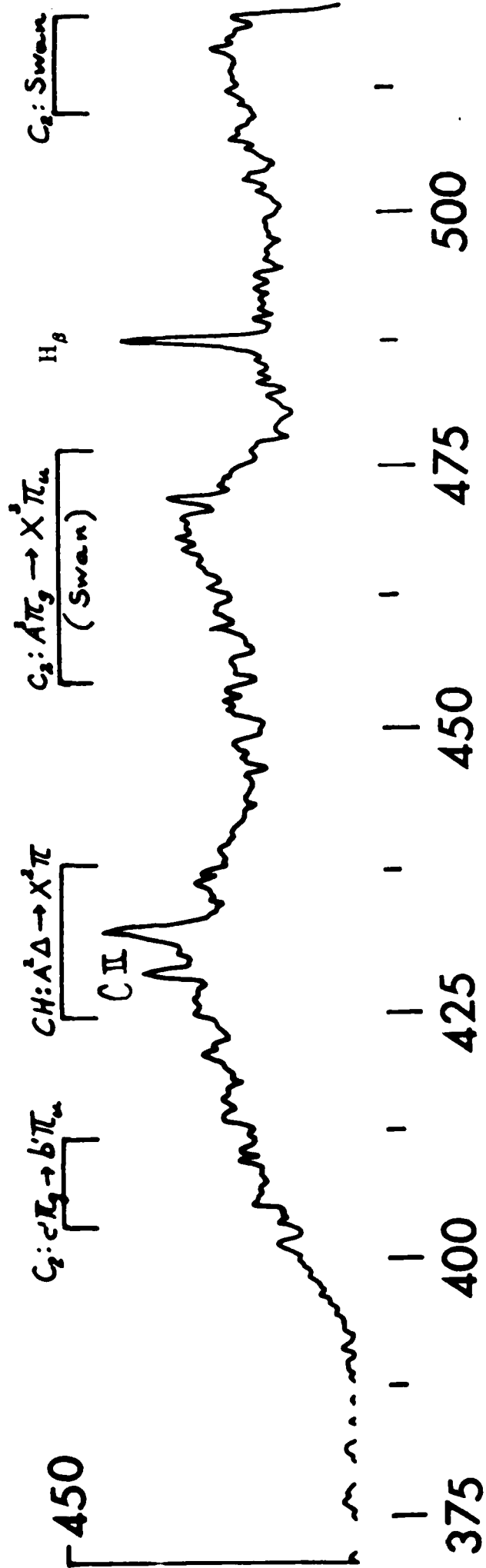


Figure 10

features of those two spectra. First, the cutoff in transmission below about 380 nm is identified. A broad spectrum white light source was used to verify this cutoff. Next note the increase in continuum-like structure from the first (M551) to the second (M552) as it obscures details and hinders resolution. By the sixth shot of that day line emission was completely obscured. Finally, comparing the two spectra reveals that the slightly longer pulse length (M552), extending just into the region of current ramp-up resulted in 3x more emission giving us evidence for the evolution of desorbed gases from the anode at $\tau = 0.5 - 0.6 \mu\text{s}$. This was also confirmed on a different day using short OMA gates immediately following short crowbarred pulses. Shorter gates can be used to exclude all light except that produced by the anode ablation plasma. No line spectra were obtained for pulses $\leq 0.4 \mu\text{s}$. The spectra obtained for pulses = 0.45 - 0.7 μs were completely similar to the structure in the presented spectra but at relative amplitudes ≤ 100 . One spectra was obtained when the OMA gate bracketed the late time, low energy, high current pulse due to the LRC ringing of the reverse charged stage. Again the same structure was observed, indicating the anode as source, but at a relative amplitude of ≥ 500 , indicating that the low energy optimizes the front surface dose by minimizing the electron range.

The spectra obtained from a noncrowbarred pulse is given in Figure 11. The gate was moved forward to about 0.8 μs to avoid the continuum-like structure that would obscure the lines, and indeed note that the background is flat. The CH peak is absent, the C^+ peak is more clearly visible, and the H_β peak is reduced in amplitude. In fact on consecutive shots that day the hydrogen peak was constantly reduced in amplitude. The

M618

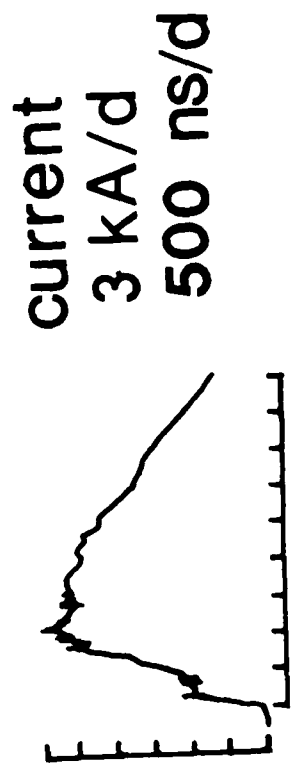
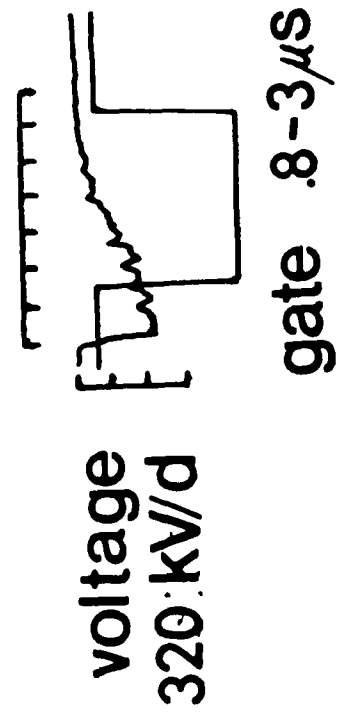
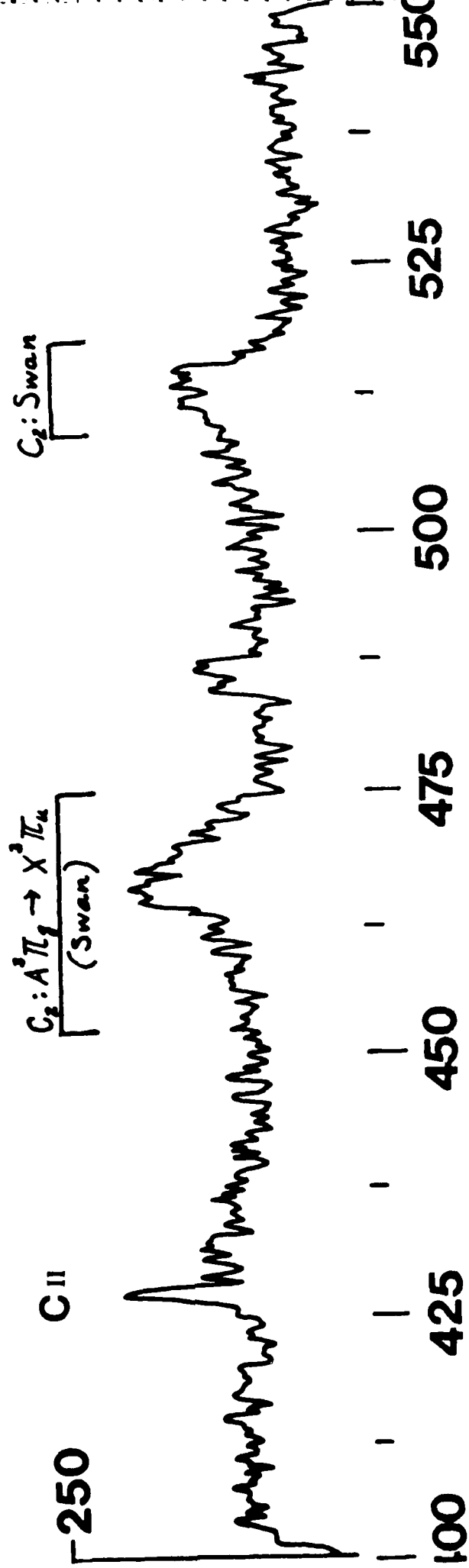


Figure 11

Stark shifts obtained here are smaller, implying smaller average fields.

A large portion of the spectra in all three cases remains unidentified due to the difficulty when Stark shifts are present but also due to the resolution limits of the instrument. Theoretically densities can be estimated from broadening and temperatures from line ratios. These possibilities will be investigated for this plasma but resolution limits again make the task difficult. Continued investigations on the plasmas formed in the diode will be made using a new aluminum ring with a shielded observation port. This new structure will eliminate the ambiguity of the previous scheme and allow us to optimize the light output by using thin quartz windows. If Cerenkov or continuum-like emission is still a problem, a smaller area cathode can be used to minimize the edge emission. In addition we will be able to look right on the surface of a carbon target. Other experimental results at this lab stress the importance of looking right along the surface at the most dense part of the ablation plasma.

Conclusions on Preliminary Results During Research Option

We understand the diode physics fairly well and further investigation and optimization of plasma production within the diode may help fill the remaining gaps. We have formulated a tentative hypothesis about the plasma formation process which will require some further testing

- 1) Contaminated anode surfaces contribute to the space charge neutralization of the beam on timescales $\approx 0.5 \mu\text{s}$.

2) Space charge neutralization leads to pinching to a much greater degree than in the simulations, increasing the local current density at the anode. This may also lead to cathode plasma instabilities and enhancements over even bipolar currents.

3) More plasma is formed from the usual anode desorption mechanisms at longer times $\approx 1 - 2 \mu\text{s}$. For noncrowbarred pulses the energy deposition approaches 15 kJ, front surface doses are maximized and production of carbon by vaporization mechanisms may come into play.

Definite conclusions about the density and temperature of these plasmas are not possible from these preliminary *experimental results*. The measurements were all taken at the maximum OMA gain because of the small intensities detected. This was due for the most part due to the diffusing and attenuating nature of the lucite ring. A preliminary estimate of the lower bound on plasma density from space charge neutralization considerations of the electron beam is $3 \times 10^9 \text{ cm}^{-3}$. These important questions will be answered with the greatly improved viewing method we are pursuing.

The most important conclusion we have reached is that methods for increasing the beam current density at the anode or carbon target must certainly be investigated. This is required both to form the plasma and to put it in a highly ionized nonequilibrium state. In order to maximize the current density one or more of the following steps can be taken.

1) We are in the process of acquiring external field coils for magnetic compression as well as for extracting rotating beams which have increased deposition due to their shorter penetration depths.

2) From the Child-Langmuir scaling it is evident that decreasing the gap spacing is also an alternative. If it is decreased sufficiently it may be possible to create a self pinched electron diode, early in the pulse. Pinching increases the current density from local area decrease but also from shorter penetration depths due to nonperpendicular incident angles. We must assess whether this drives the generator harder than it was designed for. At present we can probably reduce the gap by a factor of 2, increasing the current density by a factor of 4.

References

1. "Microsecond Electron Beam Diode Closure Experiments," Invited Paper R. Gilgenbach et. al., Fifth IEEE Pulsed Power Conference, June 10-12, 1985, Washington D.C.
2. "Electron Stream Interactions with Plasmas," R.J. Briggs, Research Monograph No. 29, MIT Press, Cambridge, MA., 1964.
3. "Plasma induced field emission and the characteristics of high current electron flow," R.K. Parker, R.E. Anderson, and C.V. Duncan, J. Appl. Phys., 45, 2463(1973).
4. "Ion effects in relativistic diodes," J.W. Poukey, Appl. Phys. Lett., 26, 145 (1975).
5. "Electrical Discharges in Gases," I. Langmuir, and K.T. Compton, Rev. Mod. Phys., 3, 191(1931).
6. "The Interaction of Electron and Positive Ion Space Charges in Cathode Sheaths," I. Langmuir, Phys. Rev., 33, 954(1929).
7. "Exact Relativistic Solution for the One-Dimensional Diode," H.R. Jory, and A.W. Trivelpiece, J. Appl. Phys., 40, 3924, (1969).
8. "Currents Limited by Space Charge Between Coaxial Cylinders," I. Langmuir, and K.B. Blodgett, Phys. Rev., 22, 347(1923).
9. "Microsecond Intensive E-Beams," E.A. Abramyan, B.A. Altercoop, and G.D. Kuleshov, in Proceedings of the 2nd International Topical Conference on High Power Electron and Ion Beam Research and Technology, Vol. 2, Oct. 3-5, 1977, pp.743-753.
10. "Relativistic Brillouin flow in the high v/c diode," J.M. Creedon, J. Appl. Phys., 46, 2946(1975).
11. "Intense monoenergetic microsecond electron beam with stabilized current," S.V. Lebedev, V.V. Chikunov, and M.A. Shcheglov, Sov. Tech. Phys. Lett., 7, 523(1981).

12. "Explosive emission of electrons," S.P. Bugaev, E.A. Litvinov, G.A. Mesyats, and D.I. Proskurovskii, *Sov. Phys.-Usp.*, 18, 51(1975).
13. "Energy Dissipation by Fast Electrons," L.V. Spencer, NBS Monograph No. 1, National Bureau of Standards, Washington D.C., 1959.
14. "The characteristics of a medium current relativistic electron-beam diode," D.W. Swain, S.A. Goldstein, L.P. Mix, J.G. Kelley, and G.R. Hadley, *J. Appl. Phys.*, 48, 1085(1977). "Observations of anode ions associated with pinching in a relativistic electron-beam diode," D.W. Swain, S.A. Goldstein, J.G. Kelley, and G.R. Hadley, *J. Appl. Phys.*, 46, 4604(1975).
15. D. Dakin, and J. Benford, PI Internal Memo, Oct. 1976.
16. "High-Power electron beam deposition studies on aluminum and graphite," M. Farber, J. E. Robin, and R. D. Srivastava, *J. Appl. Phys.*, 43, 3313(1972).
17. "The Vapor Pressure and Heat of Sublimation of Graphite," L. Brewer, P.W. Gilles, F.A. Jenkins, *J. Chem. Phys.*, 16, 797(1948).

I. Theoretical Progress

Ia. Stopping Power of Low-Z "Structured" Projectile Ions

A model to calculate the stopping power for energetic, "structured" (those carrying electrons into the target) low Z ions has been developed. Low Z ions are both energetic and structured at typical specific energies of a few hundred keV/amu (e.g. 1 MeV helium). The atomic structure is taken into account by describing the electron cloud of the projectile with elastic form factors in the first Born approximation. However, at these energies the first Born approximation begins to break down. Hence, two corrections are included: (i) the Bloch correction to account for the scattering of wave packets (instead of plane waves) for close collisions, and (ii) the Barkas effect which corrects for deviations from pure Rutherford scattering due to the displacement of an oscillating electron. Structure is introduced more approximately in these two terms. An attempt has been made to allow sufficient generality to describe ionized targets as well as neutral solids.

The first Born calculation must account for "shell corrections" at these energies. Shell corrections are energy dependent alterations to the stopping power due to the less effective contributions of the inner shell target electrons as the projectile slows down. To obtain realistic values of shell corrections, we follow Bonderup's¹ version of the local plasma approximation (LPA). The LPA is an average of the stopping power of a uniform density plasma

over the target electron cloud distribution.

Bonderup's treatment of the LPA utilizes large and small velocity expansions (projectile velocity relative to characteristic target electron speeds). The dominant contribution from the large velocity expansion is then compared to a detailed atomic calculation to introduce corrections to the LPA for not describing the binding of the target electrons. For point particles (i.e. no structure), the atomic calculation was the Bethe formula² with shell corrections calculated by Fano and Turner.³

The stopping power calculation for structured projectiles of a uniform density plasma was indicated by Ferrell and Ritchie.⁴ Their results are used for the slow velocity term. We performed the high velocity expansion using Lindhard's dielectric function.⁵ The first few terms (without shell corrections) of the atomic calculation for structured particles were obtained by Kim and Cheng.⁶ We extended the work of Fano and Turner to include the shell corrections. Since we are generally interested in only a few bound projectile electrons, we shall ignore projectile excitation.

Comparing the two high velocity expressions, we recognize the need to introduce the Lindhard-Scharff binding parameter (LSBP)⁷ in the LPA definition of the Bethe mean excitation energy. This arises from Lindhard's argument of replacing the plasma frequency with an effective frequency given by the LSBP times the plasma frequency. Based on a Thomas-Fermi-like model of the target atom, Lindhard

determined that the LSBP was a constant of order 2.

However, recent investigations of ionized targets by J. Peek⁸ have indicated that the LSBP must be dependent on the degree of target ionization such that

$$\text{LSBN}(N_t = 1) = \text{LSBP}(N_t = Z_t) \sqrt{Z_t}$$

where N_t and Z_t are the number of target electrons and protons, respectively. This has raised questions about using the LPA for ionized targets.

However, it is not surprising that Lindhard's arguments fail for one-electron target ions since it is based on a Thomas-Fermi-like (many-electron) model. Hence, we repeated his arguments with a one-electron model of the atom. For large Z_t we obtain

$$\text{LSBN}(N_t = 1) \approx 1.36 \sqrt{Z_t}$$

which essentially agrees with Lindhard's neutral LSBP value and Peek's scaling. For low Z_t we should not use Lindhard's many-electron value. However, we may use Peek's scaling to predict neutral values. These are plotted in Figure 1.

The long dashed curve is Lindhard's $\sqrt{2}$ value; the solid curve is our calculation. The short dashes with asterisks are average values based on experimental data taken from Ziegler.⁹ Our curve reflects the proper general trend with the target atomic number. This gives us confidence in our values for $\text{LSBP}(N_t = 1)$ and helps put the LPA for ionized targets on more firm ground. Data for gases are shown since the calculations are based on an isolated-atom picture of the target (appropriate for gases or highly

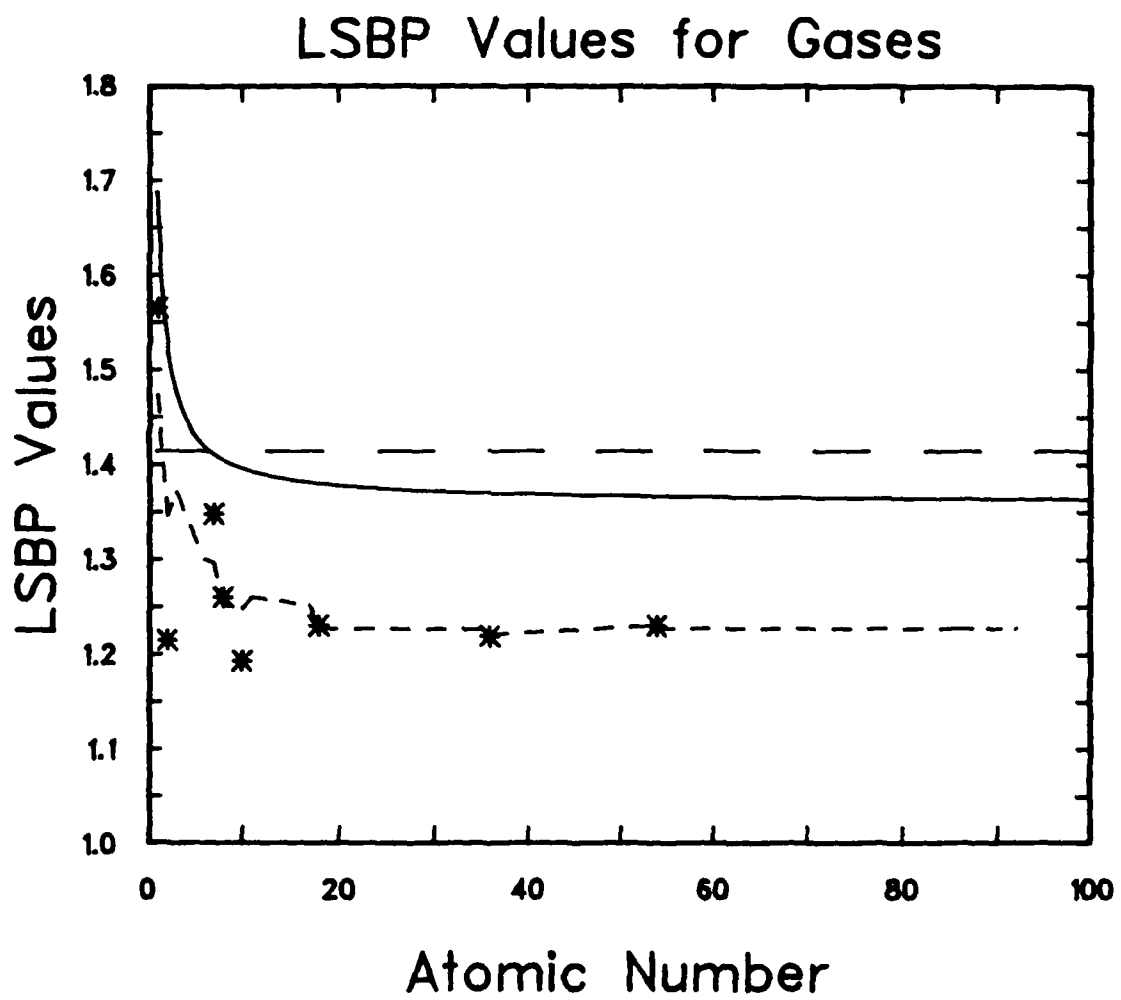


Figure 1

ionized solids). The differences in magnitudes are not important since the LSBP for neutral targets is determined to give the accepted value of the Bethe mean excitation parameter.

For partially ionized targets, we repeat a qualitative scaling argument of Lindhard's⁷ for a target with N_t electrons. This suggests the scaling

$$\text{LSBP}(N_t) = \text{LSBP}(N_t = Z_t) \sqrt{Z_t/N_t}$$

The results for $Z_t = 13$ and 81 are shown in Figure 2 along with detailed atomic calculations of J. Peek¹⁰ (boxes and asterisks). Curves 1 and 2 are based on an empirical fit to $Z_t = 13$ calculation.⁸ Curves 3 and 4 are our calculations based on theory. Lack of agreement is not surprising given the crude arguments used to obtain our scaling. It seems that our values should be modified (increased) to obtain more realistic values.

Term by term, the high velocity LPA expression is compared to the corresponding atomic calculation. In each case, replacing the plasma frequency with the LSBP times the plasma frequency is sufficient to give the proper scaling with target ionization. The actual numerical magnitude may have to be adjusted in each case to correct for deficiencies in the LPA (only one term in the shell correction had to be significantly altered). The close comparison with the detailed atomic case gives us confidence in our use of the LPA.

Structure of the projectile is introduced in the Bloch correction using the derivation attributed to Lindhard¹¹

LSBP Values for Ionized Targets

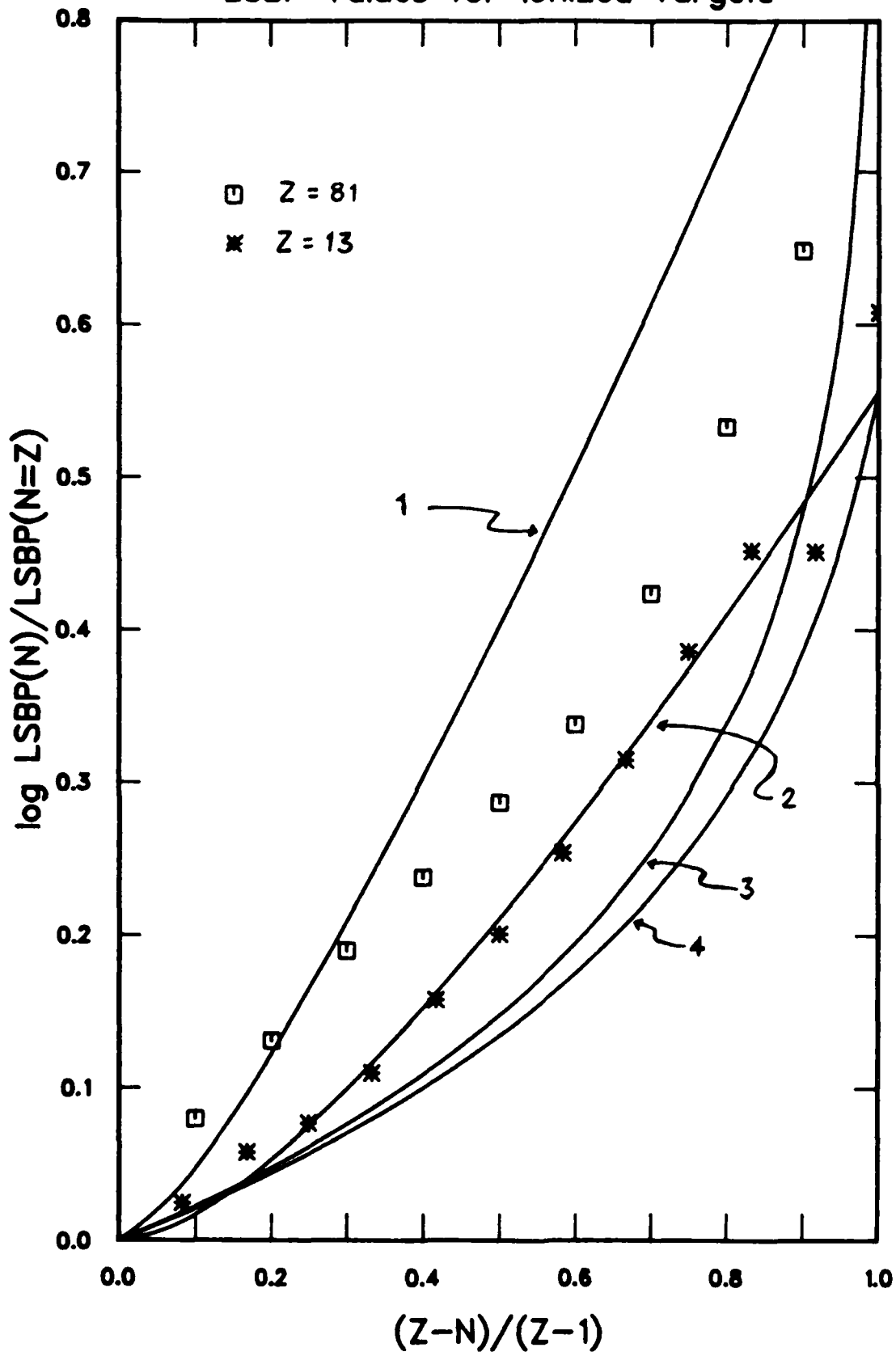


Figure 2

based on partial wave expansions. A point-like effective charge and effective Bethe mean excitation parameter are chosen similar to that suggested by Kim and Cheng.⁶ These reproduce the high velocity atomic calculation without shell corrections (shell corrections are not treated in the Bloch or Barkas terms). The resulting Bloch correction agrees up to a factor of order unity inside a logarithm to a calculation based on Bloch's original derivation¹² in appropriate limits. In this latter model, an effective charge equal to the projectile nuclear charge Z_p is used for close collisions while the net charge $(Z_p - N_p)$ is used for distant collisions. Target ionization effects follow from the use of an effective Bethe mean excitation parameter which tends to reduce the magnitude of the correction as the target is ionized.

Structure is introduced in the Barkas effect again by point-like effective charges: Z_p for close encounters and $(Z_p - N_p)$ for distant ones. However, there is a debate over whether any contribution results from close collisions.¹³ Due to the difference between the net and nuclear charges (and how that may be magnified by the cubic charge dependence of the Barkas effect), structured projectile stopping power provides a good test for the correct model. Our calculations have indicated that it is necessary to include the close collisions. Our model follows that of Deutsch¹⁴ with the impact parameter modified in the usual semi-classical way at lower energies. Target ionization is

taken into account naturally through the LPA and the LSBP. We use the same target wave functions as used in our LPA to the first Born approximation.

Figure 3 shows our initial results for structured projectile stopping in neutral solids. In particular, the results are for 1 MeV helium in various solids. Our results are given by asterisks, Ziegler's tabulations¹⁵ by boxes. The agreement is promising with a maximum difference of about 16%. Solid state wave functions of Moruzzi, Janak and Williams¹⁶ were used to describe the targets. The projectile mean equilibrium charge was taken from calculations by Ohtsuki.¹⁷ A two charge state approximation was used for helium (He^{+2} and He^{+1}) with hydrogen-like wave functions for He^{+1} . The stopping number G is proportional to the stopping power S through

$$S = \frac{4\pi e^2}{m v^2} N_t \rho_{\text{atom}} G$$

with ρ_{atom} = target atom density
 N_t = number of bound target electrons
 e = electron charge
 m = electron mass
 v = projectile velocity

As the target becomes ionized, free electrons contribute to the stopping power. This may be calculated from our high-velocity expansion for bound electrons by replacing the Fermi distribution for a degenerate gas with a Fermi-Dirac distribution of a nondegenerate gas with finite temperature. This was possible by applying the expansion

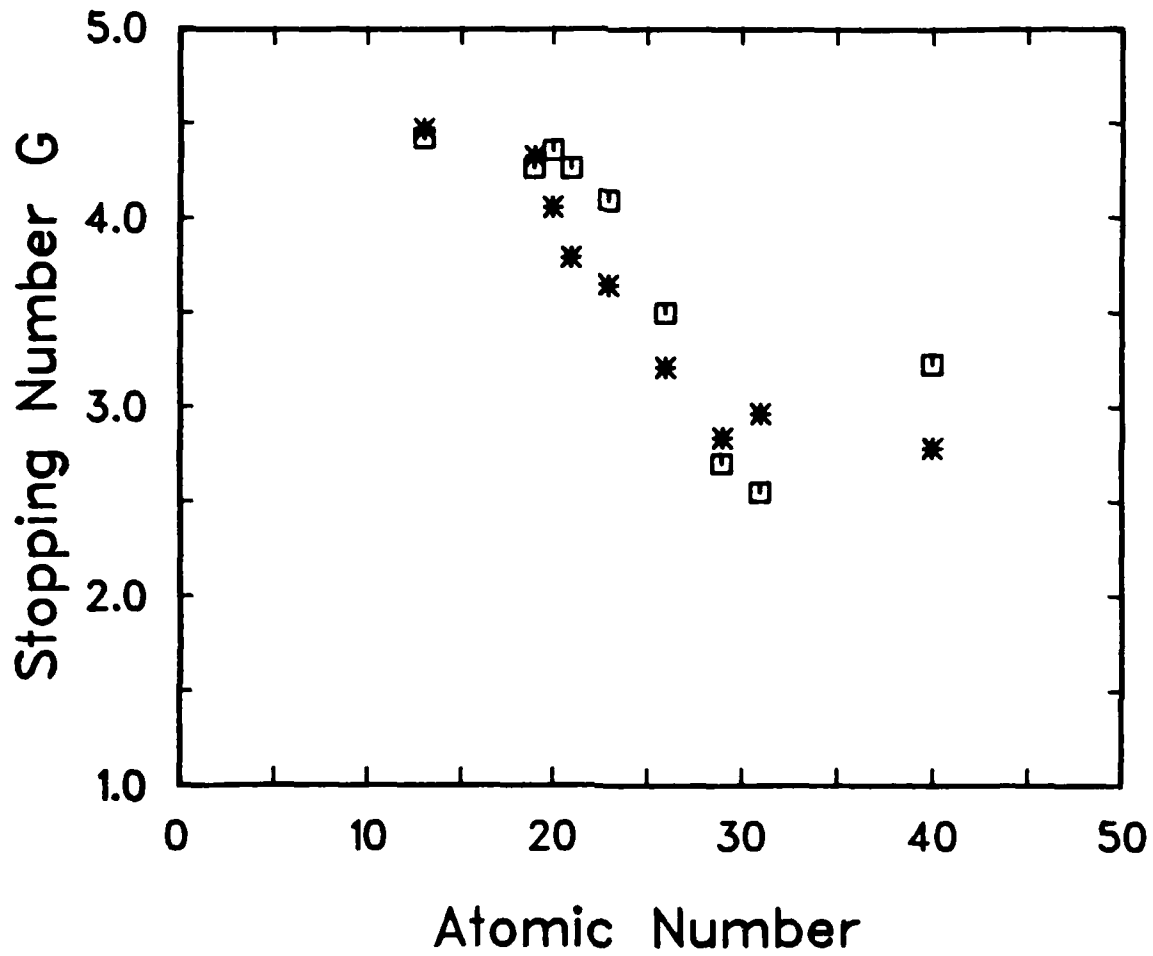


Figure 3 - Stopping number for 1MeV helium in various solids. Our structure calculations (*) and Ref 15 (□).

technique of Sigmund and Fu¹⁸ to structured projectiles. For the special case of bare ions, our result agrees with a temperature dependent calculation of Deutsch¹⁹.

References for Section I

1. E. Bonderup, K. Dan. Vidensk. Selsk. Mat.-Fys. Medd. 35, No. 17 (1967).
2. H. Bethe, Ann. Phys. 5, 325 (1930).
3. U. Fano and J. E. Turner, "Studies in the Penetration of Charged Particles in Matter." NAS-NRC Publ. 1133, 49 (1964).
4. T. L. Ferrell and R. H. Ritchie, Phys. Rev. B16, 115 (1977).
5. J. Lindhard, K. Dan. Vidensk. Selsk. Mat.-Fys. Medd. 28, No. 8 (1954).
6. Y.-K. Kim and K. Cheng, Phys. Rev. A22, 61 (1980).
7. J. Lindhard and M. Scharff, K. Dan Vidensk. Seisk. Mat-Fys. Medd. 27, No. 15 (1953).
8. J. M. Peek, Phys. Rev. A26, 1030 (1982).
9. J. F. Ziegler, Stopping Cross-Sections for Energetic Ions in All Elements, (Pergamon, New York 1980), Vol. 5.
10. J. M. Peek (1985), Private Communication.
11. J. A. Golovchenko et al., Phys. Rev. B26, 2335 (1982).
12. F. Bloch, Ann Phys. 16, 285 (1933).
13. J. Lindhard, Nucl. Instr. Meth. 132, 1 (1976).
14. C. Deutsch, Laser and Particle Beams 2, 449 (1984).
15. J. F. Ziegler, Helium Stopping Powers and Ranges in All Elements (Pergamon, New York 1977) Vol. 4.
16. V. L. Moruzzi et al., Calculated Electronic Properties of Metals (Pergamon, New York 1978).
17. T. Kaneko and Y. H. Ohtsuki, Phys. Stat. Soc. B14, 491 (1982).
18. P. Sigmund and D.-J. Fu, Phys. Rev. A25, 1450 (1982).
19. G. Maynard and C. Deutsch, Phys. Rev. A26, 665 (1982).

I b. COMPUTER SIMULATION OF ION BEAM TARGET DYNAMICS AND RADIATION EMISSION

We have developed a one dimensional computational physics code which simulates the ablation of a carbon target by a proton beam. This is accomplished by coupling a sophisticated collisional-radiative equilibrium (CRE) ionization dynamics model, a one dimensional, single temperature and fluid hydrodynamics model, and an energy deposition model. The total package is then applied to simulating the beam-target interaction under a variety of initial beam conditions. Other applications considered include heating due to inner-shell photon absorption and calculation of the amount of K_{α} radiation emitted by the direct interaction of a beam proton with a target atom.

The basic approach involves coupling a one dimensional hydrodynamic code to an ionization dynamics and an energy deposition model. Because the radiation emitted by the plasma is an important diagnostic tool, we have tried to model the ionization dynamics very carefully. This is accomplished by developing an ionization dynamics model which considers a large number of excited states and atomic processes.

The atomic processes which are considered in our model are:

- 1) collisional ionization
- 2) three body recombination
- 3) collisional excitation
- 4) collisional de-excitation
- 5) spontaneous emission

6) radiative recombination

7) dielectric recombination

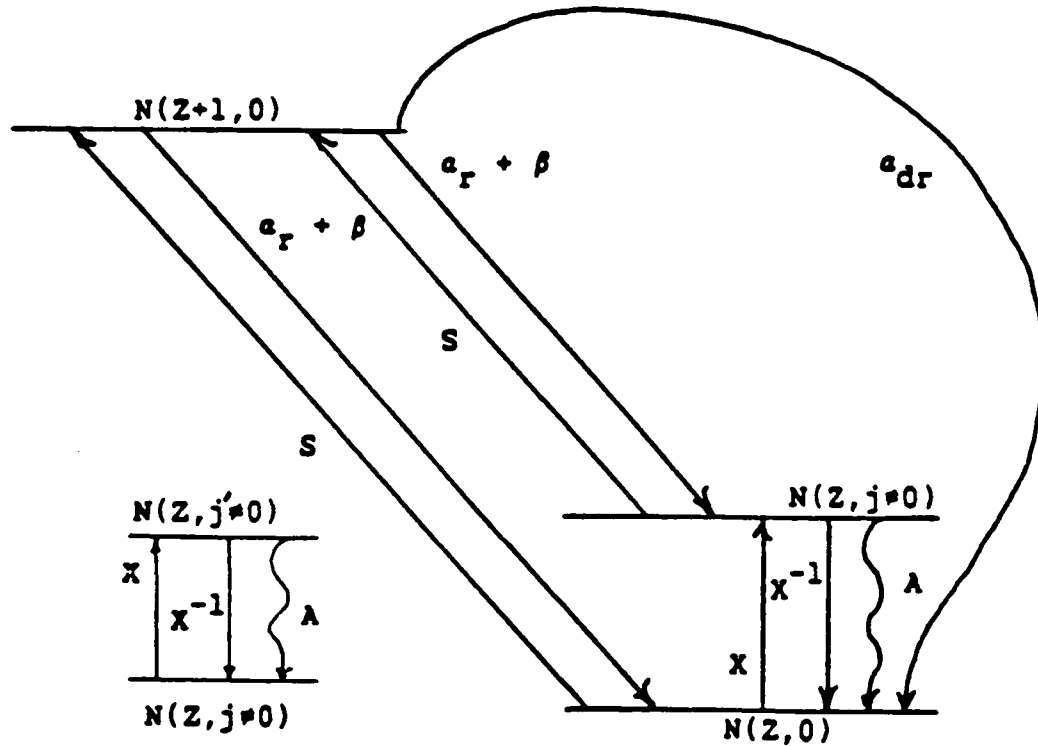
These are incorporated into a set of rate equations which have the form²:

$$\begin{aligned} \frac{N(Z,j)}{dt} = & [N_e N(Z-1,j'') S(Z-1,j'' : Z,j) + N_e N(Z+1,j')] \\ & [\alpha(Z+1,j' : Z,j) + N_e \beta(Z+1,j' : Z,j)] + \\ & \sum_{i>j} N(Z,i) A(i,j) + N_e \sum_{i>j} N(Z,i) X^{-1}(i,j) + \\ & N_e \sum_{i>j} N(Z,i) X(i,j)] \\ & - N(Z,j) [N_e S(Z,j : Z+1,j') + N_e [\alpha(Z,j : Z-1,j'') + \\ & N_e \beta(Z,j : Z-1,j'')]] + \sum_{i>j} A(j,i) + \\ & N_e \sum_{i>j} X^{-1}(j,i) + N_e \sum_{i>j} X(j,i)] \end{aligned}$$

where $N(Z,j)$ is the population density of ion species Z in level j , $S(Z-1,j''; Z,j)$ is the collisional ionization rate (cm^3/sec) from $N(Z-1,j'')$ to $N(Z,j)$, α is the sum of the radiative and dielectronic recombination rates ($\alpha_r + \alpha_{dr}$) in cm^3/sec , β is the collisional recombination rate (cm^6/sec), $A(i,j)$ is the spontaneous decay rate from levels i to j ($1/\text{sec}$), $X(i,j)$ is the collisional excitation rate from i to j (cm^3/sec) and X^{-1} is the inverse reaction, collisional de-excitation.

(Note that since this is an equilibrium model, the left hand side of the above equation is set equal to zero.)

Schematically, the transitions and atomic processes considered in this model are:



In this form the model consists of an infinite set of coupled non-linear equations, one for each available state of the ions and atoms present in the plasma. Fortunately, there are some methods and procedures available for truncating the number of states. Though we are not explicitly considering reduction in ionization potentials in this model, this phenomenon still sets an upper bound on the number of

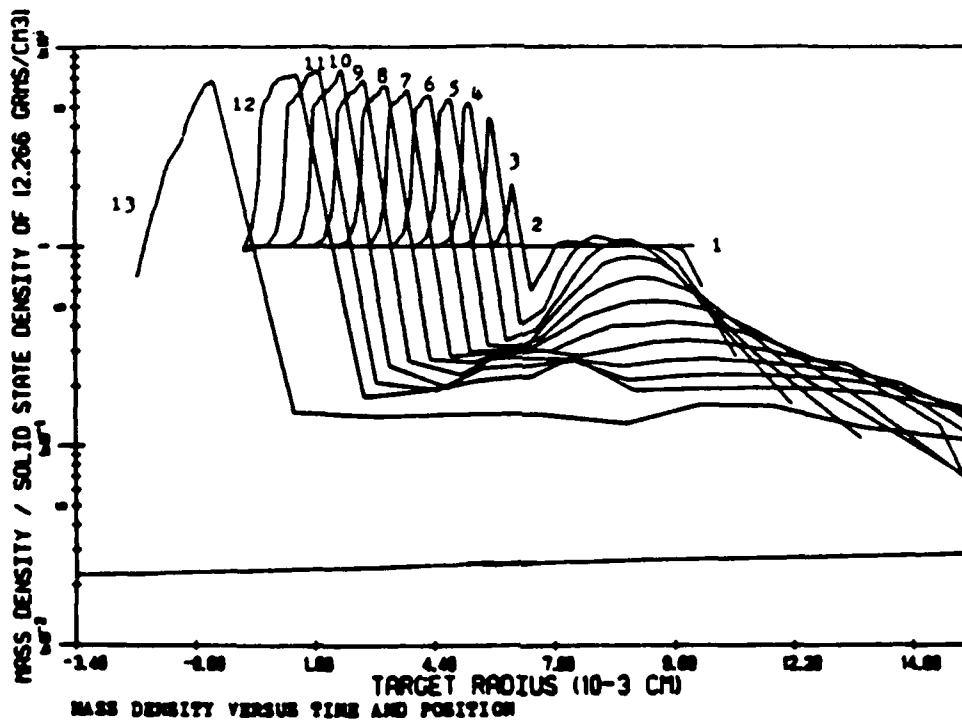
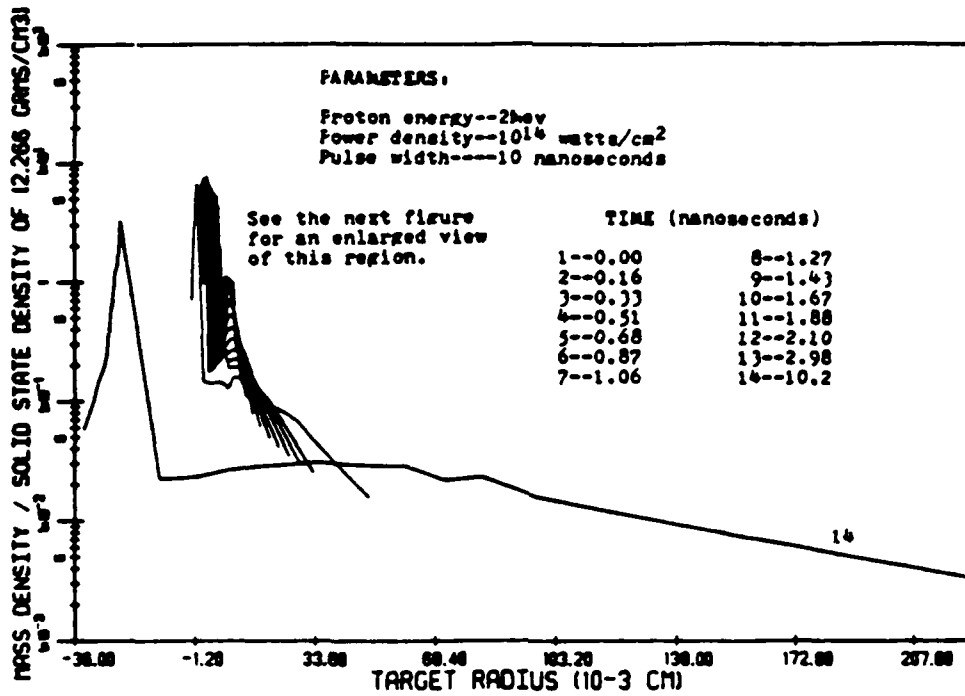
discrete quantum states available, i.e., we only need model those states for which $E(n) < E(Z) - \Delta E(Z)$.

In our model we have considered only the 5-10 lowest states for each ionization stage of carbon, including neutral carbon. Although a limited number of states have been considered in this model, they should still be adequate for modelling the radiation field, specific heats and other equations of state information needed for the beam - target simulations.

We have shown that the CRE model is applicable over the range of plasma conditions considered in this work, i.e., for temperatures between 1 and 100 ev and ion densities between 10^{19} and 10^{24} cm^{-3} . Both the CRE and LTE models give identical results for collisionally dominant plasmas. Similarly, the CRE model exhibits coronal behavior in the low density limit. This ability to model both collisional and radiative plasmas is essential for a comprehensive ionization dynamics model.

In addition, we investigated the time constraints placed upon the overall simulation. In particular this consists of a consideration of the equilibrium aspects of the CRE model and the single temperature and fluid assumptions inherent in the hydrodynamics code. In all cases, we found that the models are valid for the timing limitations encountered in this study.

We have calculated temperature, density and pressure profiles for evolving targets. We find that the deposition region heats very rapidly until the processes of electron thermal conduction, radiative loss and beam deposition begin to equilibrate. Once this occurs, we find that the pressure across the width of the deposition region remains fairly constant during the interaction. The pressure is responsible for



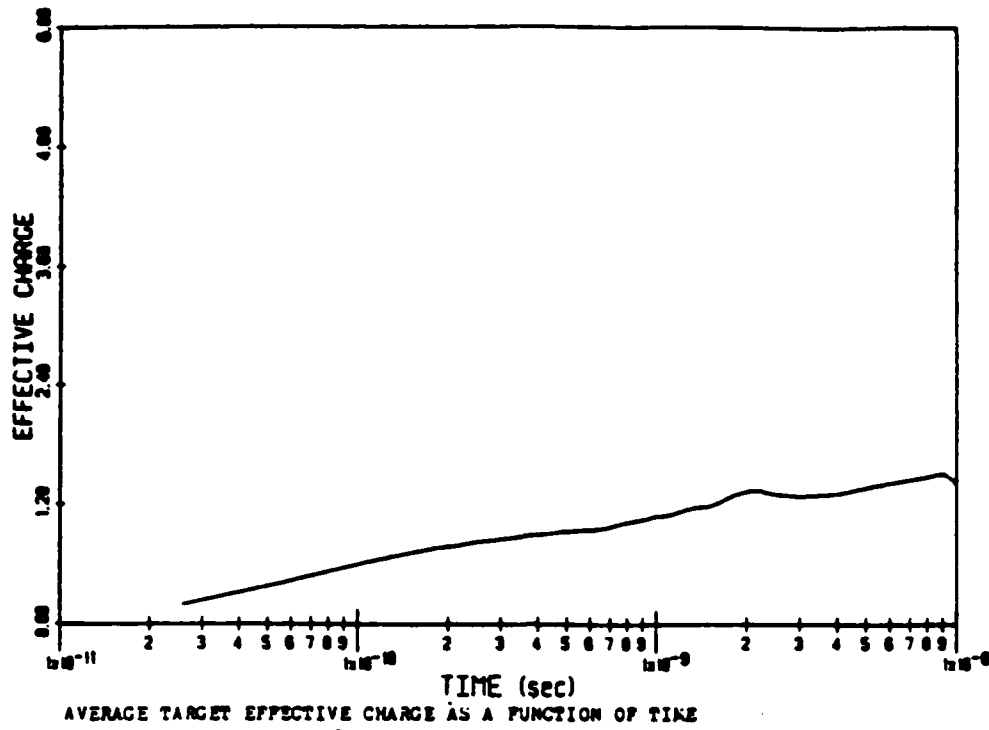
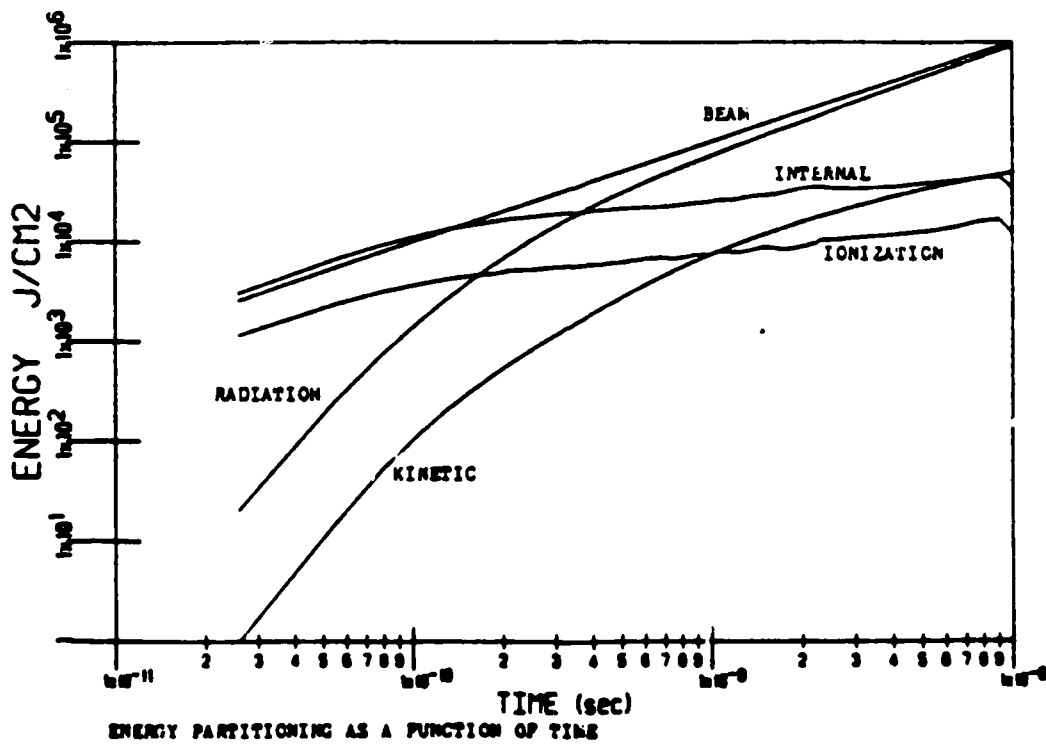


FIGURE 4.46



compression of the nondeposition region to densities as high as five to ten times solid state. We provide diagnostic information that displays various transition energies and power densities during the ablation. In addition, the partitioning of the deposited energy into internal, kinetic and radiative components is examined. This model can be applied to a variety of plasma and beam conditions. The plasma restrictions have already been mentioned, and the beam conditions must be such that the energy and power density is sufficient to heat the target to at least several eV (1 eV represents the lower bound of the rate coefficient table).

An examination of the results of our parameter study suggests the direction one might take in order to tailor the energy partitioning of the radiation field or ablation region for a specific application. For example, if carbon is to be used as a x-ray laser pump, then one might want to optimize the radiation conversion efficiency or the shape of the emission profile. In our work, we find that conversion efficiencies can be as large as 90%. We also find that the thermal emission profile is dependent upon both the energy and power density of the beam. This is illustrated by the observation that the hardness of the radiation field can be increased by either using less energetic protons and maintaining the same power density or else increasing the power density. The parameter study also categorizes the dependence of internal, kinetic and radiative energy upon beam power density and proton energy. The radiation field is further divided into relative contributions of line, recombination and bremsstrahlung radiation.

We also investigated the effects of including the inner-shell photon absorption process. This is the only radiation transport we considered

PARAMETER STUDY
(Power density is 10^{12} w/cm²)

PLASMA "ENERGY" PARAMETERS	INITIAL ION ENERGY 1 Mev	INITIAL ION ENERGY 2 Mev	INITIAL ION ENERGY 3 Mev
-------------------------------	--------------------------------	--------------------------------	--------------------------------

ENERGIES IN UNITS OF (10^3 J/CM²) AND
(% OF TOTAL BEAM ENERGY) ARE LISTED

BEAM	9.0 (100%)	9.0 (100%)	9.0 (100%)
INTERNAL(*)	1.9 (21%)	2.7 (30%)	3.2 (36%)
KINETIC	1.2 (13%)	1.1 (12%)	.95 (11%)
RADIATIVE	5.9 (65%)	5.2 (58%)	4.9 (54%)
***	***	***	***
IONIZATION	.87 (10%)	1.0 (11%)	1.3 (14%)
LINE	3.0 (32%)	2.4 (27%)	2.4 (27%)
RECOMBINATION	1.8 (20%)	1.4 (15%)	1.2 (14%)
BREMSSTRAHLUNG	1.2 (13%)	1.4 (15%)	1.3 (14%)

LINE SPECTRUM ENERGIES (% OF RADIATIVE ENERGY)

E<10ev	3%	7%	13%
10<E<20ev	15%	26%	28%
20<E<60ev	31%	13%	8%
60<E<100ev	***	***	***
100<E<200ev	***	***	***
200<E<350ev	***	***	***
E>350ev	***	***	***

RECOMBINATION SPECTRUM ENERGIES (% OF RADIATIVE ENERGY)

E<10ev	***	1%	5%
10<E<20ev	17%	15%	13%
20<E<60ev	13%	9%	6%
60<E<100ev	***	***	***
100<E<200ev	***	***	***
200<E<350ev	***	***	***
E>350ev	***	***	***

* Ionization energy is included in internal energy

PARAMETER STUDY
Power density is 10^{14} w/cm²)

PLASMA "ENERGY" PARAMETERS	INITIAL ION ENERGY 1 Mev	INITIAL ION ENERGY 2 Mev	INITIAL ION ENERGY 3 Mev
-------------------------------	--------------------------------	--------------------------------	--------------------------------

ENERGIES IN UNITS OF (10^5 J/CM²) AND
(% OF TOTAL BEAM ENERGY) ARE LISTED

BEAM	9.0 (100%)	9.0 (100%)	9.0 (100%)
INTERNAL(*)	.89 (10%)	.45 (5%)	.52 (6%)
KINETIC	.49 (5%)	.47 (5%)	.45 (5%)
RADIATIVE	7.7 (85%)	8.2 (91%)	8.1 (90%)
***	***	***	***
IONIZATION	.22 (2%)	.17 (2%)	.18 (2%)
LINE	2.3 (25%)	2.6 (29%)	1.5 (17%)
RECOMBINATION	4.8 (53%)	4.1 (45%)	3.9 (43%)
BREMSSTRAHLUNG	.60 (7%)	1.5 (17%)	2.6 (29%)

LINE SPECTRUM ENERGIES (% OF RADIATIVE ENERGY)

E<10ev	***	***	***
10<E<20ev	***	***	***
20<E<60ev	2%	6%	11%
60<E<100ev	***	***	***
100<E<200ev	***	***	***
200<E<350ev	8%	14%	4%
E>350ev	14%	11%	3%

RECOMBINATION SPECTRUM ENERGIES (% OF RADIATIVE ENERGY)

E<10ev	***	***	***
10<E<20ev	***	***	***
20<E<60ev	***	4%	20%
60<E<100ev	8%	20%	19%
100<E<200ev	19%	18%	8%
200<E<350ev	5%	***	***
E>350ev	30%	7%	1%

* Ionization energy is included in internal energy

in our otherwise "optically thin" model. The results of the study show that as much as 10% of the radiation field can be absorbed by the inner-shell process. Although, for an optically thick application this value would be reduced because of competition with valence photo-processes, it still represents an important absorption mechanism for recombination radiation. An examination of the temperature, density and pressure profiles show that inner-shell photon absorption primarily affects the temperature and density profiles of the ablation region. The nondeposition region appears to be insulated from its effects; thermal conduction and ion shock heating remain the principal heating mechanisms in this region.

Another application investigated was the calculation of the amount of K_{α} photon energy emitted by the direct interaction of the beam protons with the target atoms. We found that under optically thin conditions, the energy density of the emission is several orders of magnitude below that of the primary radiation field. However, since the energy of the K_{α} is larger than the other photons, it should be easily resolvable. It was noted that this situation only arises when the target is relatively cold. Otherwise, there will be a significant component of high energy photons created by valence transitions that will also be absorbed by the K shell. When this happens, additional K_{α} emission is produced and it washes out the beam K_{α} results. Because the spectrum of K_{α} depends upon the binding energy of the K shell electron of the emitting atom, it represents a measure of the ionization state of the target.

In conclusion, we feel that this model contains enough essential physics to be useful for analyzing a variety of processes that occur

during the ablation of a carbon target. The processes which we examined in this investigation included: 1) the effects of initial beam conditions on plasma parameters such as kinetic, internal and radiative energy, 2) inner-shell photon absorption and 3) K_{α} emission due to the direct interaction of the beam particles with target atoms. With the implementation of the suggestions for improvement listed above, the model should be adequate for providing accurate diagnostic information for a variety of physical problems.

II. Experimental Progress

IIa) Neutral/Ion Interactions with a Laser Ablation Plasma

The attenuation of beam current density is governed by the product of plasma density and interaction cross section integrated over the beam particle path length in the plasma, illustrated in Figure 1. While Coulomb collisions account for the attenuation of an ion beam, neutral particles may undergo charge exchange, momentum scattering, and impact ionization with plasma ions, along with ionization by impact with plasma electrons. The Coulomb cross section is calculated from an expression obtained by integration of the Rutherford scattering formula. Of the neutral interaction cross sections, the charge exchange cross section appears to be the largest and is to date the only one for which we have found adequate experimental and theoretical treatment in the literature¹ ($H^0 + C^{+q}$ interactions). For a 10 keV hydrogen atom in a C^{+q} plasma, we estimate for the total neutral interaction cross section

$$\sigma_{CX} \approx 5 \times 10^{-15} \text{ cm}^2$$

Beam attenuation predictions are presented in Figure 2 for the case of 10 keV protons or hydrogen atoms traveling 20cm through a quiescent, 20eV carbon plasma of various densities. Fokker-Planck calculations of initial beam particle slowing down (τ_s) and diffusion (τ_b) times indicate that path lengths much greater than 20 cm would be required for the beam particles to acquire an isotropic velocity distribution and to thermalize with the plasma, since a 10 keV proton will travel 20 cm in about 140 ns. However, since the Coulomb cross section is so large for the conditions considered, all beam



Ion beam attenuation:

$$I(t) = I_0 \exp \left\{ - \int n_p \sigma_c dl \right\}$$

where σ_c = Coulomb scattering cross section

Neutral beam attenuation:

$$I(t) = I_0 \exp \left\{ - \sum_{i,z} \sigma_{i,z} \int_{l_p} n_{i,z} dl - \frac{\langle \sigma_e v_e \rangle}{v_b} \int_{l_p} n_e dl \right\}$$

where $\sigma_{i,z}$ = cross section for charge exchange, σ_{cx} ,
 + momentum scattering, σ_s ,
 + impact ionization, σ_{ii} ,
 with plasma ions of species i ,
 charge z , and density $n_{i,z}$;

$\langle \sigma_e v_e \rangle$ = electron impact ionization cross section averaged over the electron velocity distribution;

v_b = beam particle velocity;

l_p = beam path length in the plasma.

Figure 1 - Plasma attenuation of a particle beam.

ions will undergo Coulomb collisions while traversing the plasma and hence will be lost from the beam. With 10 keV hydrogen atoms, on the other hand, we predict significant attenuation by charge exchange interactions to occur for plasma line densities greater than about 10^{12} cm^{-3} .

With the assumption of cross sections which are independent of space and time, we see in Figure 1 that the time behavior of the beam current density exiting the plasma depends on the time behavior of the integral of plasma density over beam particle path length in the plasma, which is defined in terms of the line density along the particle beam axis. An expression for the line density resulting from the production of a laser ablation plasma is obtained from the integration of Tallents' expression² for the ablation plasma ion density, presented in Figure 3. The laser beam is taken to be perpendicular to both the particle beam axis and the target surface. The buildup and decay of the line density after firing the laser is also presented in Figure 3.

I Ib) Duopigatron Based Experiments Concerning Neutral/Ion Beam Interactions with Laser Ablation Plasmas

During the past year our experimental efforts have been concentrated toward the measurement of the effects of an independently-produced ablation plasma upon the penetration of a neutral or ion beam to an underlying surface. This problem has relevance to the case of a plasma or gas cloud surrounding an outgassing material in a space vacuum environment.

● 10 keV proton beam, C⁺ plasma*

$\sigma \sim \sigma_c$ (Coulomb scattering), $KT \sim 20$ eV

n [cm ⁻³]	σ_c [cm ²]	τ_s [s]	τ_D [s]	l_{mfp} [cm]	$\frac{I}{I_0}$
10^{11}	5×10^{-4}	2×10^{-2}	2.55	2×10^{-8}	~ 0
10^{12}	4×10^{-5}	2×10^{-3}	0.28	2×10^{-8}	~ 0
10^{13}	5×10^{-6}	2×10^{-4}	0.03	2×10^{-8}	~ 0
10^{14}	4×10^{-7}	2×10^{-5}	0.003	2×10^{-8}	~ 0

● 10 keV neutral hydrogen beam, C⁺ plasma*

$\sigma \sim \sigma_{cx} \sim 5 \times 10^{-15}$ cm² (ref. 1)

n [cm ⁻³]	l_{mfp} [cm]	$\frac{I}{I_0}$
10^{11}	2000	0.99
10^{12}	200	0.90
10^{13}	20	0.37
10^{14}	2	~ 0

*Assumed uniform and stationary ($\bar{n} = nL$, $L = 20$ cm)

Figure 2- Beam attenuation predictions.

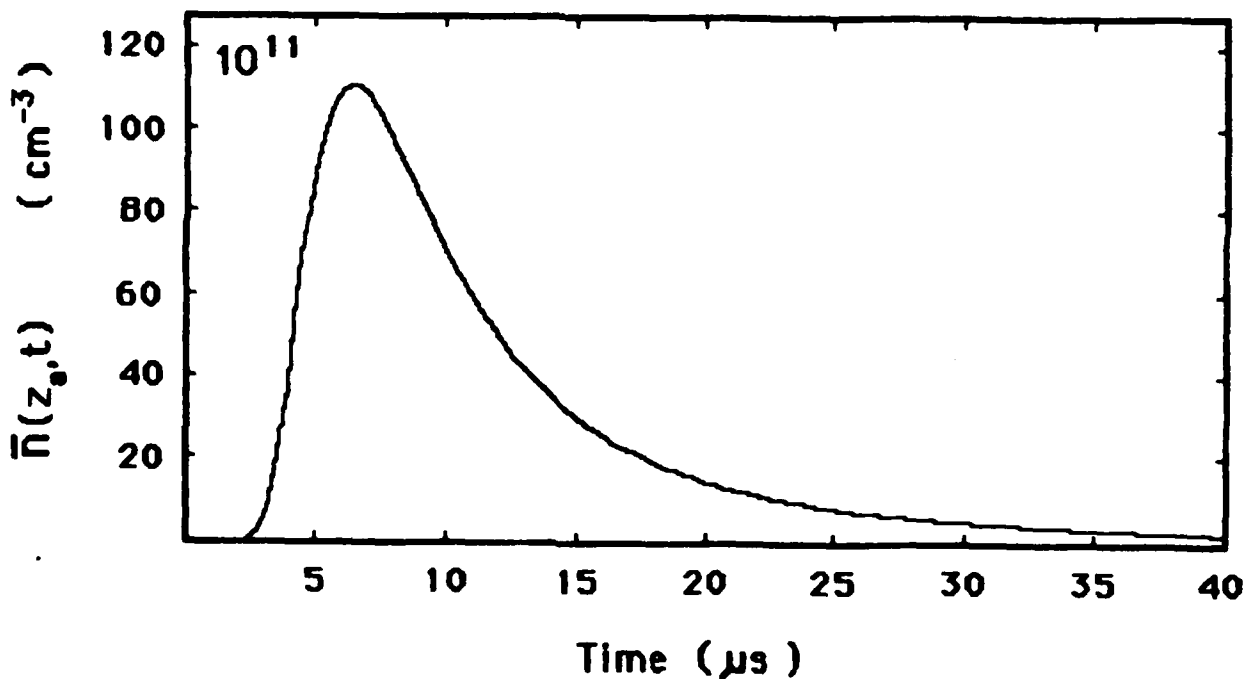
Ion number density :

(G. J. Tallents, Laser and Particle Beams (1983),
Vol. 1, Part 1, pp. 171-80.)

$$n(R, \theta, t) = \frac{2\pi^{-3/2} N_T k^2}{(v_z^0)^3 t^3} \exp \left\{ \frac{-R^2 [(k^2 - 1) \sin^2 \theta + 1]}{(v_z^0)^3 t^3} \right\}$$

Line density along particle beam axis, located a distance z_0 from target surface:

$$\bar{n}(z_0, t) = \int n(z_0, \theta, t) dl$$



Conditions: $z_0 = 1$ cm, $L = 20$ cm, $v_z^0 = 5 \times 10^6$ cm/s,
 $k = \frac{v_z^0}{v_r^0} = 4$, $N_T = 10^{15}$ ions.

Figure 3 - Self-similar expansion model for laser-produced target plasma.

IIb.1) Beamline and Vacuum Systems

The duopigatron based experiment has been completely disassembled and renovated for these experiments. What was needed for these interaction experiments was a highly collimated ion or neutral beam to interact with the expanding carbon ablation plasma produced by a ruby laser. A floor plan showing the present location of the components in this experiment is shown in Figure 4. Major components and changes in the system will be discussed in the following sections.

The neutral beam device is depicted as it existed immediately following its renovation in Figures 5 and 6. Large port gate valves are used to isolate components of the system. The beamline expands from the 10.2 cm diameter opening between the neutralization tank and the vertical gate valve to the 15.2 cm diameter opening into the target chamber, which is a 29 cm diameter, 33 cm long stainless steel tank. Following vacuum leak and electrical system checks, 10 kV hydrogen beams were extracted and monitored to verify proper operation.

In order to place diagnostics so as to monitor the beam after passage through a target plasma, a number of changes were made to the system. First, in order to avoid filling the target chamber with a background plasma produced by passage of the beam into the chamber, and to better collimate the particle beam entering the chamber, a 3 cm aperture was placed at the chamber entrance. Better results were obtained by adding two more apertures, one just after the vertical gate valve and another just after the second pumping station. This arrangement provided both a collimated particle beam and differential pumping.

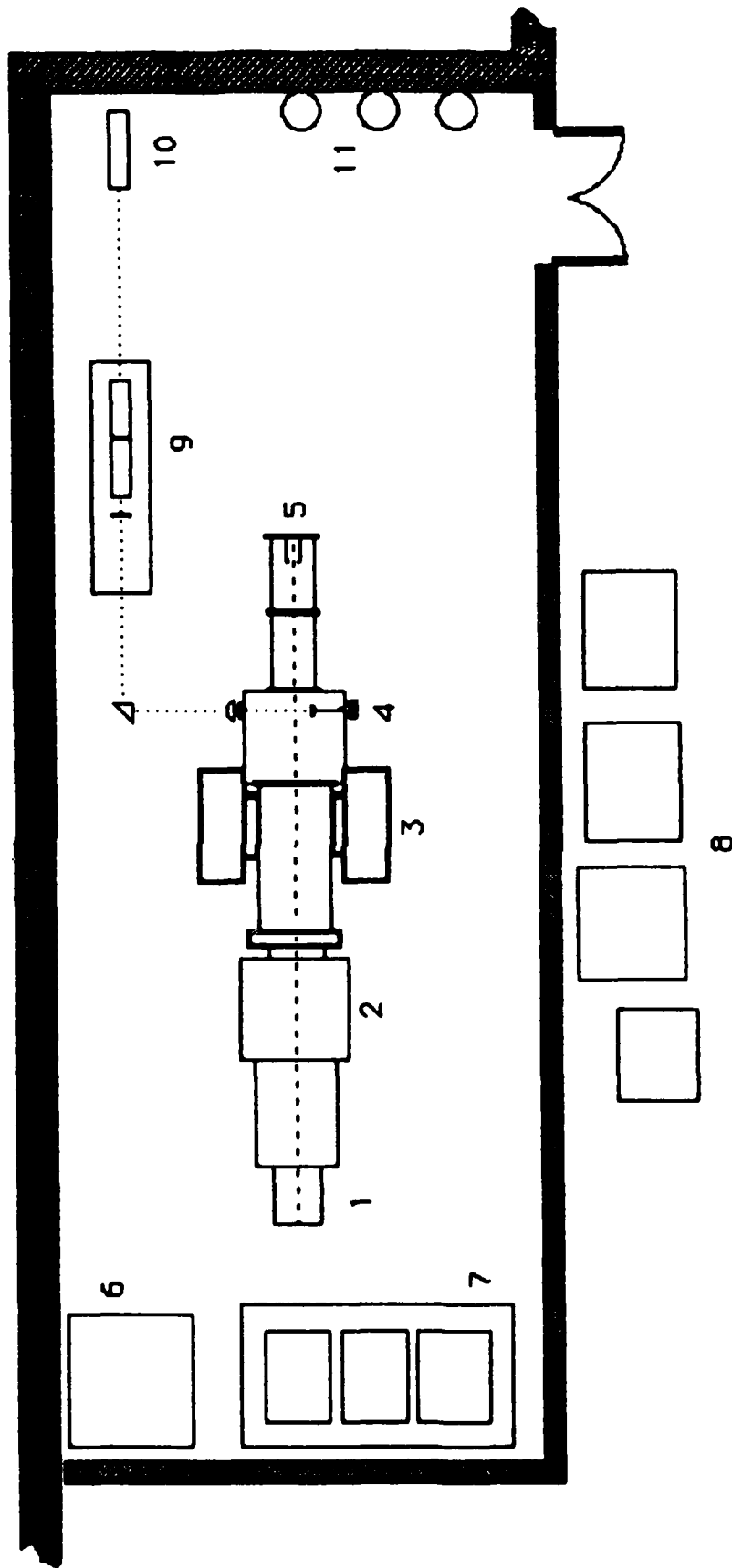


Figure 4 - Components of the beam interaction experiment. Shown is (1) the duopigatron, (2) neutralization cell, (3) bending magnets, (4) target chamber, (5) particle detector, (6) isolation transformer, (7) isolated power supplies, (8) controls, (9) ruby laser, (10) HeNe laser, (11) gas bottles. Not shown is the high voltage power supply located in a separate interlocked room.

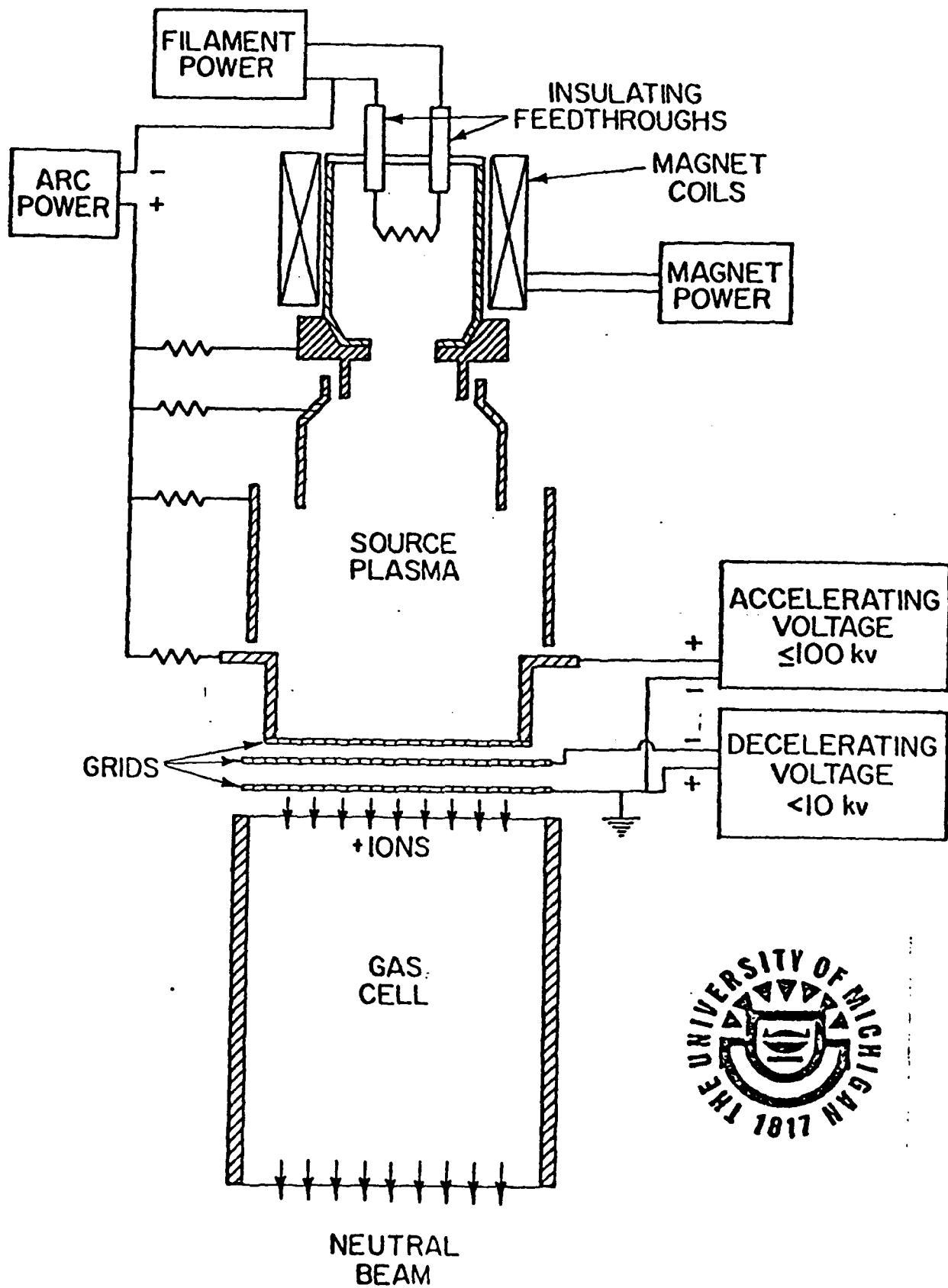


Figure 5 - Schematic illustration of duoPIGatron type positive ion source with accelerating grids and neutralizing gas cell.

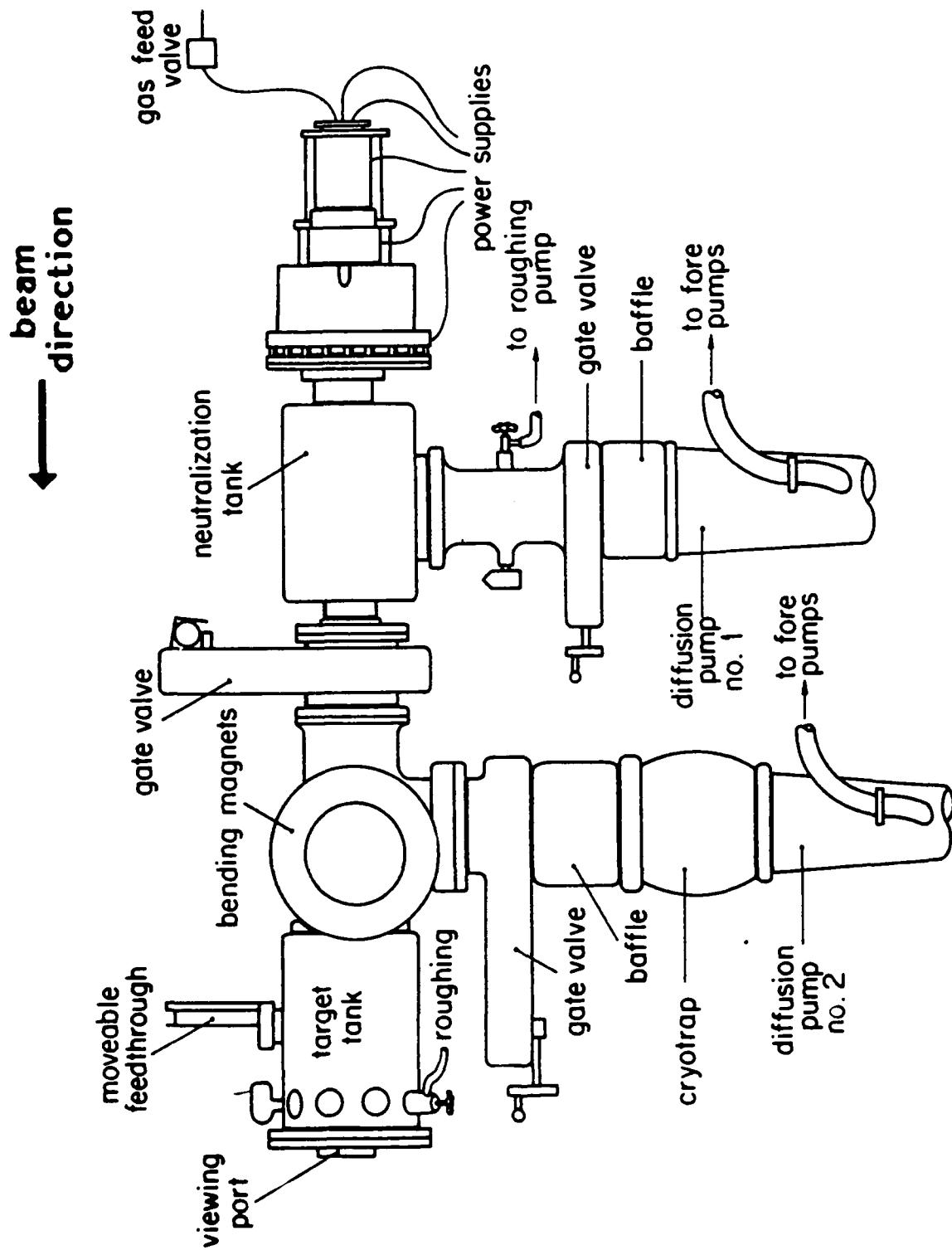


Figure 6 - Duopigatron and beamline as constructed at the beginning of this reporting period.

Pressure in the target chamber remains below 10^{-5} Torr while the pressure in the duopigatron end rises to nearly 10^{-3} Torr when a beam is extracted. Second, since the experimental targets are to be located in the plane defined by the 11 ports arranged circumferentially near the end of the chamber, a 10 cm I. D. Pyrex cross was attached to the target chamber end flange to allow the mounting of diagnostics downstream of the target. Initial experiments using this arrangement indicated the need to move the diagnostics further away from the target, due to target plasma streaming and particle beam timing, and so a second Pyrex section was placed between the first one and the chamber end flange. Further studies indicated the need for additional apertures to be placed between the target plasma and the Pyrex system along with a reduction of the size of the aperture at the entrance to the target chamber. The aperture into the Pyrex system made it necessary to install a third vacuum pumping station. The target end of the neutral beam device, as of the end of this reporting period, is illustrated in Figure 7.

I Ib.2) Ruby Laser System

A target plasma is produced in the target chamber by focusing the output of a Korad K-15 ruby laser onto a solid target mounted within the chamber on the end of a rotatable feedthrough. A 29 cm focal length lens is mounted external to the vacuum system and the laser beam passes through a glass window. A prism is used to turn the laser beam and a HeNe laser is used to align the laser system components, which are

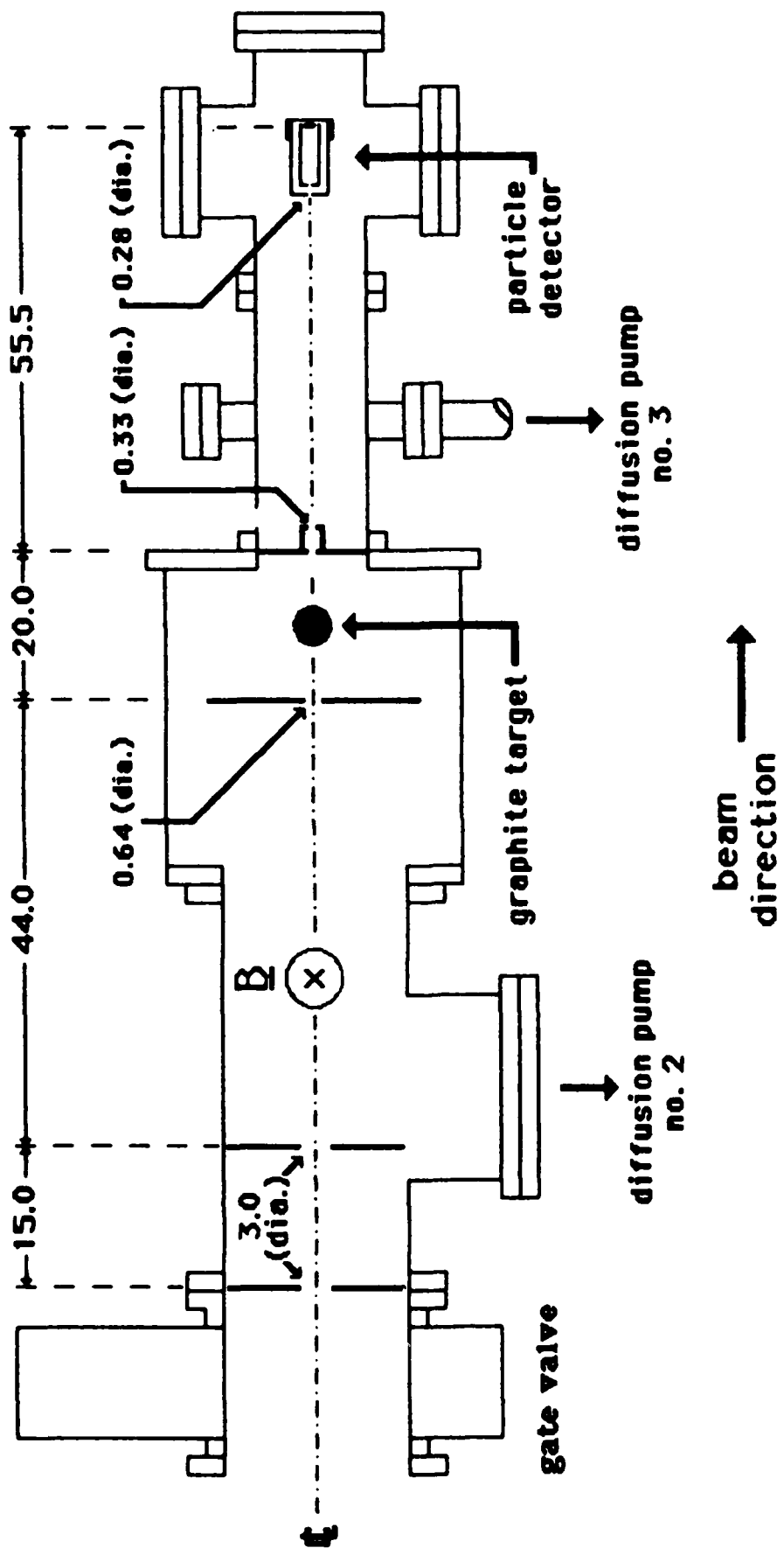


Figure 7 - Target end of beamline. (dimensions in cm)

shown in Figure 4. A pockels cell allows conversion of the laser output from the relaxation mode to the Q-switched mode.

I Ib.3) Diagnostics

Beam attenuation data is obtained by the use of a Faraday cup type of particle detector, illustrated in Figure 8. In this device, an energetic particle (ion or neutral) strikes the collection plate, which then emits secondary electrons. The secondary electrons are collected by the innermost cup, which is typically biased at +15 VDC. The outer cups define the collector's acceptance angle and help to shield the innercup from any charged background particles. Ions collected on the emitting plate and electrons leaving the plate produce a measurable voltage signal across the resistor shown in the figure.

Other beam parameters monitored during each shot are: 1) Arc current, I_{arc} , the current flowing from cathode to anode in the duopigatron; 2) Drain current, I_{drain} , the current drawn by the accelerator grid; and 3) Accelerator voltage, V_{accel} , the voltage applied to the accelerator grid. Arc current is obtained by measuring the voltage across a shunt resistor, drain current is obtained through the use of a Pearson coil on the transmission line between the high voltage capacitor and the accelerator grid, and the voltage on the accelerator grid is measured with a high voltage probe.

I Ib.4) Ion and Neutral Beam Probe Measurements

The first task performed after the renovation and subsequent system checkout was to determine the parameters of the particle beam in order to adjust the geometry of the interaction

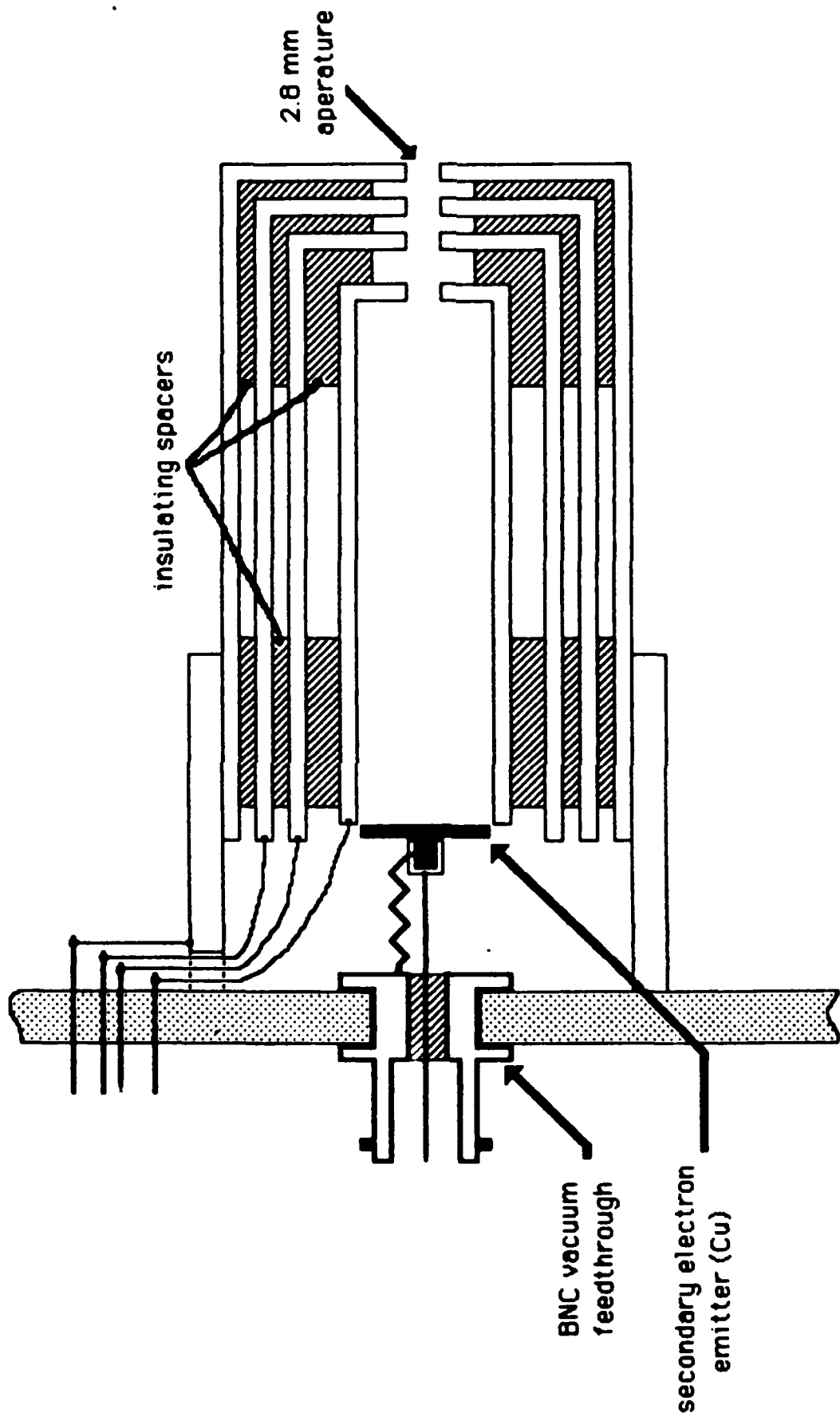


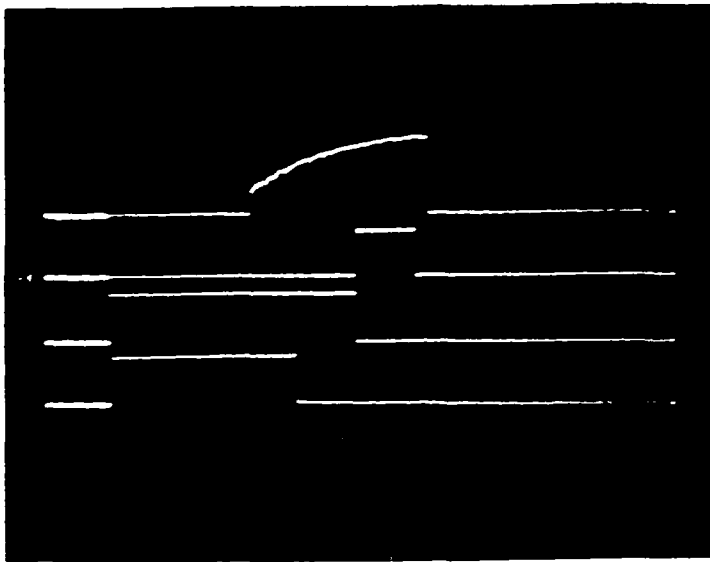
Figure 8 - The particle detector as mounted on a plexiglass end flange.

experiment. In preparation for the target interaction experiments, a Pyrex tee was attached to the target chamber end flange and the detector was mounted on a movable feedthrough. A ruled marker was used to indicate the cup position relative to the beamline axis and the cup was repositioned between shots to scan across the beam diameter.

Typical oscilloscope traces showing the timing and beam parameters for 20 amp arc discharges and an accelerating voltage of 10 kV are presented in Figure 9.

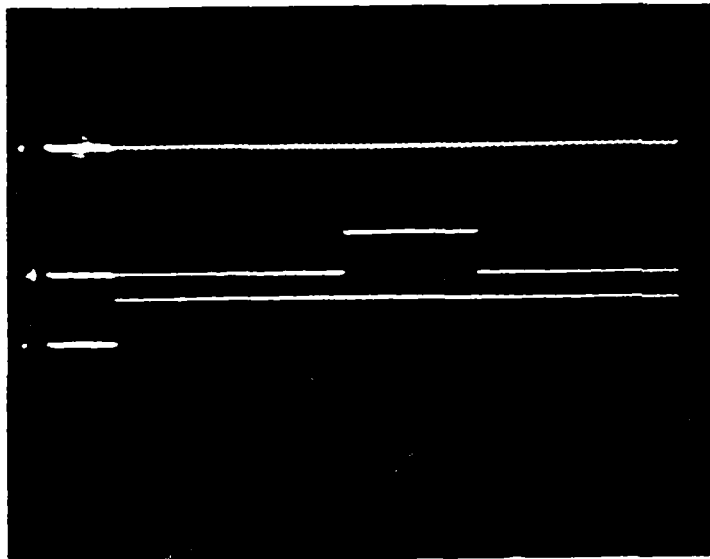
Figure 10 presents the results of a vertical scan of beams after having passed through the single 3 cm aperture for both 0 and 5 amps of bending magnet current (0 and approx. 180 Gauss). The factor of three decrease in the peak signals for such a low bending magnet current indicates that the beam ion fraction is quite high and the degree of beam divergence is indicated by the width of the curves: For these non-optimal conditions, more than 70% of the beam particles entering the target chamber are ions and the beam expands from 3 cm to about 6 cm in diameter in a distance of 37 cm. Fixing the cup position at 2 cm from the beamline axis and varying the current through the bending magnets yielded the results presented in Figure 11. This shows that 20 amps (approx. 700 Gauss on axis) removes all but the heaviest of beam contaminants and, again, that only about 30% of the beam particles are charge neutral.

Figures 10 and 11 were obtained from operation of the source with a relatively high hydrogen gas feed rate (gas



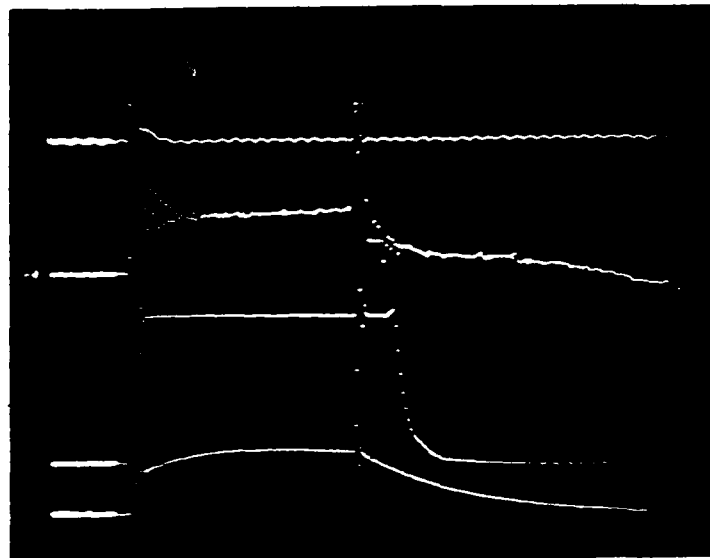
A. 0.1 s/cm

- 1 - I_{arc} , 5 V(20 A)/cm
- 2 - flashlamp trigger, 5 v/cm
- 3 - arc voltage gate, 5 V/cm
- 4 - gas feed gate, 5 V/cm



B. 200 μ s/cm

- 1 - I_{arc} , 5 V(20 A)/cm
- 2 - accelerating voltage trigger, 5 V/cm (crowbarred 400 μ s later)
- 3 - flashlamp trigger, 5 V/cm (Q-switched 1 ms later)



C. 100 μ s/cm

- 1 - I_{arc} , 5 V (20 A)/cm
- 2 - I_{drain} , 50 mV (0.5 A)/cm
- 3 - I_{detec} , 2 V (0.8 μ A)/cm
- 4 - V_{accel} , 5 V/cm (x 2000)

Figure 9 - Typical hydrogen beam parameters.

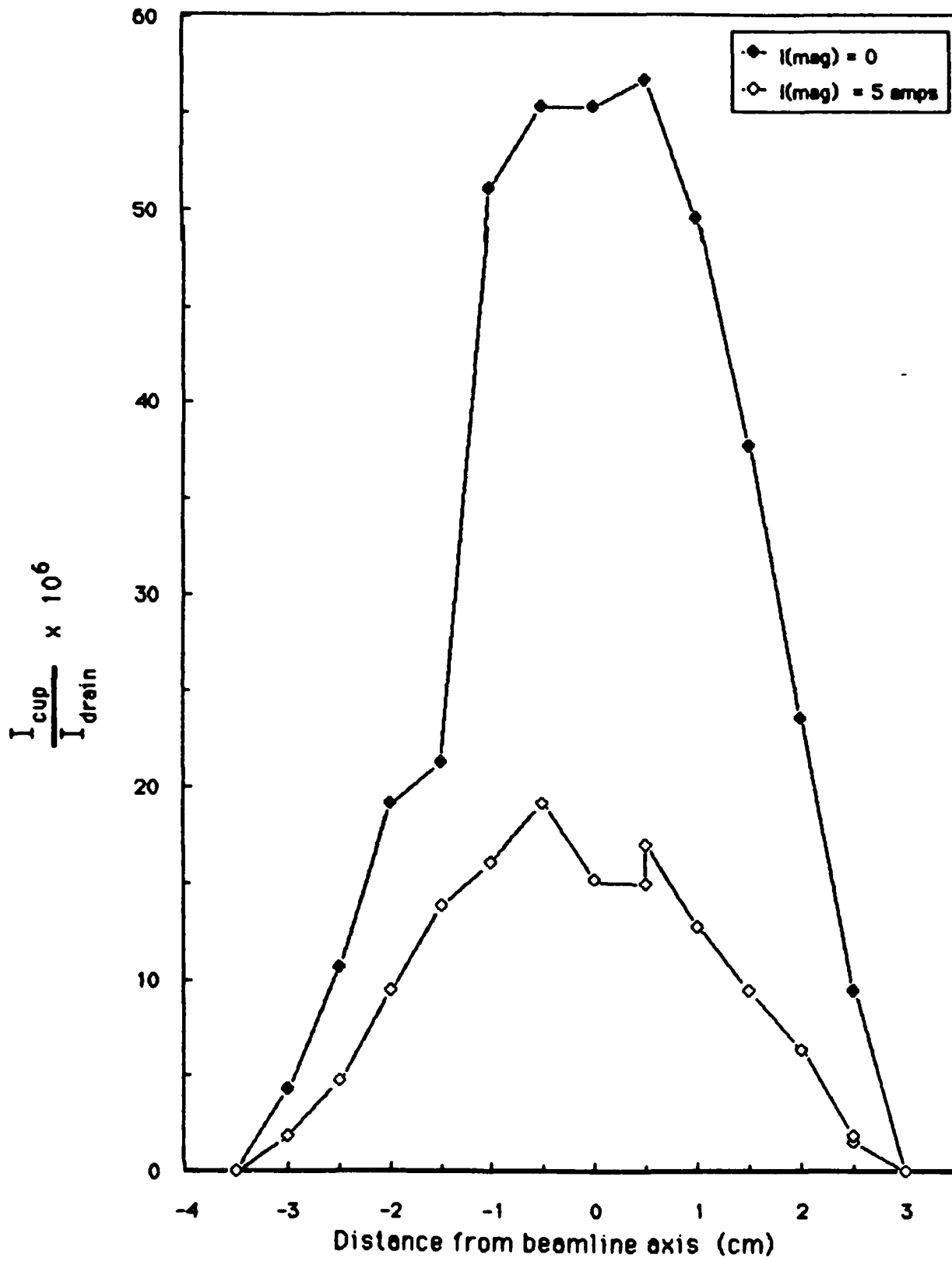


Figure 10 - Beam profile using a single 3 cm aperture.

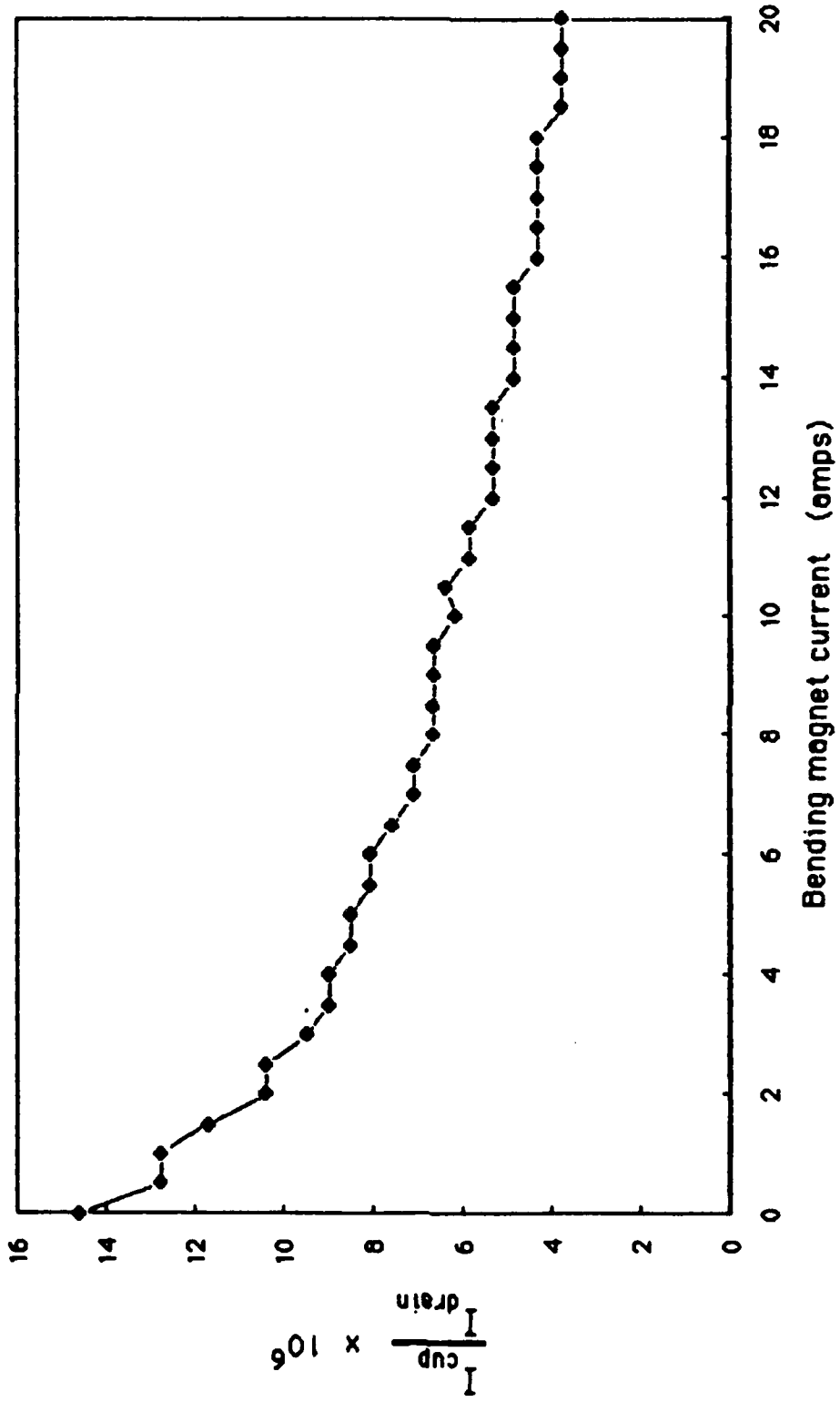


Figure 11 - Normalized detector current vs. bending magnet current.

valve setting = 100). In an effort to increase the beam neutral fraction and to improve beam collimation, two additional 3 cm diameter apertures were placed in the beamline as shown in Figure 7. With the detector placed on the beamline axis, 10 kV hydrogen beams were again extracted from 20 amp arc discharges, this time varying the gas feed rate. Results for bending magnet currents of 0 and 20 amps are presented in Figure 12, which show that the neutral fraction of the beam increases as the gas feed rate decreases, as expected, since there are fewer background particles available for the neutrals to charge exchange with (back into ions) in the beamline. However, there is a lower bound on the gas feed rate and gas pulse length, below which there is no source plasma buildup. This limit appears to be at a gas valve setting of approximately 50 and a gas pulse length of about 0.3 seconds for the aperture placement shown in Figure 7. Discharges at this operating point are very unstable.

Finally, with the gas valve setting at 60 and gas pulse length of 0.3 seconds, the cup was again scanned across the beam diameter to obtain the results shown in Figure 13. Although the apertures have reduced the beam current entering the target chamber, these results clearly show that neutral fraction under these conditions is now on the order of 90% and that the beam collimation is somewhat improved.

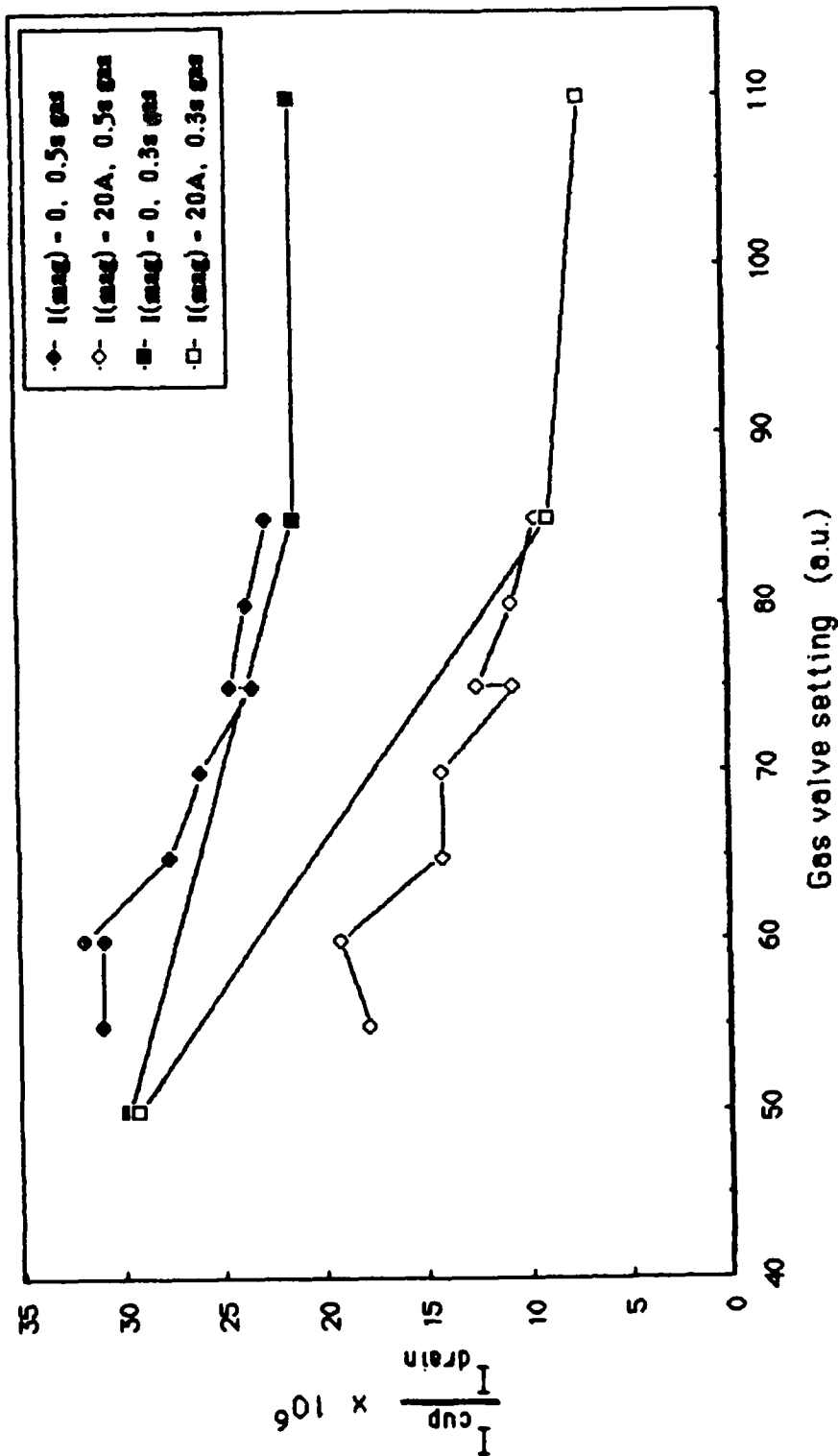


Figure 12 - Normalized detector current vs. gas valve setting.

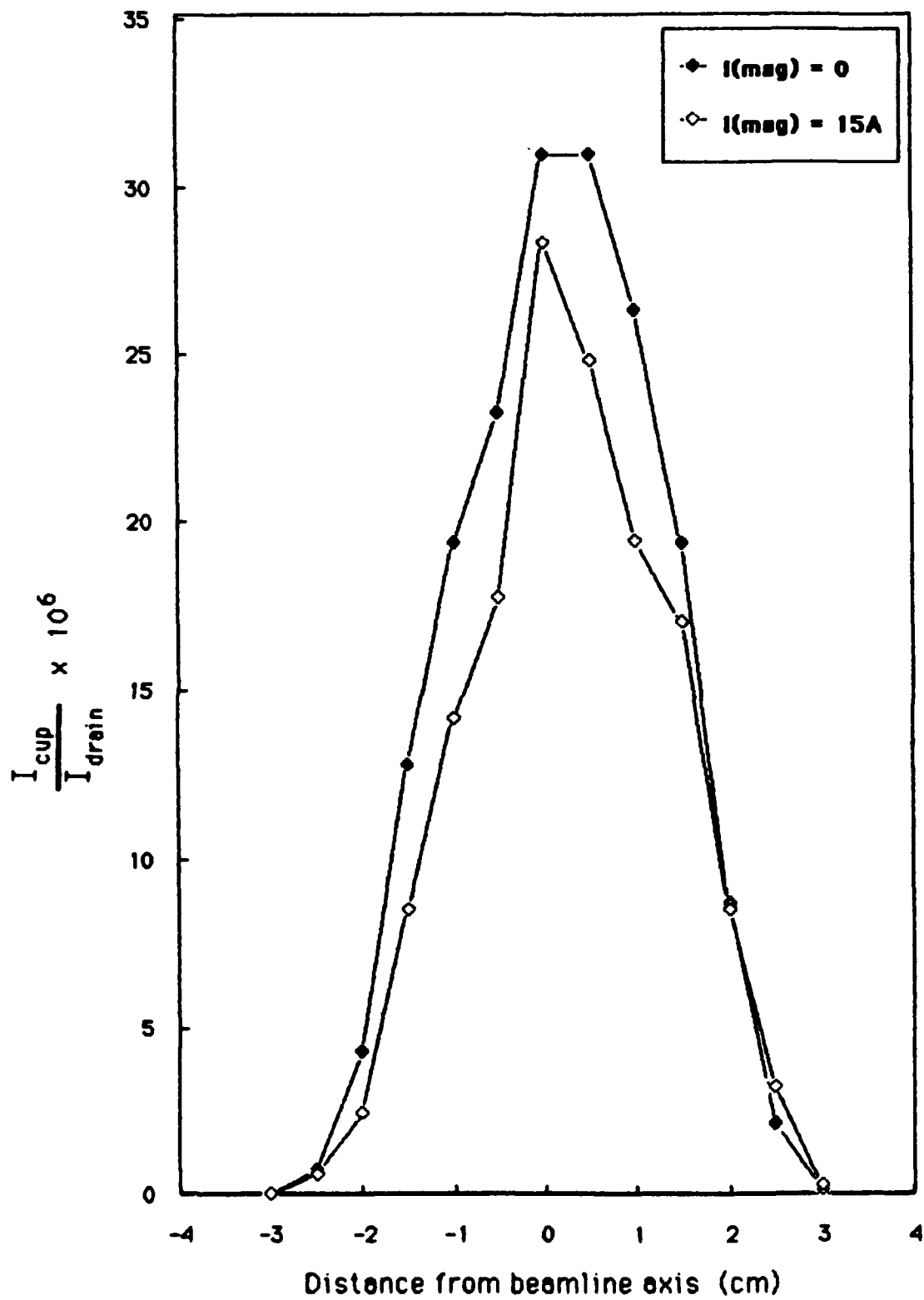


Figure 13 - Beam profile using three 3 cm apertures.

I Ib.5) Ablation Plasma Production and Diagnostics

The production of an ablation plasma involved focussing the ruby laser output onto the surface of a solid target: A plume of ionized target material expands from the surface at a velocity on the order of 10^6 cm/sec. The total number of particles emitted and their energy depends on the energy delivered by the laser. Initial use of the ruby laser involved its operation in the relaxation mode, which can deliver up to about 1.2 Joules. However, in order to facilitate the correlation of laser output with diagnostic signals, the laser has been operated during this period in the Q-switched mode, which delivers up to about 0.3 Joule with a pulse width of 40-60 ns. Oscillograph traces from PIN diode detection of the laser output in both modes are presented in Figure 14.

Prior to this reporting period, carbon plasmas were produced using the relaxation mode output and attempts were made to characterize them. These initial studies involved the use of flat copper plates, biased at various voltage, to collect the charged plasma particles. With the plates located 1.55 and 2.55 cm from the face of the graphite target, it was determined that the electron temperature is in the range $16 < kT(\text{eV}) < 24$, that the maximum ion velocity is about 2×10^6 cm/s, which, for carbon ions, yields an average expansion energy of 6.2 eV.

More recently, Q-switched laser produced carbon plasma has been studied through the use of a Langmuir probe in order to obtain an estimate of the plasma electron temperature. With the laser beam axis perpendicular to the graphite target, the

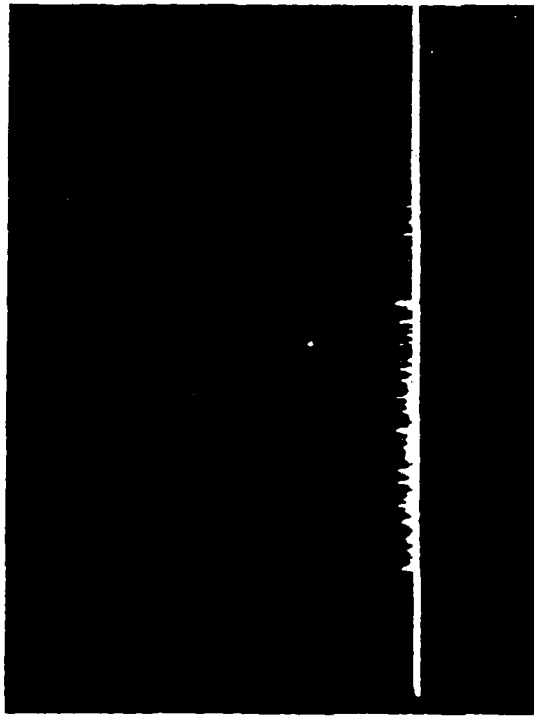


Figure 14 - Laser output as detected by a PIN diode. (A): Relaxation mode output, 0.1V, 0.2ms/div. A calorimeter measured the total output energy in this shot to be 1.7 Joules. (B): Q-switched output, 1V, 1us/div, output energy = 0.8 J.

probe was placed 20 degrees off axis and 4.3 cm from the focal spot. The results of these experiments are presented in Figure 15 and calculations yield electron temperatures of 8.7, 11.1, and 10.7 eV at 2, 5, and 10 us, respectively.

We have also looked at the ablation plasma emission spectra by replacing the Pyrex vacuum chamber with a large glass window on the target chamber and flange and focusing the light onto the entrance slit of an optical multichannel analyzer (OMCA). Spectra obtained from three separate shots are presented in Figure 16. Although we were unable to calibrate for intensities to obtain line ratios and obtain plasma temperature, these spectra show that we are producing carbon ions within a charge state of at least +2.

I Ib.6) Beam/Plasma Interaction Experiments

We have measured changes occurring when energetic hydrogen particles interact with a carbon ablation plasma. Timing is such that the laser is Q-switched after the particle beam is well established. Our initial experiments exhibited a low signal to noise ratio. Further investigations identified more than one source for the interference received by the detector signal. First, it was found that the high frequency signal occurring when the laser is Q-switched was due to the detector circuit acting as an antenna, receiving the noise generated by the pockels cell circuit. Second, it was found that the EMI (electromagnetic interference) problem was aggravated by ground loops in the system. Third, it was found that the

Collection Current
vs Probe Voltage

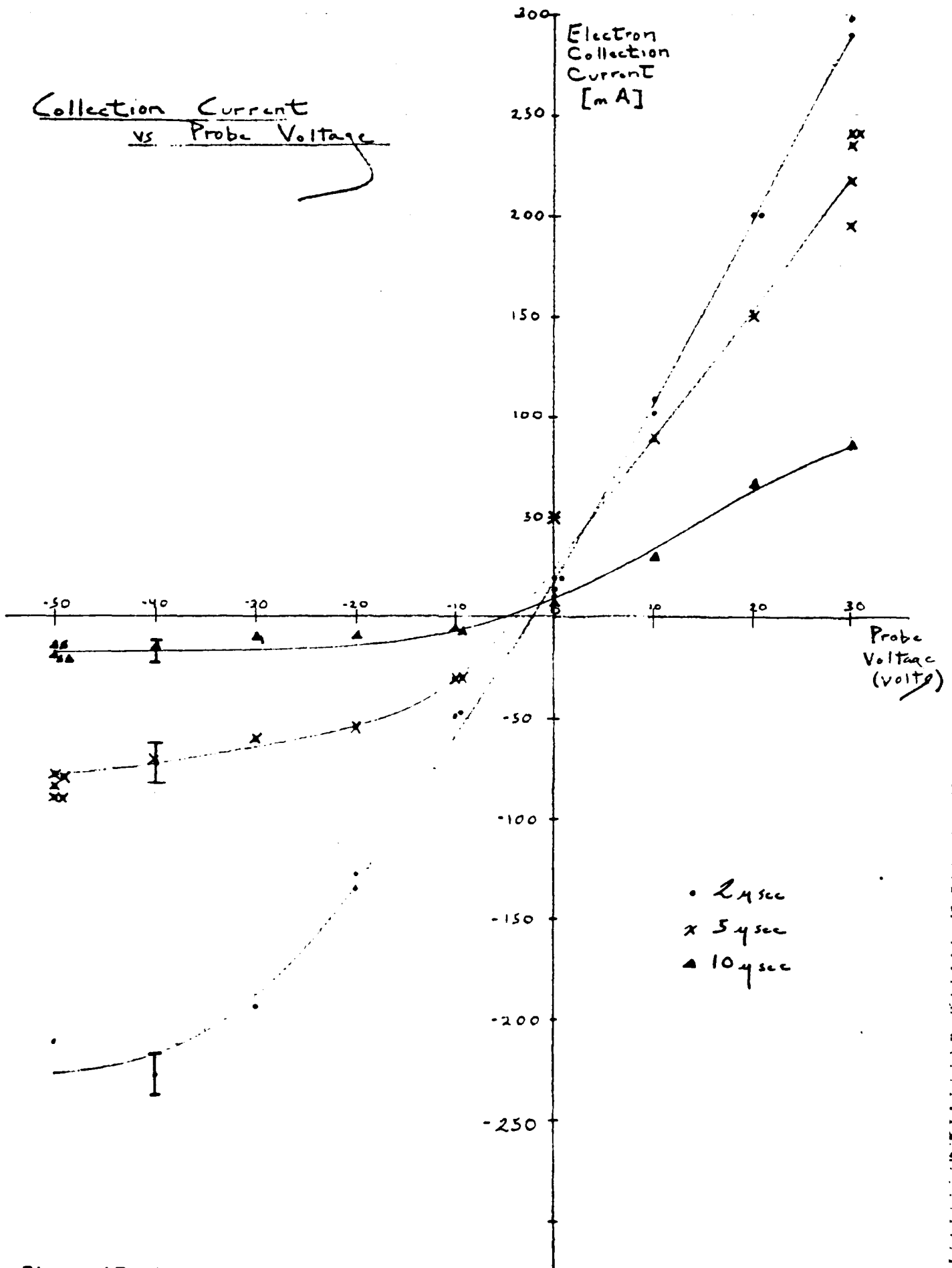


Figure 15 - Langmuir probe results.

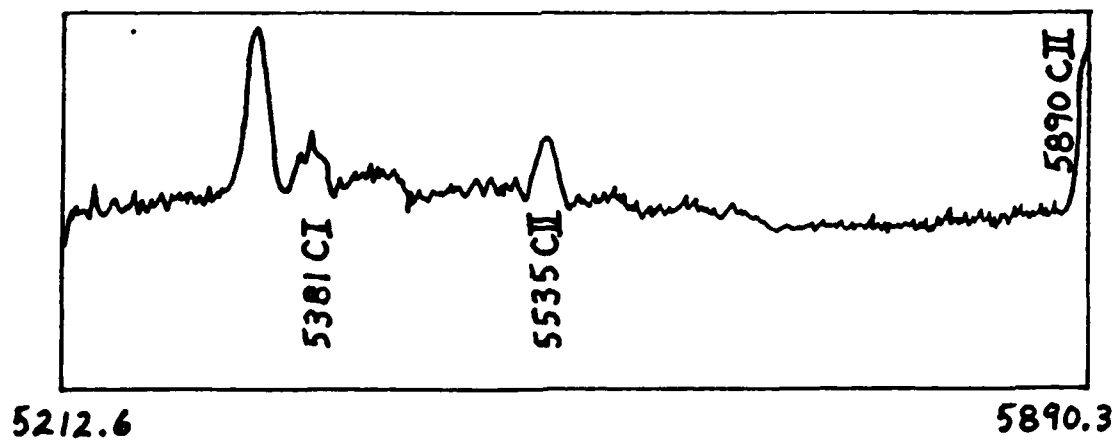
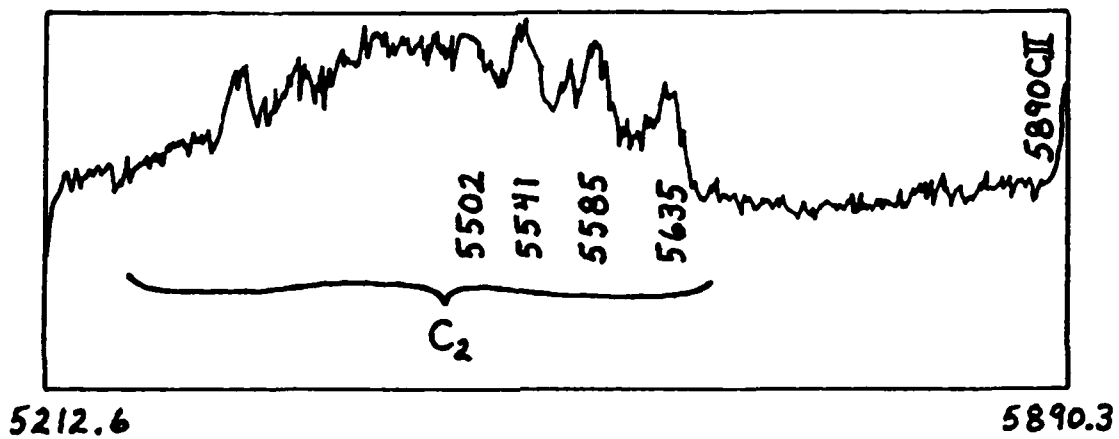
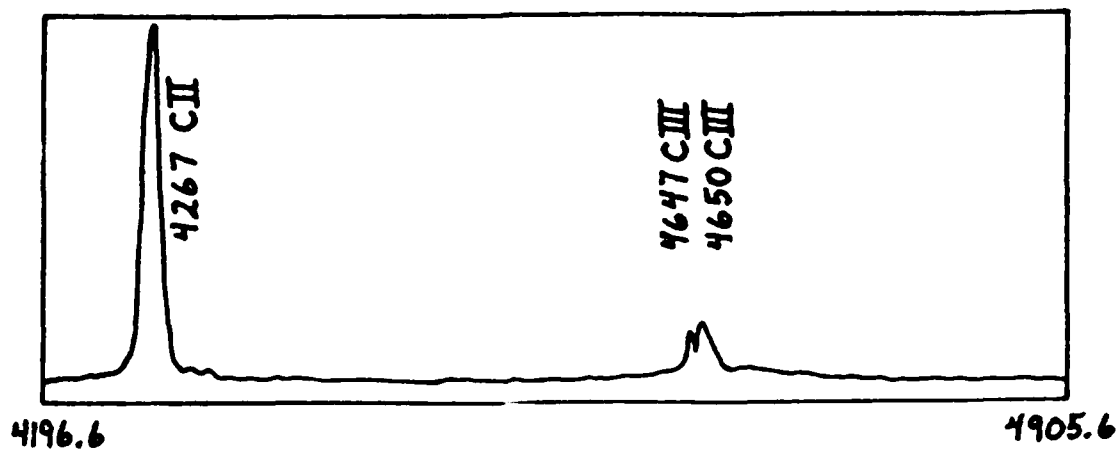


Figure 16 - Ablation plasma emission spectra. Reference 3 used for peak identification.

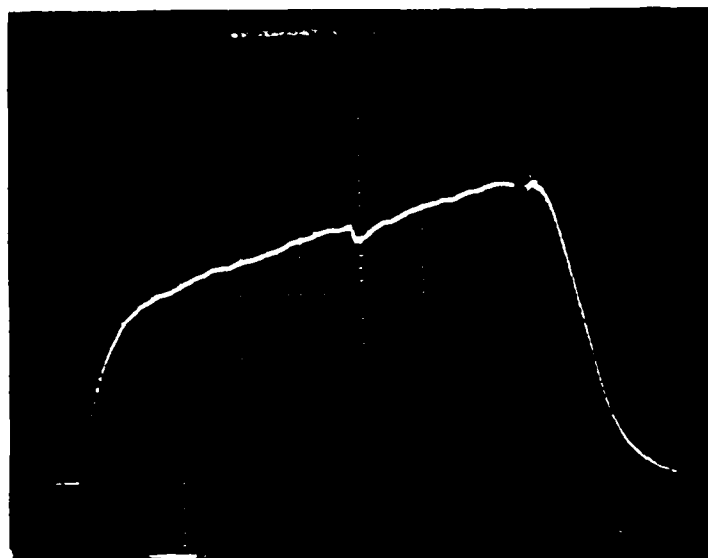
detector was too close to the plasma, that there was significant streaming of plasma into the detector.

Adding a second Pyrex piece to place the detector further from the target chamber helped to reduce the third source but not to eliminate it, and so small apertures were placed between the target chamber and the Pyrex system, requiring the addition of the third pumping system. Next, ground loops were eliminated and attempts were made to shield from the EMI by placing copper sheet and RF shielding tape around the pockels cell, which significantly reduced the magnitude and duration of the noise picked up by the detector circuit.

With the noise levels reduced to the point where we could make meaningful measurements of the small change in detector current following the firing of the laser, the full beam/plasma interaction experiment was conducted using 10 keV hydrogen beams and Q-switched laser pulses. Typical attenuation data for the case of no bending magnet current (neutral + ion beam) and for 18 amps of bending magnet current (neutrals only) are presented in Figure 17. It is seen that as much as 12% of the beam current is lost due to beam interactions with the plasma.

Data from a "neutrals only" shot is presented in Figure 18 along with a best fit of the self-similar expansion model. The model yields a value of the maximum line density which, for a maximum attenuation of approximately 13%, agrees quite well with the simple predictions given in Figure 2.

NEUTRAL (87%) + ION (13%) BEAM



10 mV, 50 μ s / div

$$\frac{I}{I_{\min}} = 0.94$$

SHOT #1166 :

$$V_{\text{accel}} = 9.8 \text{ kV}, \quad I_{\text{mag}} = 0$$

$$I_{\text{arc}} = 22 \text{ A}, \quad I_{\text{drain}} = 0.52 \text{ A}$$

$$I_{\text{detec}} = 4.0 \mu\text{A} \quad \text{at } t=225 \mu\text{s}$$

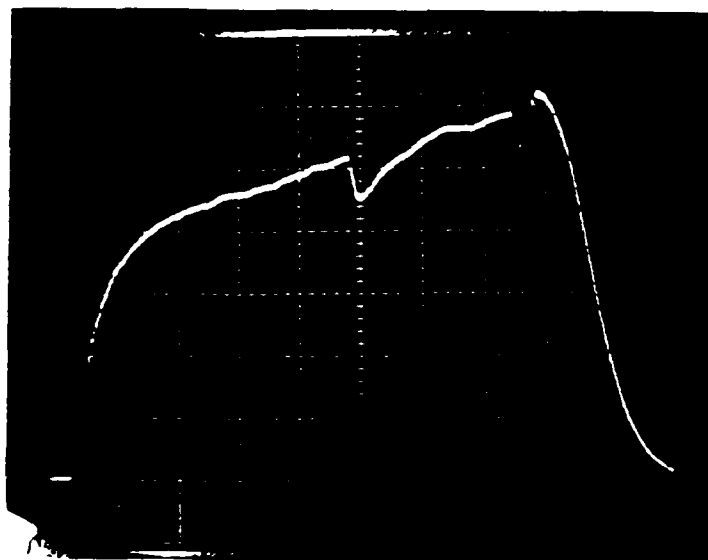
Beam ion fraction ~ 0.13

Laser: $\sim 0.1 \text{ J}$ on target

$\sim 40 \text{ ns FWHM}$

($\sim 1 \times 10^{12} \text{ W/cm}^2$ peak)

NEUTRAL BEAM (>99%)



5 mV, 50 μ s/div

$$\frac{I}{I_{\min}} = 0.88$$

SHOT #1171 :

$$V_{\text{accel}} = 10.0 \text{ kV}, \quad I_{\text{mag}} = 18 \text{ A}$$

$$I_{\text{arc}} = 20 \text{ A}, \quad I_{\text{drain}} = 0.39 \text{ A}$$

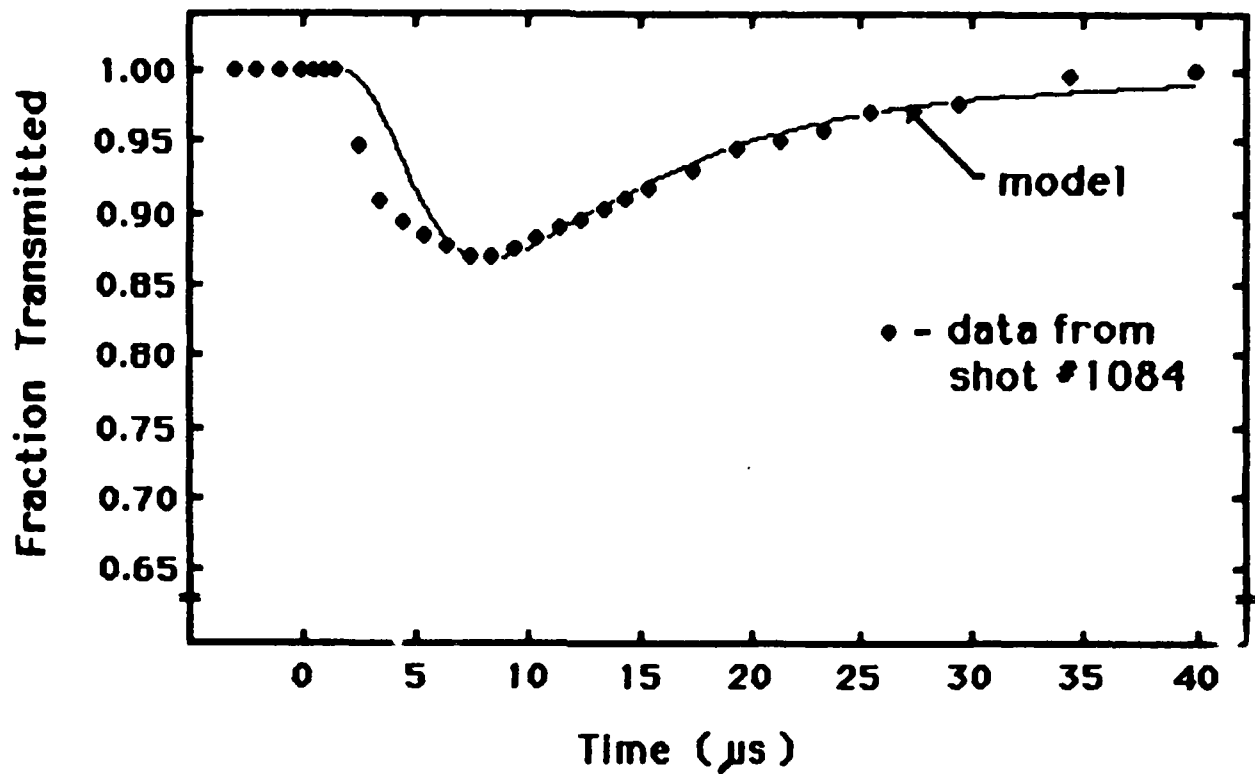
$$I_{\text{detec}} = 2.6 \mu\text{A} \quad \text{at } t=225 \mu\text{s}$$

Laser: $\sim 0.3 \text{ J}$ on target

$\sim 40 \text{ ns FWHM}$

($\sim 3 \times 10^{12} \text{ W/cm}^2$ peak)

Figure 17 - Typical attenuation data.



Shot #1084 : $V_{\text{accel}} = 10 \text{ kV}$, $I_{\text{mag}} = 18 \text{ A}$

Model : Self-similar expansion normalized to the data at the point of maximum attenuation, which yields

$$\bar{n}_{\text{max}} = 2.8 \times 10^{13} \text{ cm}^{-2}$$

Best fit obtained with $k = 4$, $v_z^0 = 3 \times 10^6 \text{ cm/s}$

Figure 18 - Neutral beam attenuation, experiment vs. model.

Current work includes providing the means by which we can discriminate between beam ions and neutrals in order to correlate shots such as are shown in Figure 17. We are also investigating the discrepancy between data and model in the first 5 us after firing the laser, seen in Figure 18. The ion fraction with the magnetic field on is less than 1%. For the case of no bending magnet the ion/neutral fraction is estimated to be 13%:87%.

IIC) Fabrication of an Applied - B Ion Diode for the Febetron

In order to achieve higher energy and higher current ion beams for our interaction experiments we have fabricated an applied B (radial) magnetically insulated ion diode which is compatible with our existing Febetron Pulser. The higher energy beam will permit us to obtain higher energy scaling data compared to the 20 kV duopigatron data, whereas the higher beam current should improve the signal to noise ratio of our particle detectors. The Febetron parameters are:

Voltage Maximum = 500 kV

Current Maximum = 1.4 kV

Pulselength = 400 nsec. full width on current

A schematic illustration of the applied - B diode as configured for the Febetron is depicted in Figure 19. (This design is similar to those described in references 4 through 9.) The Febetron will initially be run in positive polarity with a flashboard anode and a carbon brush cathode. Figures 20 and 21 give more detailed views of the recently constructed ion diode magnet coils and vane structure. The

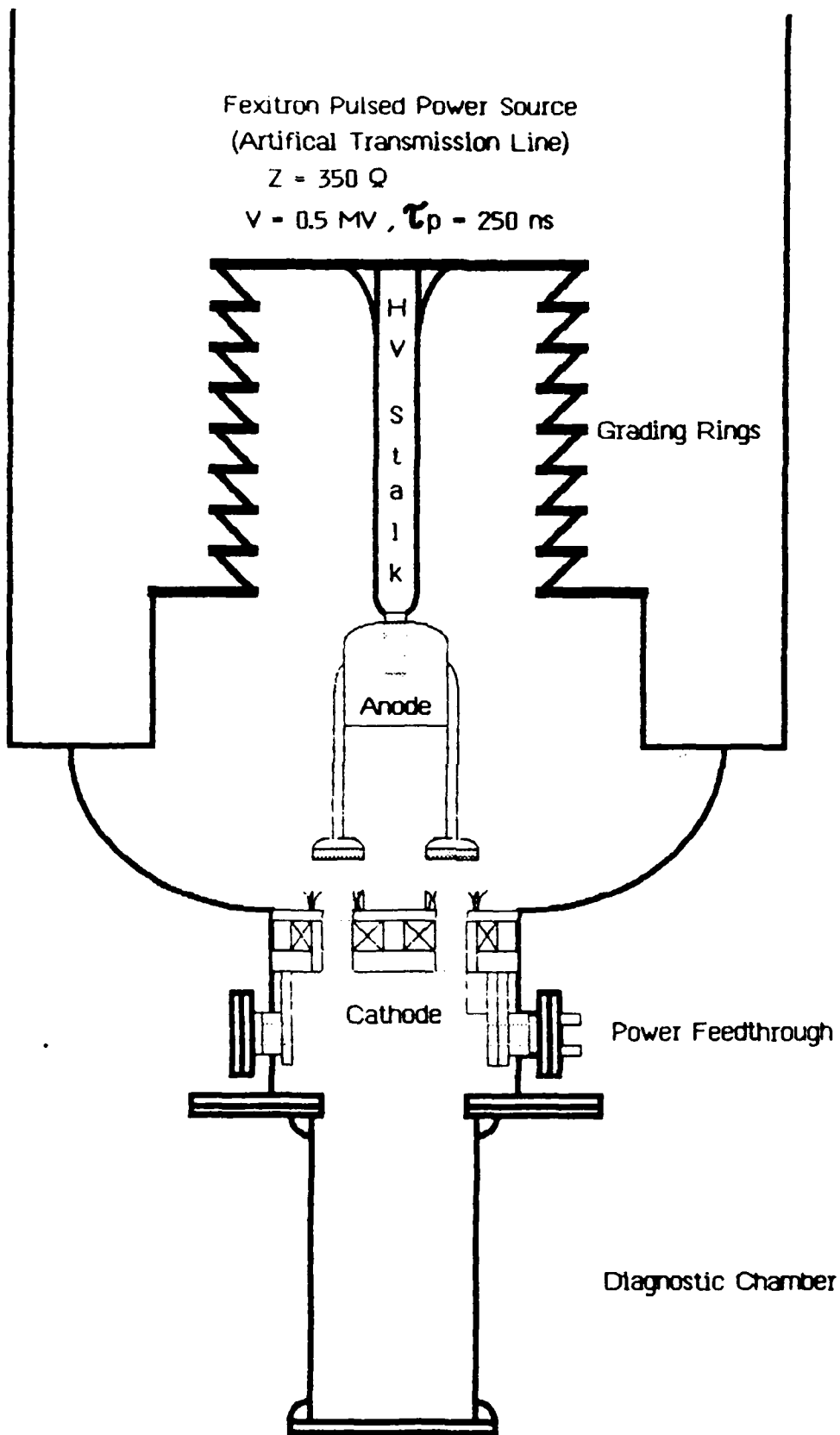


Figure 19 - Diode Experimental Assembly

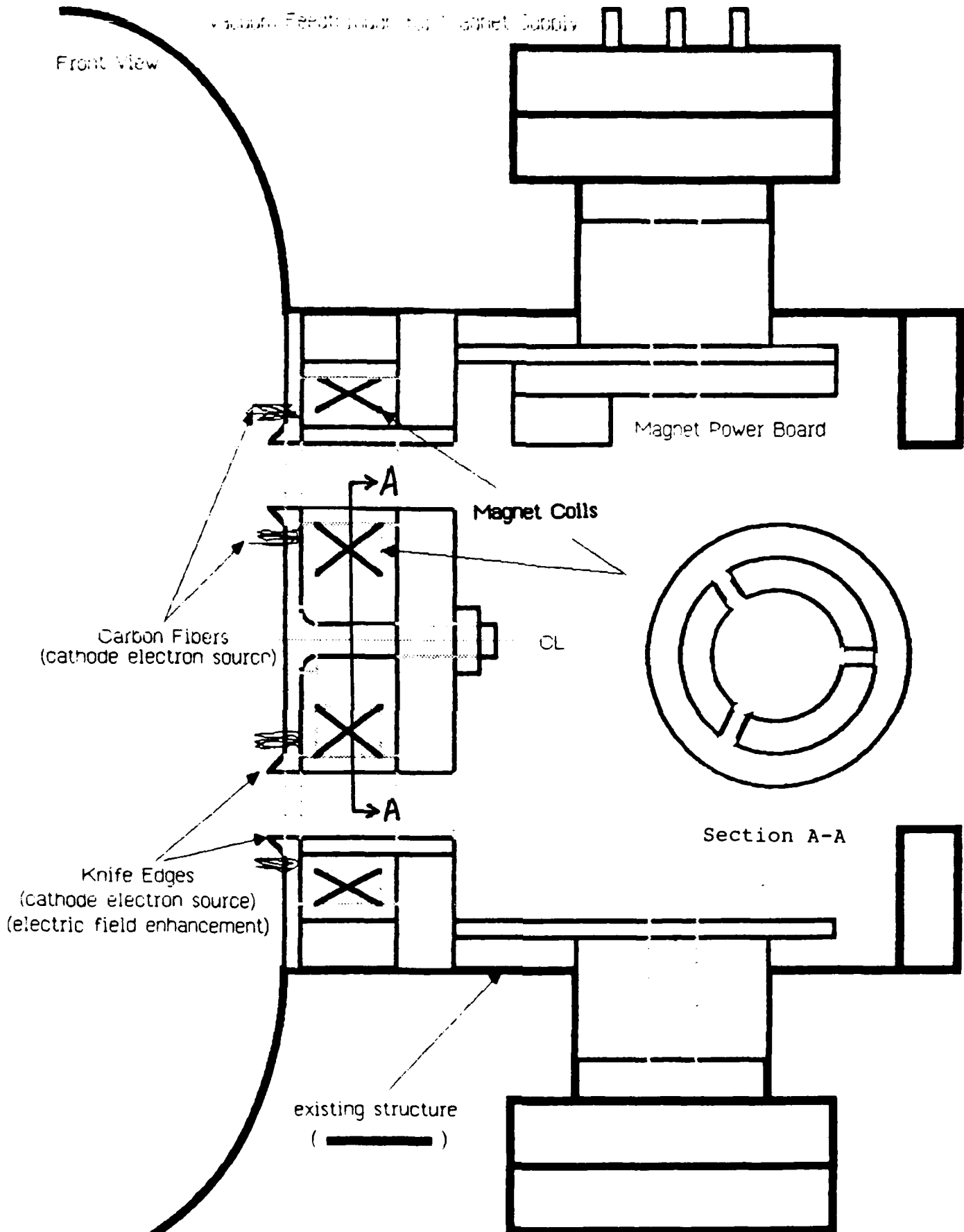


Figure 20 - CATHODE
(cross-sectional view)



Figure 21

flashboard anode (Fig. 22) employs a lucite plate with imbedded copper pins.

An important consideration in the design of this diode was the necessity of achieving a radial magnetic field which exceeds the critical insulating field. The critical insulating field for a 1-D planar diode can be calculated from the expressions given in references 10-13. Assuming that we wish to operate at 1.5 times the critical field the following table gives the required performance of our ion diode:

V(kV)	B _{crit} (Gauss)	1.5 B _{crit} (Gauss)
50	772	1158
100	1118	1677
200	1650	2475
300	2101	3152
400	2516	3775
500	2911	4366

The magnitude of these fields dictated that the magnet coils needed to be operated in the pulsed mode. The capacitive discharge magnet power supply depicted in Figure 23 was constructed for this purpose. Details of the ignitron firing circuit are given in Figure 24. Typical data for the magnet current trace and integrated B dot loop signals are given in Figure 25. The measured radial magnetic field (Figs. 26 and 27) easily exceeds the critical insulating field for the magnet and power supply which we have constructed.

AD-A162 330

NEUTRAL BEAM INTERACTIONS WITH MATERIALS(U) MICHIGAN
UNIV ANN ARBOR DEPT OF NUCLEAR ENGINEERING
R M GILGENBACH ET AL 22 NOV 85 AFOSR-84-0130

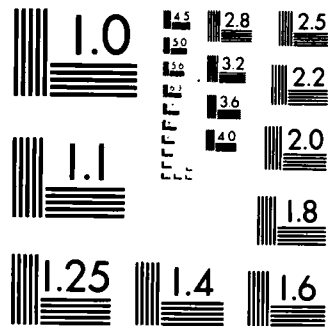
2/2

UNCLASSIFIED

F/G 20/9

NL





MICROCOPY RESOLUTION TEST CHART
NATIONAL BUREAU OF STANDARDS-1963-A

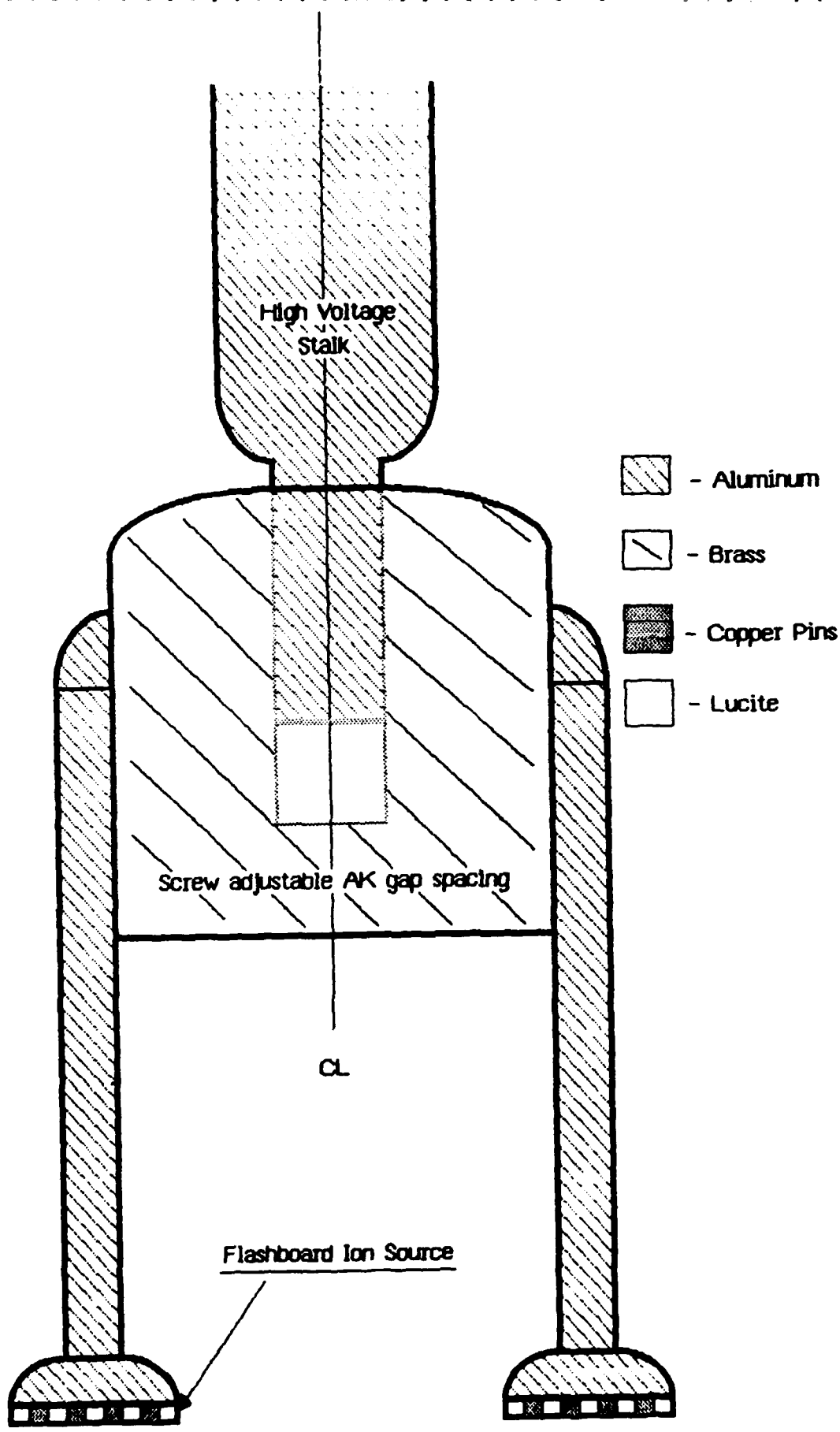


Figure 22 - ANODE
(cross-sectional view)

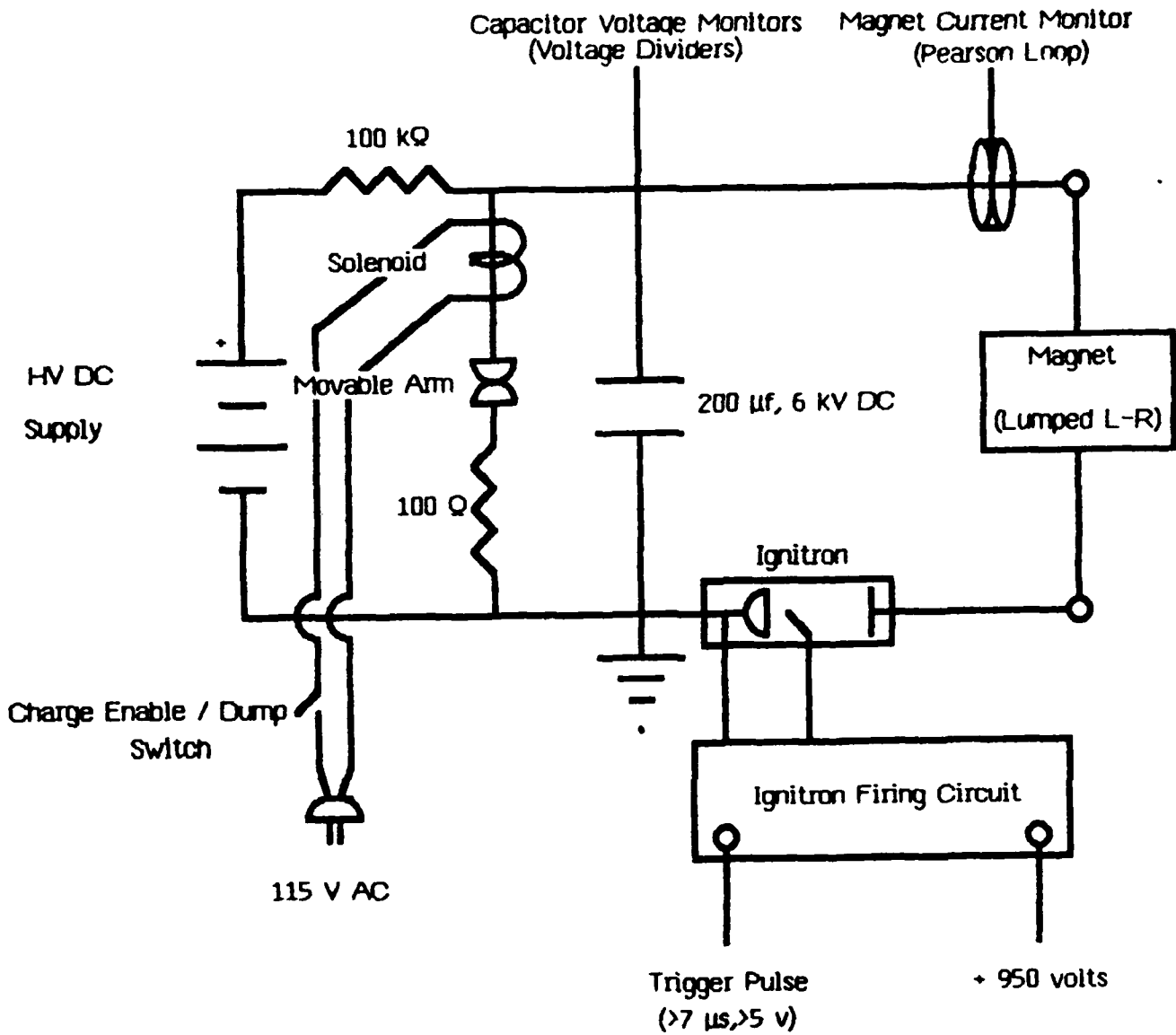


Figure 23 - Pulsed Magnet Supply

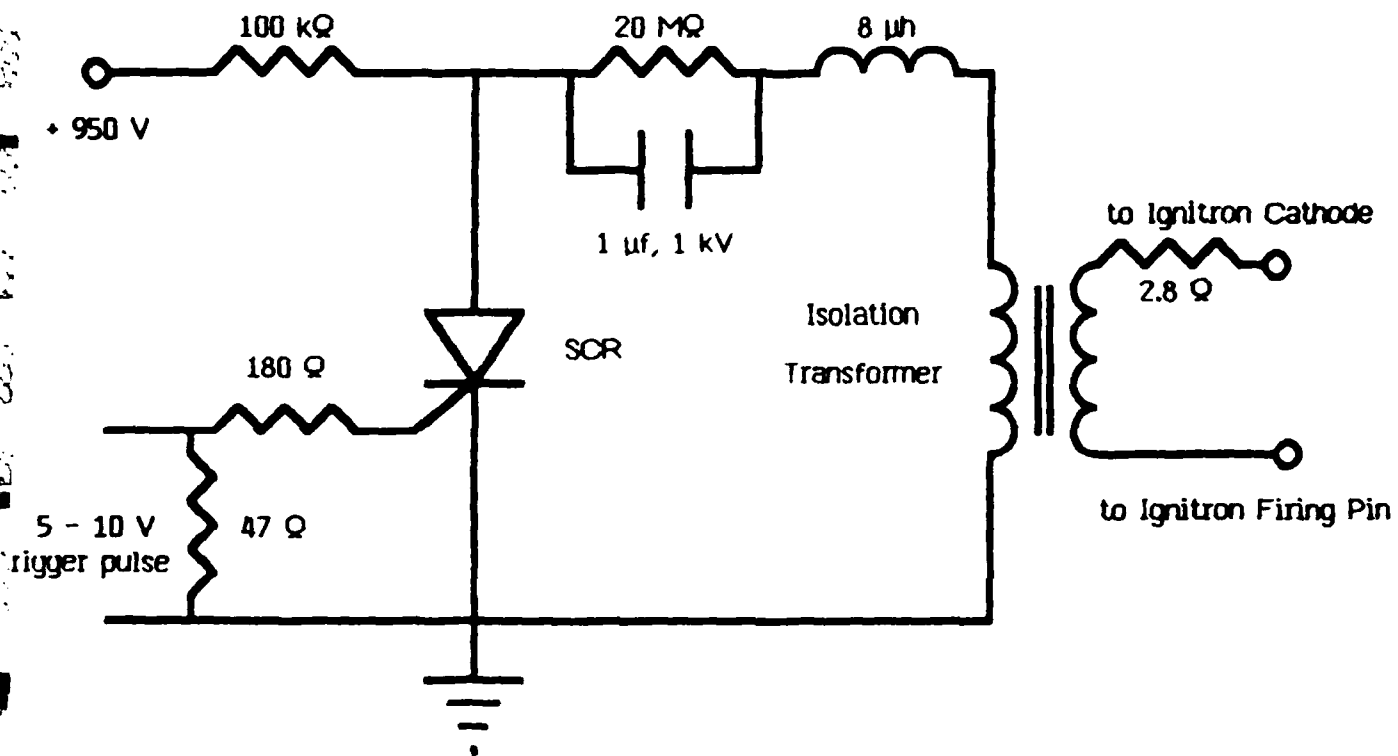


Figure 24 - Ignitron Firing Circuit

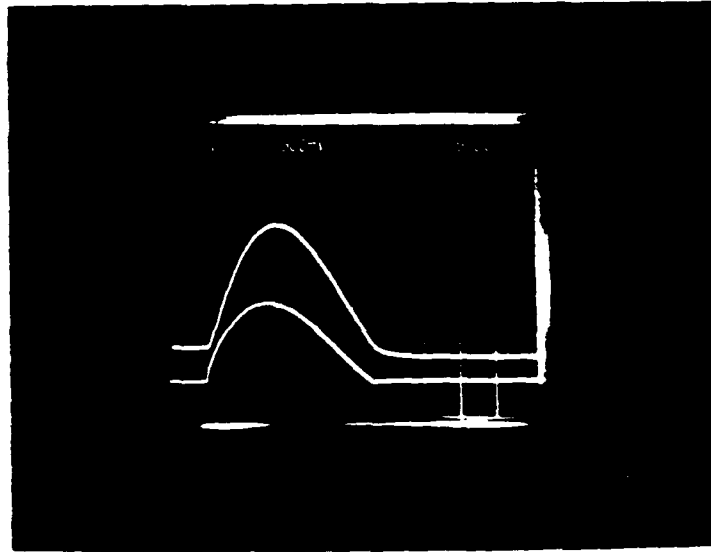


Fig.25- Top trace: example of self-integrated B dot probe (r = center of gap, z = 3.5 cm) 100 turns, $A = 4.95 \times 10^{-5} \text{ m}^2$, RC = 22 ms, V = 2 KV
Note that the trace for B(t) follows the current very well signifying good integration of the signal.

Bottom trace: Magnet current measured through Pearson coil 0.05 v/amp x 30.0 atten

AXIAL MAGNETIC FIELD VARIATION

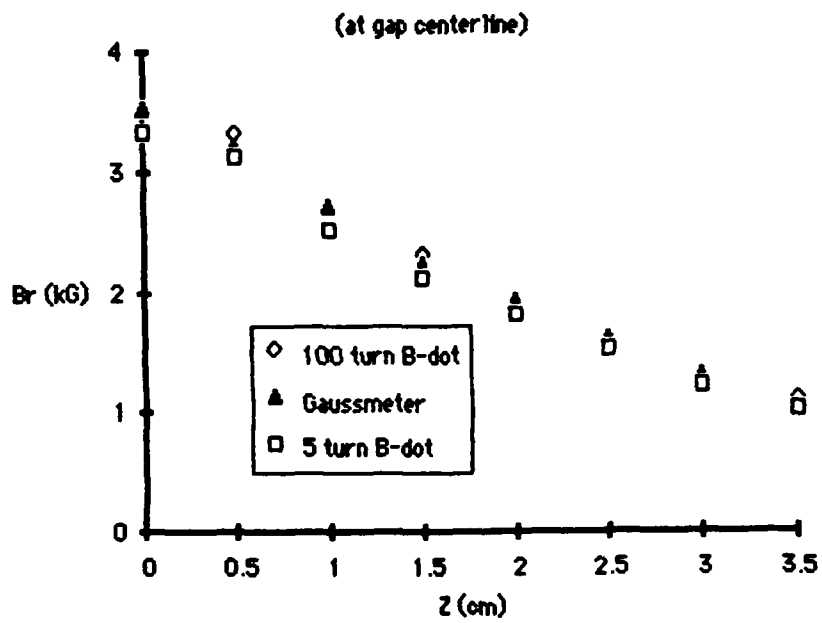


Figure 26

MAGNETIC FIELD

at gap centerline and $z = 0$

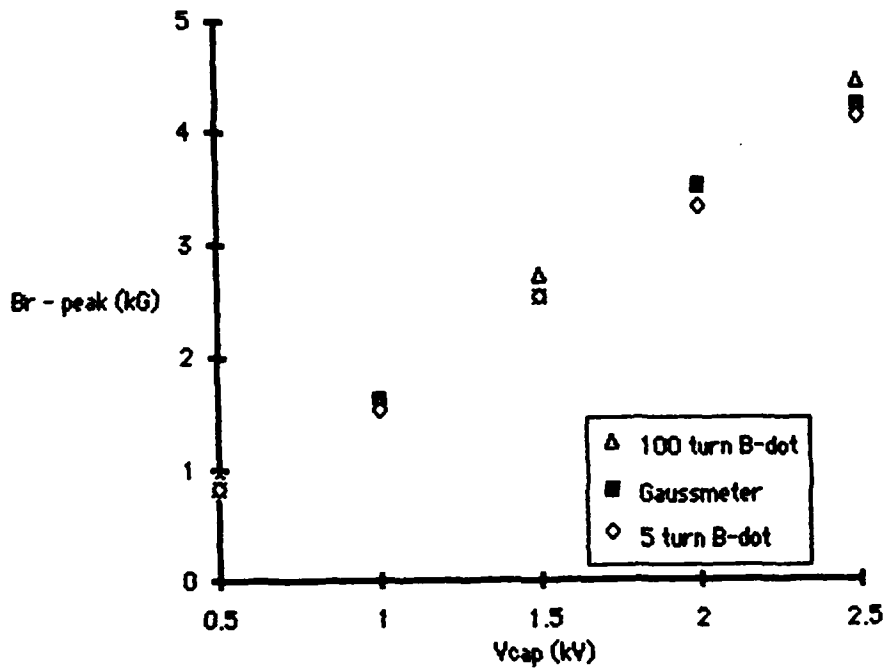


Figure 27

REFERENCES FOR SECTION II

1. R. A. Hulse, D. E. Post and D. R. Mikkelsen, J. Phys. B 13 (1980) 3895.
2. G. J. Tallents, Laser and Particle Beams (1983), Vol. 1, Part 1, pp. 171-180.
3. Selected Tables of Atomic Spectra, NSRDS-NBS 3, Section 3, Nov. 1970.
4. S. Humphries Jr., J. Appl. Phys., 49 (1978) 501.
5. S. Humphries Jr., et al., J. Appl. Phys., 51 (1980) 1876.
6. Y. Nakagawa, Jpn. J. Appl. Phys., 22 (1983) L326.
7. K. Horioka, et al., Jpn. Jor. Appl. Phys., 23 (1984) L374.
8. J. Mizui, et al., BEAMS83, p. 151.
9. Y. Nakagawa, BEAMS83, p. 163.
10. T. J. Orzechowski and G. Bekefi, Phys. Fluids., 19 (1976).
11. R. N. Sudan and R. V. Lovelace, Phys. Rev. Lett., 31 (1973).
12. R. V. Lovelace and Edward Ott, Phys. Fluids, 17 (1974).
13. T. M. Antonsen Jr. and E. Ott, Phys. Fluids, 19 (1976).

III. Graduate Students Supported in Part by this Contract

1. J. W. Thornhill, Ph.D. (Dissertation Defended, Dec.'84)
2. J. Meachum, Ph.D. Candidate (Dissertation in Progress)
3. M. Cuneo, Ph.D. Candidate
4. R. Kensek, Ph.D. Candidate (Dissertation in Progress)
5. E. Pitcher, M.S. Candidate
6. L. Smutek, M.S. Candidate
7. S. Bidwell, M.S. Candidate
8. K. Pierce, M. S. Candidate

IV. Publications and Dissertations since June 1, 1984 Funded by this Contract

P. D. Weber and R. M. Gilgenbach, "Intermediate and High Mass Ion Beams from a 10-cm Duopigatron," Plasma Chemistry and Plasma Processing, Vol. 4, June 1984.

J. W. Thornhill, Doctoral Dissertation: "The Hydrodynamics and Ionization Dynamics of Particle Beam Heated Carbon Ablation Plasmas."

"Neutral and Ion Beam Interactions with Laser Ablation Plasmas," J. Meachum, R. M. Gilgenbach, M. Cuneo, and E. Pitcher, Presented at the 1985 IEEE International Conference on Plasma Science, June 3-5, 1985, Pittsburgh, PA.

"Plasma Generation from Microsecond Intense Electron Beams," M. Cuneo, R. M. Gilgenbach, M. L. Brake, R. F. Lucey, L. Horton, S. Bidwell, J. Miller, K. Pierce, T. Repetti, L. Smutek. Presented at the 1985 meeting of the APS Division of Plasma Physics, Nov. 4-8, 1985, San Diego, CA.

V. Honors and Awards

R. M. Gilgenbach received the Outstanding Young Engineer Award from the IEEE Nuclear and Plasma Sciences Society. He was presented a "Centennial Key to the Future" at the award ceremony in San Jose, CA on November 30, 1984.

END

FILMED

1-86

DTIC